

Time-Resolved X-ray Measurements of Energy Relaxation in Ultrafast Laser Excited Semiconductors

by

Soo Heyong Lee

A dissertation submitted in partial fulfillment
of the requirements for the degree of
Doctor of Philosophy
(Physics)
in The University of Michigan
2006

Doctoral Committee:

Professor Reis, David A., Chair

Professor Bucksbaum, Philip

Professor Clarke, Roy

Professor Sension, Roseanne J., Cognate

© Soo Heyong Lee 2006
All Rights Reserved

For My Family and Friends

ACKNOWLEDGEMENTS

I just finished up writing my thesis, and about couple hours away from submitting it to Rackham. That would conclude one of the most important chapters in my life. However writing this little section of acknowledgement seems much more difficult than I had expected. There are so many people who helped me out in many ways during my graduate school years. Listing them all in a piece of paper would be quite difficult. But that is not going to stop me from trying.

I thank my family for their relentless support. I would like to thank my mother and father for bringing me to this world and always being there for me. If anyone knows anything about my life, they would know that it has been a very bumpy ride so far. There are times when I was so lost that I almost gave up. But my parents would not let that happen and always have been there for me. My fiancé and my sister have there for me too. I always wanted to thank them and let them know much I love them. But I am such a stubborn guy; it is very difficult to speak my mind. I hope that they already know about it. Of course, I cannot leave out Zzonzzon (my parents' pet dog) for biting my hand at the airport on December 23rd 2005.

I greatly thank my advisor David A. Reis. David has been my mentor for last four years, and it has been a privilege working in his group. Whether he believes it or not, I tried my best to be a good student. I think that he is one of the smartest person I have ever met, and I hope to be like him someday. I thank professor Philip Bucksbaum, professor Roy Clark, and professor Roseanne Sension for being in my defense committee. Without their help, I would be nowhere right now. I also would like to thank professor Roberto Merlin for helpful discussion sessions and Rachel Goldman for growing AlGaAs/GaAs sample for us.

David Fritz and Adrian Cavalieri have been my colleagues in David's group. Fritz has been one of my best friends in graduate school and also a good role model. I always try to copy what he does, starting from aligning lasers, appreciating NBA games to eating and excising properly. Adrian has been like an older brother that I never had. At times he yells at me, but he often looks out for me whenever I am in a tight spot. I will miss countless nights that we sat in front of computer screens waiting for some amazing data to roll in. I hope that they know how much I appreciate their help.

Jason Devita has been my best non-X ray or laser related friend in graduate

school. I enjoyed having computer related conversations with him over lunch at Seva. He taught me how to ride a long board. He also saved my life by carrying me to ER when I fell off my board a couple years ago. Furthermore without his help, I would not be graduating because he needs to submit my thesis to Rackham in a few hours. I hope that I can still count on him. Mariano (Manu) Trigo also was a good friend of mine along with my very first post doc Jarred Wahlstrand. Of course, I thank Yumiin for bringing good cookies to my defense.

I thank scientists at sector 7 at APS for taking care of me like I am one of their own. Eric Landahl has been like my personal post-doc and a friend throughout my life at APS. Without his advice and help, I would not be graduating this term. And I would like to thank his wife Sarah for having me for dinner and showing me around downtown Chicago. Don Walko showed me many X-ray diffraction techniques and made sure that I had enough sleep. I thank you Dohn Arms for being my friend and helping out with data acquisition setup. Eric Dufresne also helped me a lot by borrowing me some of his beam time, so that I can take more data. I personally thank Harrold for numerous advices and showing me how to properly solder really thin wires. Finally I thank Jin Wang for having me around at sector 7, so that I could do my experiments. Of course, I cannot forget Steve Ross and detector pool staffs for their support. I will never take my eye off Mar345.

Finally I also like to show my gratitude to my loyal SPS friends: Geoff Svacha, Matt Pennington, John Blum, James Degandhardt, Ryan Foley, and Brandon Preblich. They have been my friends forever, and I hope that we can hang out again pretty soon.

I know that I left out some people whom I owe my appreciation to. But I really need to submit my thesis pretty soon. So I will need to thank you in person.

Finally, I have always thought that I can measure someone's success by looking at how successful their friends are. If I still believe that, I have been a very succesful person, and I hope to keep it that way.

TABLE OF CONTENTS

DEDICATION	ii
ACKNOWLEDGEMENTS	iii
LIST OF FIGURES	viii
LIST OF APPENDICES	xvi
CHAPTER	
I. Introduction	1
1.1 Underlying Physics of Semiconductors// Upon Ultrafast Laser Excitation	1
1.2 Relevant Experiments	4
1.2.1 Optical Pump Probe Methods	4
1.2.2 Time-Resolved X-Ray Scattering Experiments	6
1.3 Thesis Motivation and Organization	9
II. Experimental Setup	12
2.1 Laser Pumped and X-ray Probed Experiment	12
2.2 Overview of the Experimental Site	14
2.3 Synchrotron X-Ray Source	15
2.3.1 Background	15
2.3.2 Electron Accelerator and Storage Ring	16
2.3.3 Temporal Properties of Electron Bunch Structures	17
2.3.4 Synchrotron Radiation	19
2.4 Monochromator	21
2.5 Laser System	22
2.5.1 Ti:Sapphire Oscillator	23
2.5.2 Amplified Laser System	25
2.6 Laser to X-ray synchronization	28
2.7 Detectors	30
2.7.1 Ion Chamber	31
2.7.2 Avalanche Photo-Diode (APD)	32

2.8	Expected Improvements	35
III.	Theory	36
3.1	Simulation of Strain Generation and Propagation	37
3.1.1	Stress and Strain Relation in Solids	37
3.1.2	Simulation of Laser Induced Strain Generation and Propagation	40
3.1.3	Effect of Plasma Diffusion and Recombination	43
3.1.4	Dynamical Matrix and Dispersion Relation	45
3.2	Theory of X-ray Diffraction	48
3.2.1	Formulation of X-ray Diffraction	48
3.2.2	Theory of Dynamical X-ray Diffraction	52
3.3	Probing Phonons Dispersion Relation with X-Rays	57
IV.	Time Resolved X-Ray Diffraction	60
4.1	Generation and Propagation of Acoustic Pulse at a Buried Interface	60
4.1.1	Probing with X-rays	60
4.1.2	Experimental Apparatus and Procedure	63
4.1.3	Observation of Unipolar Strain Pulse	65
4.1.4	Comparison with Simulation	69
4.2	Measurements of Thermal Expansion versus Deformation Po- tential	72
4.2.1	Experimental Layout	72
4.2.2	Origin of Impulsive Strain Generation in GaAs	76
4.3	Laser Fluence Dependent Excitation Dynamics	79
4.3.1	Effect of Free Carrier Absorption	80
4.3.2	Observation of Free Carrier Absorption	81
4.3.3	Incorporation of FCA in the Numerical Simulation	83
4.3.4	Long Thermal Equilibrium Process	87
V.	Time-Resolved Inelastic X-Ray Scattering	92
5.1	Motivation	92
5.2	Experimental Schemes	94
5.2.1	Transmission Geometry	95
5.2.2	Reflection Geometry	96
5.3	Non-Equilibrium Lattice Dynamics in InSb	98
5.3.1	Uniaxial Property of Propagating Strain	98
5.3.2	Perpendicular to Surface Normal: Scan along (1 -1 0)	99
5.4	Observation of Terahertz Acoustic Phonons	102
5.5	Laser Induced Zone Boundary Acoustic Phonons	104

VI. Summary and Outlook	108
6.1 Progresses in Time-Resolved X-Ray Science	110
6.2 New Sciences	116
APPENDICES	118
BIBLIOGRAPHY	135

LIST OF FIGURES

Figure

1.1	Typical set up for the time-resolved all optical detection of coherent phonons oscillations. We send an additional laser pulse following a pump-pulse with variable time-delays. By measuring amount of reflected light at each time delay, we can probe the dynamics over the entire cycle of the system. The time-resolution in this scheme is typically in orders of tens to hundreds of femtoseconds	3
1.2	Isotropic reflectivity changes measured with optical pump-probe methods. Data displays different oscillatory behaviors depending on doping level in the sample [1]. Despite sub-picosecond time-resolution, one cannot directly deduce how much the lattice moved.	5
1.3	Transient changes in X-ray diffraction efficiency upon ultrafast laser excitation at two different reflections (111) and (222) in Mismuth crystal is measured with plasma based source [2]	7
1.4	Time-resolved X-ray diffraction efficiency measured at different angles about InSb Bragg peak. Despite 100 ps time-resolution at ALS, sub 10 ps dynamics were measured using X-ray streak camera [3].	9
1.5	Time-resolved rocking curves of impulsively strained InSb crystal. (a), and (d) are collected sets of data and (b) and (e) are result obtained from numerical modeling to simulate the temporal evolution of strain inside the crystal [4].	10
2.1	The Advanced Photon Source(APS) at the Argonne National Laboratory provides this most brilliant X-rays for research in various scientific disciplines such as biology, chemistry, physics and ect. . . .	13
2.2	Experimental floor layout at MHATT/XOR sector 7 insertion beam-line.	14
2.3	The brilliance of X-ray sources as a function of time. The brilliance of early lab source and each generation of synchrotrons are compared	16

2.4	General layout of APS electron accelerator and storage ring structures. The schematic also displays the locations of the experimental hutches. Electromagnetic field from the electromagnets around the ring structure focuses the electrons into a narrow beam that is bent on a circular path within vacuum chambers running through the centers of the electromagnets.	17
2.5	Fill pattern under standard operating mode at APS. 24 singlets with a nominal current of ~ 4.25 mA and a spacing of ~ 153 nanoseconds between singlets.	18
2.6	The alternating poles of an undulator create a series of small amplitude oscillations in a moving direction of electrons that emit synchrotron radiation at each pole. A certain fundamental wavelength is selected by the path length travel, which can be controlled by change the undulator gap.	20
2.7	Properties of small oscillations for coherent generation of synchrotron radiation.	21
2.8	A double crystal monochromator. Polychromatic X-ray beam is incident on the first sets of lattice planes but only one wavelength satisfies two successive Bragg conditions.	22
2.9	Design of KML oscillator system used in the experiments	24
2.10	Grating-pair stretcher used to provide positive dispersion. Lenses (L1 and L2) are separated by twice their focal length. A reflector is used to fold the beam path. Difference in distance between the grating and lens and the focal length determines the total dispersion.	25
2.11	Multipass amplifier Design that was used at sector 7 prior to its decommission, which took place during our run in summer of 2003.	27
2.12	Current regenerative amplifier scheme from Positive Light. The unit is capable of delivering 30 fs pulse at average power output of 2.5 W.	27

2.13	Laser to X-Ray Timinig Synchronization Scheme. 44 MHz signal delivered from the storage ring facility is fed into the bunch clock generator (BCG) to reconstruct 351.9 MHz, which is mixed with 4th sub harmonic of the laser oscillator frequency. Error signal is used as a feedback to adjust the cavity length of the oscillator to minimize the error signal, thus locking laser system timing to the reference frequency of 351.9 Mhz.	29
2.14	Overview of laser to synchrotron radiation timing at sector 7	31
2.15	Ion chamber outputs current calibrated to number of X-ray photons. Figure taken from [5]	32
2.16	First figure (on left) shows typical rise time of APDs (5~10ns) that were used in the experiment. In this case APD was running under single photon counting mode. Figure on right was taken from APD under normal linear mode, and it shows X-ray pulse trains under standard fill pattern operation mode. The spacing between each singlet is approximately 150ns	33
2.17	The HUBER diffractometer used in the experiment has four degrees of freedom in movement.	34
2.18	Experimental layouts at D-Hutch. Ti:Sapphire laser oscillator is synchronized to master 352 MHz RF reference frequency from the storage ring. An optical pulse from the laser amplifier that is seeded by the oscillator is delivered to the sample. With proper alignment spatial overlap between the optical pulse and the X-ray pulse onto the sample can be achieved. Notice that repetition rate of the synchrotron radiation is locked to the 352 MHz frequency as well. Therefore we can achieve timing synchronization between the X-ray pulses and the laser pulses	34
3.1	Schematics of 3 Dimensional Stresses in Cartesian coordinate	39
3.2	Calculated spatial dependence of the strain based on Thomsen's thermo-elastic model at different times following optical absorption [6].	41
3.3	Temporal evolutions of photo-excited carriers with carrier and thermal diffusion processes taken into account.	44
3.4	Arrays of atoms in a lattice structure can be viewed as a chain in which masses are connected by springs	47

3.5	Propagation of Electromagnetic waves in free space	49
3.6	The path difference of scattered radiation between atoms at separation r	51
3.7	Propagation of Electromagnetic waves in free space	53
3.8	Propagation of Electromagnetic waves in free space	54
3.9	Solution to the Takagi-Taupin equation can be obtained by calculating solutions at each layer or mesh points	56
4.1	1.5 μm AlGaAs/GaAs epitaxial sample grown on (001) GaAs substrate was used in this experiment. Figure on the right shows a static X-ray diffraction trace from the sample. Two individual (004) Bragg peaks are clearly resolved.	64
4.2	Energy band diagram of GaAs and AlGaAs. Band diagrams themselves do not look much different for those two alloys. Nevertheless their electronic structures are quite distinctive. For GaAs at room temperature $E_g = 1.42$ eV, $E_L = 1.71$ eV, $E_X = 1.90$ eV. For AlGaAs $E_g = 1.80$ eV, $E_L = 1.92$ eV, $E_X = 1.95$ eV.	65
4.3	Intensity of the X-ray diffraction (measured relative to before excitation and normalized to the maximum) following femtosecond laser excitation above the gap in the GaAs substrate. Three different angles near the (004) Bragg peaks are shown: (a) 27.546° , on the high angle side of the AlGaAs peak; (b) 27.5415° on the low angle side of the AlGaAs peak; and (c) 27.5690° on the low angle side of the GaAs peak.	67
4.4	Simulation of the strain as a function of depth at four different time-delays following laser-excitation where the energy is deposited in a thin region of the GaAs substrate. A simple thermoelastic model is used in which the strain is due to differential thermal expansion and diffusion is slow. An elastic response is generated which travels at the longitudinal speed of sound. The transmission coefficient for the pulse at the heterostructure interface is unity and the reflection coefficient at the free surface is -1. Notice that a unipolar compression pulse propagates through the AlGaAs film, reflects off the free surface becoming a tensile pulse, and later transmits into the GaAs substrate.	68

4.5	Time and angle resolved X-ray diffraction from AlGaAs film showing the propagation of a short acoustic pulse that was generated in the GaAs substrate. Experimental data are on the left and a simulation in which strain is incorporated into dynamical diffraction theory is on the right.	71
4.6	Data acquisition layout of time resolved X-ray counting scheme. APS counts are collected before, during, and after incident of the laser pulse to the GaAs crystal. Total counts are also being collected to give us a normalization factor.	74
4.7	Pulsed radiation source, which has time-dependent intensity behavior, may require dead time loss correction	75
4.8	Rocking Curve about (004) reflection. Plot shows the comparison between data set with and without dead time correction.	75
4.9	Propagation of a strain pulse in AlGaAs epitaxial film layer. Peak of Bragg peak shift accordance with lattice spacing changes.	77
4.10	Simplified version of band gap of direct semiconductor [7]. Figure shows various energy relaxation routes of photo-excited carriers. (1) carriers are initially excited optically from valence to conduction band. (2) FCA process where excited electrons are once again excited by incident photons and promoted deep into the conduction band. (3) Non-radiative recombination. (4) Auger recombination process where excess energy of an electron is transfer to another carrier as it recombines with holes. (5) Luminescent transitions (6) trapping of free carriers and (7) recombination.	82
4.11	Amplitude of strain pulse saturates at high laser fluence levels. Plot on left shows propagation of strain pulse in AlGaAs at different laser fluence. Plot on right shows how maximum amplitude of the strain pulses varies depending on the fluence. This optical limiting effect is credited to free carrier absorption process, which may be better known as free carrier absorption.	84
4.12	After accounting for both the interband absorption and the free carrier absorption by its cross section, numerical model now simulates the optical limiting effect.	85

4.13	Numerical model still does not predict the data even after the saturation in carrier density has been taken into account. Notice that ratio between the compression pulse and the tensile pulse in the film layer drastically deviates from 1 at high laser power. Also notice that there is considerable heating effect at higher laser fluence, which develops relatively slowly within 1 ns period in the GaAs substrate.	88
4.14	After incorporating free carrier interband absorption, numerical model follows the experimental data much closely. Top left shows the strain propagation in AlGaAs and bottom left is the simulation. Accordingly top right shows the strain generation and propagation in GaAs substrate and bottom right is the numerical counter-part.	89
4.15	long term thermal bahvaior of the multilayerd struecute. Initally as heated surface of the GaAs substrate cool down the film layer begins to heat up as heat energy gets transmitted through the interface. Eventually both systems come to a thermal equilibiirum.	90
5.1	Two types of X-ray scattering setup. Figure on left shows a point detector scheme, while figure on right shows imaging scheme to study phonons. Through out most of the work covered in the thesis, first method was used.	94
5.2	Imaging of thermal population of phonons in (100) GaAs crystal. This phonon image was taken back in 2003 when we were still trying to use imaging method to study laser induced phonon dynamics.	96
5.3	Rocking curve of InSb about 111 reflections. Slight deviation on HKL space is due to systematic error in orientation matrix. Nevertheless for our application, the deviation can always be accounted for during error analysis.	97
5.4	2D (reciprocal space along (111) and time) scan about (111) Bragg reflection in InSb. We are able to observe coherent lattice vibrations slightly away from Bragg condition (zone center). Oscillations too far off the zone center cannot be resolved due to limitations in current probe pulse duration.	99
5.5	Time scans in InSb at particular wave vector, $q = 0.0007$. Basically each line out of Figure 5.4 should look like this except lower q value corresponds to oscillation at lower frequency: High q means higher frequency.	100

5.6	Experimentally observed oscillation frequency vs. wave vector. The slope should give out the group velocity of LA phonons along [111] direction. Dispersion relation of the material near zone center has been mapped out.	100
5.7	2D (Reciprocal space vs. Time) scan about (111) InSb Bragg reflection. The scan was taken along (1-10) direction, which is perpendicular to previous scan direction. Presence of oscillatory behavior of lattice on this orthogonal vector direction suggests that impulsively generated strain may not be uniaxial.	101
5.8	Experimentally observed oscillation frequency vs. wave vector along [1 -1 0]. The slope gives out the group velocity of TA phonons potentially along any direction.	102
5.9	Temporal evolution of laser induced phonon frequency spectrum at low LA branch. Initial bandwidth of the mode is narrow [see top left], but it becomes broad as time progresses. And also center of the frequency slowly toward lower frequency region.	103
5.10	Laser induced effect on lattice dynamics extends far more than what we just demonstrated. Current experimental scheme is capable of studying phonon dynamics at up to frequency of 0.5 THz where treatment of continuum dynamics of lattice dynamics will break down. .	104
5.11	Theoretical prediction of phonon population distribution upon ultra-fast laser excitation. The colored scale on the right side of the contour figure gives the p phonon density. The non-equilibrium phonon population has a preferential decay direction along K. Other less dense non-equilibrium phonon populations may also be observed in our experiment [8][9].	105
5.12	Three zone boundary regions were chosen for the counting experiment. As time progresses error bar becomes smaller as our statistics gets better. On first two sites, the ratio basically converges to 1. Nevertheless on zone boundary along [1 1 1] direction, there is a considerable laser induced effect.	106
6.1	Taking Static Images with X-rays. Floral Radiography. X-rays are used to take still picture of flower. Differential transmission of X-rays through the flower is imprinted on to X-ray film [10].	108

6.2	Making Movies with X-rays. Fast time dynamics such as fuel-injection system can be studied with time-resolved X-ray technique. Researchers at Argonne National Laboratory can monitor amount of X-ray energy that is absorbed by the fuel spray. Micro-second dynamics of fuel spray cannot be probed with optical method [11]. . .	109
6.3	A streaked image of an 10KeV X-ray bunch measured with a X-Ray streak camera on April 4, 2003. The detector is developed at David Reisař group at the University of Michigan. A FWHM of 60ps was measured.	111
6.4	A compact streak camera developed in David Reisař group at the University of Michigan. X-Ray pulse incidents upon a CsI photocathode, which subsequently emits secondary electrons. The electrons are then accelerated by an applied electric field down the bore of the detector. The rising edge of a voltage pulse is applied to the deflection plates as the electron bunch passes by. Electrons arriving at separate times experience a different deflection voltage, and thus the electron bunch become streaked. The bunch is later amplified and imaged by micro-channel plate, phosphor screen and a CCD. . .	112
6.5	Schematics of the slicing source that are under development at Advanced Light Source [3].	113
6.6	(a) The bright band in each column is the electro-optic signal, and its location indicates the time of arrival of the electron bunch with respect to the laser probe pulse and the width corresponds to the electron bunch duration. (b) Normalized arrival time histogram of 1000 consecutive single shots.	114
6.7	Time-Resolved X-ray pump-probe data taken at SPPS by David M. Fritz during summer of 2005. Using a novel timing scheme developed by Adrian et al [12], lattice dynamics occuring at sub-picosecond time scale can now be observed at an accelerator-based facility. Latest technologies in ultrafast X-ray field will soon give us sufficient tool to test our fundamental understanding of condensed matter physics.	115

LIST OF APPENDICES

Appendix

A.	Structural Factor Calculation	119
B.	Matlab Code for GaAs Dynamical Matrix Calculation	126
C.	Physical Parameters of GaAs	134

CHAPTER I

Introduction

In this chapter, I present experimental motivation and method for studying semiconductor dynamics upon ultrafast laser excitation. I go over the theoretical basis of the physics and introduce numerical simulations and experiments that were conducted prior to my research. Ultimately, I explain how novel techniques of time-resolved X-ray diffraction can be used to study responses of an optically excited condensed matter system.

1.1 Underlying Physics of Semiconductors// Upon Ultrafast Laser Excitation

In optically opaque materials such as semiconductors, a significant amount of optical radiation can be absorbed near the crystal surface. An incident photon with energy greater than the energy bandgap of the semiconductor creates electron and hole pairs. The free carriers are normally generated near the surface within the optical absorption depth, which typically ranges from $0.1\sim 1\text{ }\mu\text{m}$. Excess energy from the free carriers is released through various recombination processes. In a radiative recombination process, such as band to band recombination or recombination in-

volving excitons, the released energy results in emission of photons. On the other hand, in non-radiative recombination processes, such as R-G center recombination and auger recombination, the released energy generates thermal energy and produce lattice vibrations. With laser oscillators and amplifiers, considerably high carrier density ($10^{17} \sim 10^{21}/cm^3$) can be produced. Under heavy excitation ($10^{18}/cm^3$ or greater), the spontaneous excitation and recombination of electron and hole pairs are dominated by the non-radiative recombinations [13, 14, 15]. In a typical III-V semiconductors such as GaAs or InSb, the relevant electron to phonon interactions are polar optical and acoustical deformation potential scattering [13, 14, 15, 16, 17].

The dynamics of the carrier excitation and relaxation processes have been subjected to numerous experimental and theoretical investigations during past decades [18, 19, 20, 21, 22, 23, 24]. Impulsively generated acoustic pulses and thermalization process have been the primary subjects of study in the time-resolved condensed matter community. The thermalization of photoexcited carriers upon laser excitation has been looked into in earlier photoluminescence experiments [25]. Electron and hole velocity distributions and heating distributions have been studied by a scattering experiments [26]. Recently impulsive excitation and phase sensitive detection of coherent phonons has been explored through optical pump-probe techniques with femtosecond time-resolution where a coherent phonon mode and free carriers are excited simultaneously. Relevant information regarding the carrier to phonon interaction has been further investigated [27, 28, 29, 30]. However, quantitative measurements of the impulsive strain and detailed knowledge of the thermalization processes are

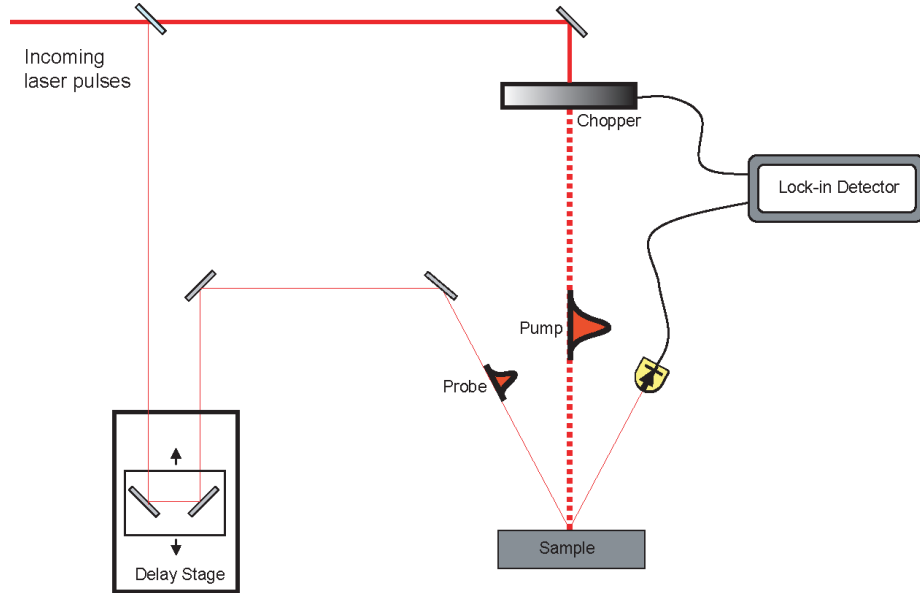


Figure 1.1: Typical set up for the time-resolved all optical detection of coherent phonons oscillations. We send an additional laser pulse following a pump-pulse with variable time-delays. By measuring amount of reflected light at each time delay, we can probe the dynamics over the entire cycle of the system. The time-resolution in this scheme is typically in orders of tens to hundreds of femtoseconds

still lacking. Typically, our understanding is based the assumption that the energy relaxation takes place on much shorter time scale compared to the acoustic transit time in the crystal medium. Under this assumption, the energy transfer from the energized electrons to the lattice occurs instantaneously. Thus the current numerical models that predict semiconductor response upon ultrafast laser excitation ignores the intricate energy relaxation dynamics that are mentioned in previous paragraphs. In this thesis, I formulate much more detailed and accurate understanding of impulsive strain generation and propagation. The motivation comes from fundamental research as well as development of new semiconductor devices and semiconductor processing techniques such as in-situ/non-invasive sample measurement and laser annealing [31, 32, 33, 34].

1.2 Relevant Experiments

1.2.1 Optical Pump Probe Methods

We use time-resolved techniques to observe transient dynamics occurring in solids in fast time scales. In an optical pump-probe experiment, time-resolved detection of transient phenomena on variable time scales (ranging from microseconds down to possibly sub-femtoseconds) is possible. In a typical pump-probe experiments, one creates an event by applying a laser pulse to a sample and thus pumping it. When the sample is excited, its lattice dynamics is initially disturbed from its equilibrium state. After certain period of time, the system eventually comes back to the equilibrium. This experimental scheme is applicable for studying repeatable excitation processes such as the photoexcitation of carriers in semiconductors. By systematically sending an additional laser probe pulse with fixed time delays from the pump pulse and then by measuring amount of the reflected probed light at each time delay, one can observe temporal evolution of lattice movement over the entire cycle of the system (See Figure 1.1).

In these experiments, the time-resolution is defined by the minimal distinguishable separation between pump and probe pulses, which is typically about 100 fs with modern laser systems. The time-resolution allows detection of non-equilibrium phonon dynamics upon ultrafast laser excitation in 100 fs time scales [1]. It can also be used to study propagation of ultrafast acoustics pulses [35, 36]. Nevertheless the measurement of atomic displacements or directly determining the amplitude of the strain is not possible because the wavelength of laser radiations is much longer

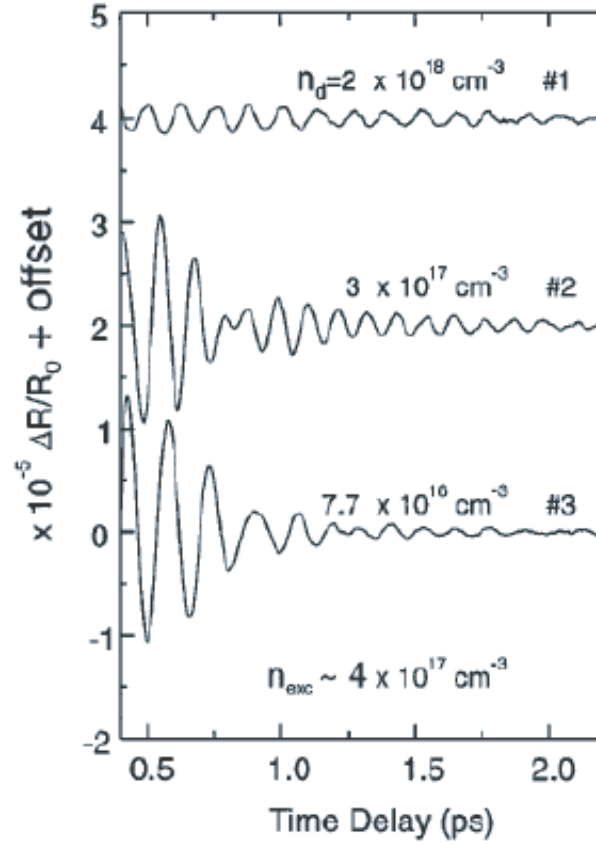


Figure 1.2: Isotropic reflectivity changes measured with optical pump-probe methods. Data displays different oscillatory behaviors depending on doping level in the sample [1]. Despite sub-picosecond time-resolution, one cannot directly deduce how much the lattice moved.

than atomic spacings in a typical crystal. For instance, Figure 1.2 shows observation of oscillatory behaviors of the lattice in GaAs upon short laser excitation in picoseconds time scales. However, we cannot quantitatively measure how much the lattice moved. Furthermore, the optical probe is only sensitive to dynamics occurring within the optical penetration depth. More versatile and effective probe is necessary to study overall bulk dynamics or multilayer samples.

1.2.2 Time-Resolved X-Ray Scattering Experiments

Since the discovery of X-rays by Rontgen in 1895, X-rays have been used to study structural properties of condensed matter systems on atomic length scales. Probing with X-rays yield direct information about atomic positions of the materials. X-rays also penetrate considerably deeper than optical probes thus allowing study of bulk materials. Furthermore, the wavevector of the X-rays are large enough to probe the entire Brillouin zone in reciprocal space.

By the early 1980s, scientists have begun to incorporate X-rays in time-resolved experiments [37, 38]. In earlier experiments, due to relatively poor time-resolution and count rate, it was difficult to study detailed lattice dynamics in fast time scales. The time-resolution was mostly limited by speed of the electronics while the data acquisition rate was severely constrained by the number of photons from X-ray tube sources. With the arrival of powerful femtosecond laser technologies, laser driven plasma sources were built to produce hard X-ray photons. The first hard x-ray source (1.6 KeV) with picosecond time-resolution has been demonstrated by Rischel et al. [39]. The plasma source provides sufficiently short X-ray pulses to probe fast

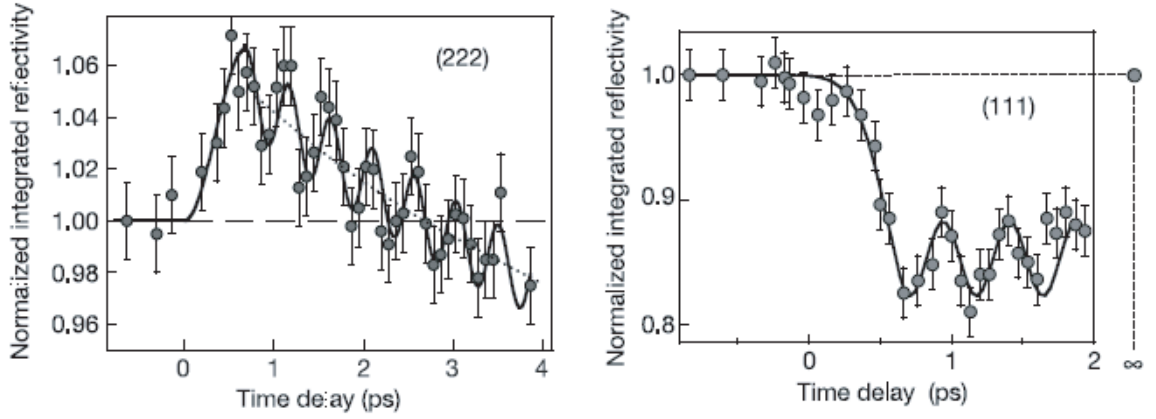


Figure 1.3: Transient changes in X-ray diffraction efficiency upon ultrafast laser excitation at two different reflections (111) and (222) in Mismuth crystal is measured with plasma based source [2]

lattice dynamics without relying on the time-resolution of detectors and electronics. Since then, development of more advanced plasma sources achieved subpicosecond time-resolution. The improved ultrafast source of X-rays were used to study fast phase transition [40, 41] and coherent atomic displacement of the lattice in solids [2] where Sokolowski-Tinten et al [2] have successfully demonstrated a periodic modulation of the X-ray diffraction efficiency caused from excitation of coherent optical phonons (See Figure 1.3). Nevertheless, the plasma source based experiment still suffers from low count rate and thus requires X-ray focusing optics, which degrades the monochromaticity of X-ray beam such that obtaining real atomic spacing information becomes unfeasible. And also, even with the incorporation of the focusing optics, the acquisition time often exceeds single days for a single sample or set of excitation conditions. For these reasons time-resolved X-ray experiments at synchrotron facilities had received much attention.

Third generation synchrotron radiation facilities such as Advanced Photon Source

(APS) continuously produces many orders more X-rays than the tube sources. The synchrotron X-rays are monochromatic and have negligible spatial divergence. Furthermore, X-ray beams at APS is intrinsically pulsed, which is ideal for doing time-resolved experiments. By late 1990s, in a very few national facilities such as Advanced Light Source (ALS) and APS, femtosecond laser pumped and synchrotron X-ray probed set ups were implemented. In one of the experiments performed at the ALS, Lindenberg et al. [3] studied InSb system with sub 10 ps time-resolution using a streak camera. In their work, oscillation periods of the optically excited acoustic phonon modes were measured (See Figure 1.4). From this data, they were able to extract wavevector information and later constructed a dispersion relation for the laser induced phonon populations. In this experiment, the thermoelastic model failed to match the experimentally obtained values until electron to phonon coupling time was included. In another synchrotron based experiment at APS, Reis et al [4] reported on the modulation of X-ray diffraction from (111) InSb due to impulsively generated acoustic phonons and were able to quantitatively characterize localized strains at different times. They were able to make a direct comparison between the experimental data and the simulation (See Figure 1.5). They found out that the energy partition from the pump pulse to the lattice cannot be accounted for based on the thermoelastic model. Inclusions of various delicate processes such as carrier diffusion, recombination and thermal diffusion were necessary to correctly predict the time-resolved behavior of the InSb crystal upon ultrafast laser excitation. In above examples, TRXD shows when and where the thermoelastic models can be

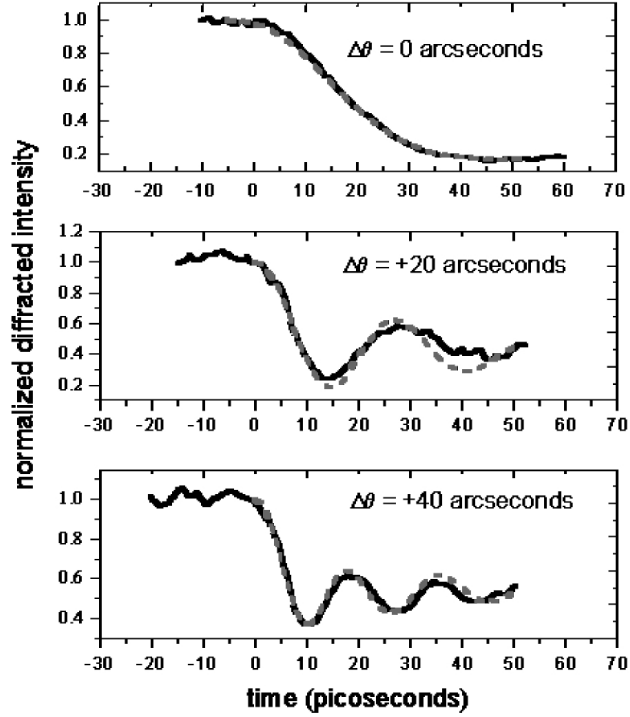


Figure 1.4: Time-resolved X-ray diffraction efficiency measured at different angles about InSb Bragg peak. Despite 100 ps time-resolution at ALS, sub 10 ps dynamics were measured using X-ray streak camera [3].

used. The results signify that the thermoelastic model and mere verification from optical measurements are not sufficient to explain intricate dynamics in the crystal upon femtosecond laser excitation.

1.3 Thesis Motivation and Organization

In this thesis, I make quantitative measurements on how the energy from optical excitation relays down to generation of impulsive strain and heat in various materials. In chapter 2, I present experimental apparatus and schematics that are used in my time-resolved X-ray diffraction measurements. And then, I elaborate on theories and numerical models to simulate the data in chapter 3. In chapter 4, relative strength of thermal expansion and volume deformation potential are calculated and compared

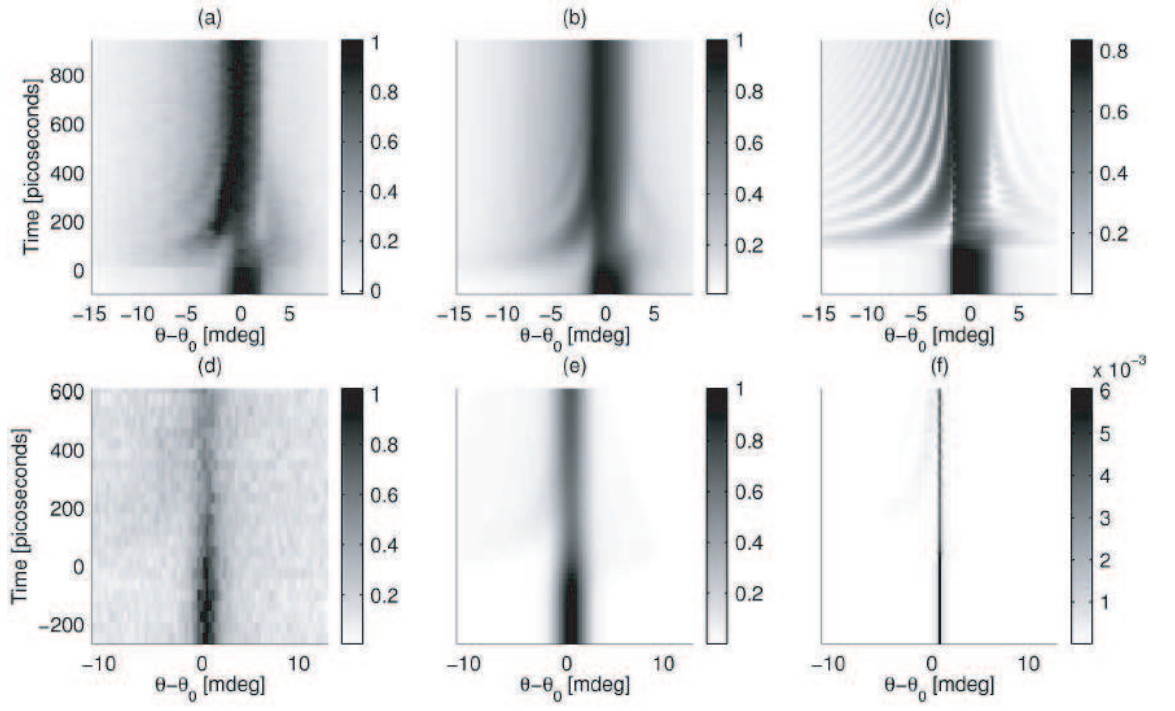


Figure 1.5: Time-resolved rocking curves of impulsively strained InSb crystal. (a), and (d) are collected sets of data and (b) and (e) are result obtained from numerical modeling to simulate the temporal evolution of strain inside the crystal [4].

to the data. Unpredicted behavior of the strain from varying pump fluence is also presented. In chapter 5, I study strain and phonon interactions beyond the assumption of uniaxial property and continuum dynamics. By fully extending the capability of the synchrotron X-ray based pump probe method, dynamics of large wave vector phonons (upto terahertz), are investigated. Finally in chapter 6, limitations of current time-resolved methods will be addressed and possible solutions are introduced. In conclusion, I make discussions about how upcoming X-ray technologies should further aid us to explore condensed matter physics in unprecedented precision and time-resolution.

CHAPTER II

Experimental Setup

Time-resolved X-ray diffraction (TRXD) measures two different facets of lattice dynamics: time and space. The measurement requires specialized tools and knowledge from two different experimental fields, optical pump-probe and X-ray scattering. TRXD experiment requires pulsed laser and pulsed X-ray sources that are synchronized to each other, which can be done at very few places around the world. It is also necessary to spatially and temporally overlap the laser and X-ray pulses on the sample and to control the time delay between them. The timing aspect of the TRXD closely resembles that of the optical pump-probe experiment while the techniques of spatial analysis of the sample follow procedures that are laid out for X-ray diffraction. In following chapters, the relevant apparatus for TRXD experiments at the X-ray synchrotron are described. In particular, I explain synchronization between X-rays and femtosecond optical pulses in detail.

2.1 Laser Pumped and X-ray Probed Experiment

In a TRXD experiment, X-rays are delivered to the sample, and then the laser pulse is directed onto the X-ray spot. Given that the temporal delay between the

pulses is sufficiently longer than the system's recovery period, the initial X-ray diffraction pattern represents the lattice dynamics at a thermal equilibrium. For example, one would expect to see a rocking curve about the Bragg angle. However, once the time delay is adjusted such that the X-ray and the laser pulses are temporally overlapped, X-rays now interact with the lattice that has been excited by the optical radiation. Therefore, important crystal parameters such as the lattice spacing change drastically and the position of the Bragg peak changes accordingly. As we systematically scan the X-ray pulse arrival time with respect to the laser pulse, the lattice system eventually has enough time to return to its equilibrium state. By recording the angular position of the Bragg peaks at each time delay, the time resolved data set from a photoexcited material is obtained.



Figure 2.1: The Advanced Photon Source(APS) at the Argonne National Laboratory provides this most brilliant X-rays for research in various scientific disciplines such as biology, chemistry, physics and ect.

Most of the experiments presented in this thesis were performed at the Advanced Photon Source (APS) (See Figure 2.1). APS is a source of the most brilliant X-

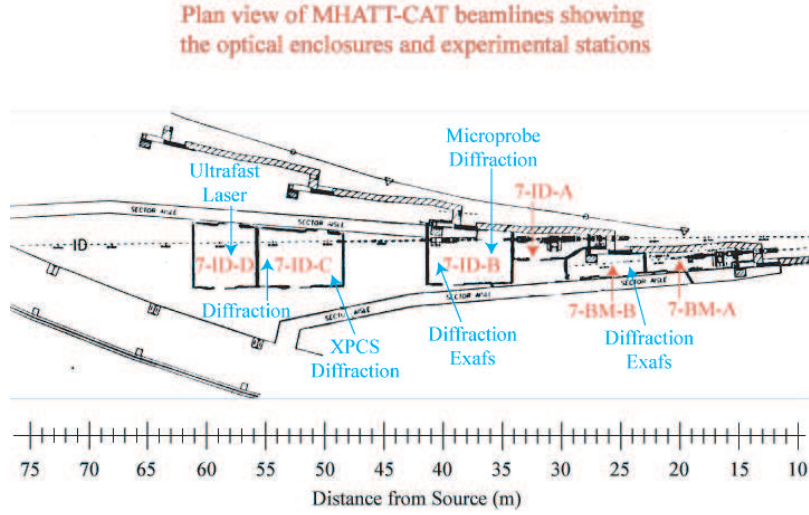


Figure 2.2: Experimental floor layout at MHATT/XOR sector 7 insertion beamline.

ray beams to study various interdisciplinary subjects, such as biology, atomic and molecular physics and condensed matter systems. APS is comprised of 37 beam lines (currently growing) with several experimental endstations, or hutches on each beamline. Among the beamlines, MHATT-CAT/XOR at sector 7 has a unique set up where the simultaneous delivery of ultrafast amplified laser beam and X-rays is possible.

2.2 Overview of the Experimental Site

The experimental floor plan of sector 7 is shown in Figure 2.2. The monochromatic X-rays beams are produced at A Hutch. Three experimental hutches are subsequently connected through X-ray beam delivery pipe, which is maintained under vacuum to limit the loss of X-ray flux due to absorption in air. B and C hutches are separate experimental stations typically reserved for non time-resolved experiments, such as surface scattering, X-ray imaging, or characterization of X-ray optics. Approximately 40 meters down from the X-ray source, D-Hutch is configured for

time-resolved X-ray diffraction experiments. Inside the D-hutch, there is an amplified laser system that is precisely synchronized (within a few picoseconds) to the repetition rate of the X-ray pulses from the APS storage ring. The laser system begins with a seed laser, Ti:Sapphire oscillator, which generates femtosecond optical pulses at a central wavelength of 800 nm (1.55 eV). The output from the oscillator is amplified through a commercial Ti:Sapphire amplifier to deliver a few milli-Joule laser pulses that are compressed down to 100 fs FWHM or less.

The APS accelerator generates electron bunches that travel at a relativistic speed. Currently the FWHM of an electron bunch in time domain varies from as short as 30 to 150 ps. As the electron bunches pass through the undulator, X-ray bunches with identical temporal profile to that of the electron bunches are generated. As a result, we have X-ray pulses that are highly monochromatic and carry very small spatial divergence. Once we manage to spatially overlap the X-ray and the laser pulses on the sample, TRXD can be performed. Specific of key apparatus and procedure will be described in detail in later sections.

2.3 Synchrotron X-Ray Source

2.3.1 Background

The term synchrotron originates from a specific type of a particle accelerator. It has become a universal term for radiation generated from charged particles such as electrons traveling at relativistic speeds in artificially designed magnetic fields that keeps them in a circular orbit. Synchrotron radiation is emitted from the electrons traveling at almost the speed of light when its path is bent by a magnetic field and

was first observed in 1947 [42, 43]. Since then, many storage rings have been built around the world dedicated to the production of brilliant X-rays. As can be seen in 2.3, most advanced third generation light sources are able to produce 10^{12} times brighter X-rays than early lab based ones [44].

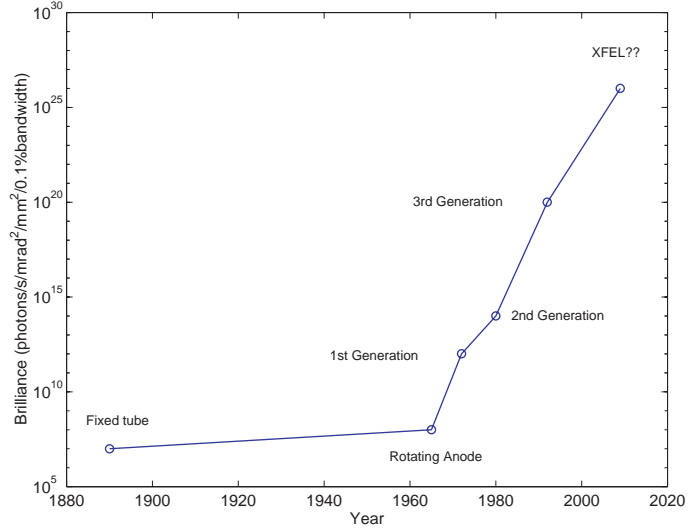


Figure 2.3: The brilliance of X-ray sources as a function of time. The brilliance of early lab source and each generation of synchrotrons are compared

2.3.2 Electron Accelerator and Storage Ring

The APS electron accelerator and storage system are the critical components for production of the high energy X-rays. Initially electrons emitted from a thermionic cathode are accelerated by high voltage alternating electric fields in a linear accelerator. Selective phasing of the electric field accelerates the electrons to 450 MeV. At this energy, the electrons are relativistic. The electrons are later injected into the booster synchrotron, a race-track shaped ring of electromagnets (See Figure 2.4), and then accelerated up to 7 GeV. In order to maintain the orbital path of the electrons, bending and focusing magnets increase the electric field strength in synchronization

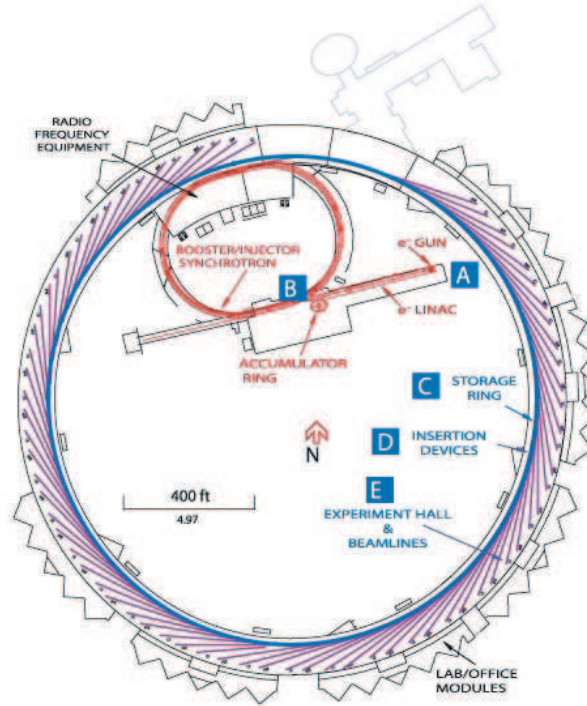


Figure 2.4: General layout of APS electron accelerator and storage ring structures. The schematic also displays the locations of the experimental hutches. Electromagnetic field from the electromagnets around the ring structure focuses the electrons into a narrow beam that is bent on a circular path within vacuum chambers running through the centers of the electromagnets.

with the RF field. The 7 GeV electrons eventually are injected into the 1104 meter circumference storage ring consisting of more than a thousand electromagnets and associated equipments.

2.3.3 Temporal Properties of Electron Bunch Structures

The synchrotron radiation from APS is pulsed due to temporal properties of the APS electron bunch structure (See Figure 2.5). The repetition rate of electron bunch structure is determined by RF frequency given from the linac to compensate for energy loss due to synchrotron radiation. Trains of electron bunches (approximately 15 ns long) are accelerated in the linac to 325 MeV from the injector gun into the

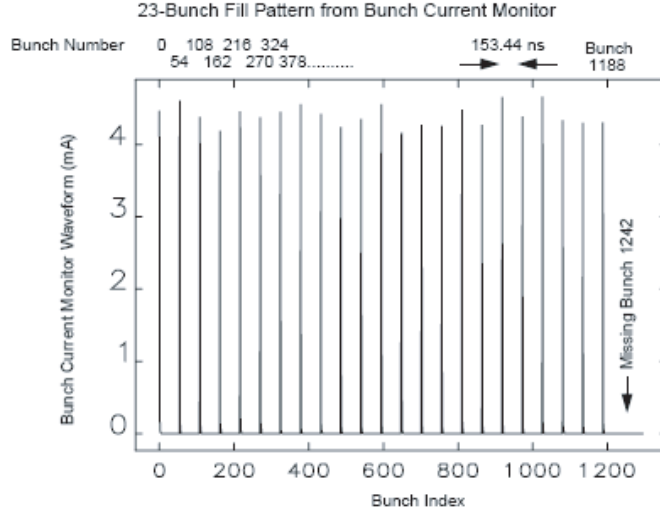


Figure 2.5: Fill pattern under standard operating mode at APS. 24 singlets with a nominal current of ~ 4.25 mA and a spacing of ~ 153 nanoseconds between singlets.

accumulator ring. The bunches are damped in transverse and longitudinal phase space coordinates and accumulated until an extraction is triggered. The bunch length at the extraction is about 1 ns. The extracted beam is injected into a booster ring that ramps the single bunch from 325 MeV to 7 GeV.

At the end of the booster cycle, the bunch is extracted and injected into the storage ring. At this point, the bunch can be injected into any of the 1296 RF buckets that are spaced by 2.842 ns. The storage ring master RF frequency of 351.972 MHz defines the bucket spacing of 2.842 ns. The circumference of 1.104 Km corresponds to a revolution frequency of 271.5 KHz (P0 frequency), which corresponds to a revolution of exactly 1296 buckets in 3.683 μ s. Under standard operating mode, which is used in most of my experiments, singlet bunch pattern at 102 mA of average current comes in a train of 23 bunches (16 nC/Bunch), each spaced by 153 ns. At the end of bunch train, there is a gap of 306 ns [45]. As we describe in section 2.6, the

electron bunch structure and storage ring RF frequencies are very important as they are used to achieve timing synchronization between the synchrotron-radiation and laser pulses.

2.3.4 Synchrotron Radiation

In a storage ring of synchrotrons such as APS, X-ray radiation is usually produced in bending magnets that are needed to keep the electrons in orbit, or insertion devices such as wigglers and undulators that are placed in the straight sections of the storage ring. We always used the latter. In an undulator, as the electron beam passes between the series of periodic magnets (See Fig. 2.6), it changes directions. The poles of the magnets alternate, so the electron beam wiggles left and right. Any wiggling electric charge emits electromagnetic radiation. The type of electromagnetic radiation produced depends on the frequencies at which the charge wiggles. Lower frequency wiggles can make radio waves or microwaves, while higher frequency wiggles can make X-rays. For our experiment, an undulator is used instead of wiggler. In both of these devices, an alternating magnetic field forces electrons to oscillate. However amplitude of the field in a wiggler is considerably larger and thus radiations from different part of wiggler adds up incoherently. On the other hand, the undulator emits radiation where at a given electron at one oscillation is in phase with the radiation from other oscillations. Consequently the amplitudes of the radiated waves are added and then the sum is squared to give out the signal intensity.

The condition to achieve the coherent superposition of x-ray radiations is shown in Figure 2.7. In the vicinity of M, one can approximate the cosine wave with amplitude

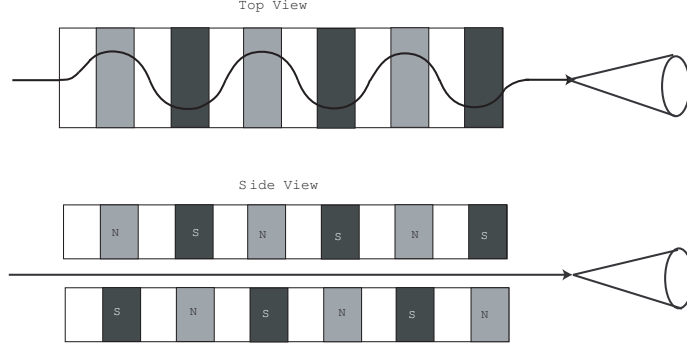


Figure 2.6: The alternating poles of an undulator create a series of small amplitude oscillations in a moving direction of electrons that emit synchrotron radiation at each pole. A certain fundamental wavelength is selected by the path length travel, which can be controlled by change the undulator gap.

A by circle with radius p as follows. That is,

$$Circular : x + (\rho - A) = \sqrt{\rho^2 - z^2} \rightarrow x \cong A - \frac{1}{2} \frac{z^2}{\rho}$$

$$Cosine : x = A \cos(k_\mu z) \rightarrow x \cong A - \frac{Ak_\mu^2 z^2}{2}$$

From this, we obtain a condition

$$\rho \cong (Ak_\mu^2)^{-1}$$

And then another condition to be met is the electron path length ζ for a single period of the undulator is given as,

$$\zeta \cdot \lambda_\mu = \int \sqrt{1 + \left(\frac{dx}{dz}\right)^2} dz \cong \lambda_\mu [1 + (Ak_\mu)^2/4]$$

There is a very delicate link between synchrotron radiation and relativity. Naively, one would assume that the wavelength of radiation from the undulator should be close to the array period of the magnets, which is about 30 million times off from X-ray wavelength. The explanation is given in terms of relativity. Imagine the

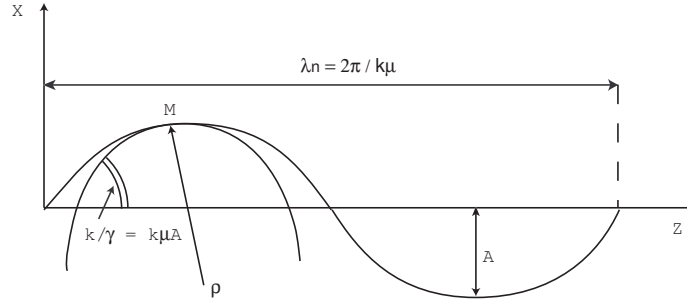


Figure 2.7: Properties of small oscillations for coherent generation of synchrotron radiation.

undulator seen by an electron that travels toward it. The electron is moving at near speed of light, thus it sees the undulator contracting along its length in its frame of reference (Lorentz contraction). Therefore, the emitted wavelength is reduced with respect to the undulator period. But also the emitted wavelength is affected by the relativistic Doppler Effect. As result, we are able to generate X-rays from the undulator periods. Consequently, the coherent addition of the radiation is only feasible at one frequency, fundamental wavelength of monochromatic x-ray beam, and its harmonics. The wavelength is tunable by changing the strength of magnetic field, which can be conveniently done by changing undulator gap [46].

2.4 Monochromator

Radiation from the undulator is extremely intense and carries spectral bandwidth of approximately 3%, which is too broad for a diffraction experiment. In order to obtain X-rays that are sufficiently monochromatic, additional filtering of the spectrum is required. At the output of the undulator, there are sets of white beam slits that are water cooled to dissipate the heat load. Typically at the sector 7, the emitted radiation is apertured to $500 \mu\text{m}$ by $500 \mu\text{m}$ through X-ray slits. Following

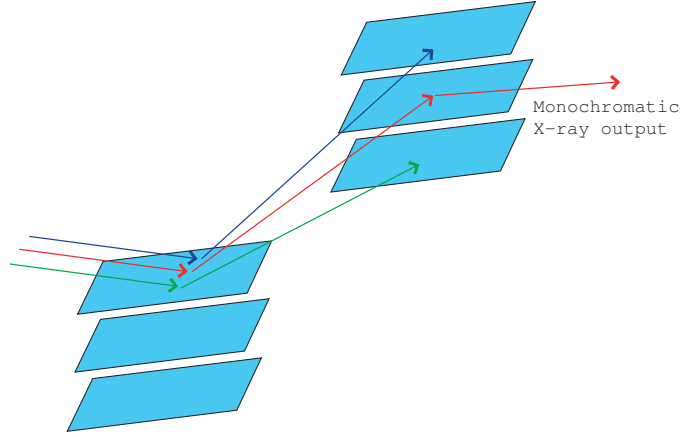


Figure 2.8: A double crystal monochromator. Polychromatic X-ray beam is incident on the first sets of lattice planes but only one wavelength satisfies two successive Bragg conditions.

the white beam slits, a cryogenically cooled double crystal Si (111) monochromator limits the spectral bandwidth. This device depends on two successive applications of Bragg reflections (See Figure 2.8). Depending on the lattice spacings of the first crystal, different wavelength components from the incoming beam are rejected at different outgoing angles. Among all components in the polychromatic beam, only a single wavelength that satisfies the Bragg condition is reflected toward parallel direction to the incoming beam. The monochromator finally outputs approximately 106 monochromatic X-ray photons per pulse at 10 KeV with energy deviation typically less than 1.4 eV, which corresponds to approximately 0.014%.

2.5 Laser System

The generation picosecond strain pulse requires a laser system that produces optical pulses with width less than the optical penetration depth speed of sound. Ti:Sapphire oscillator suffices this requirement. However to generate large enough strain ($10^{-5} \sim 10^{-4}$) that introduces significant deformation, an optical fluence

of a few $\frac{mJ}{cm^2}$ is required. Commercial laser amplifier provides the desired fluence with reliable stability. The laser system schematics inside the experimental hutch is described in following sections.

2.5.1 Ti:Sapphire Oscillator

Ti:Sapphire laser emits broadband near infrared light. These lasers are mainly used in scientific research where ultrafast optical pulses are needed. This unit is typically pumped with another laser with a wavelength of 514 to 532 nm and operates most efficiently at a wavelength of 800 nm. This laser is modelocked to produce trains of optical lights with short duration on the tens of femtoseconds. The basis of this modelocking technique is to induce a fixed phase relationship between the modes of the laser's resonant-cavity and thus produce short pulses.

A laser cavity consists of two plane mirrors facing each other (See Figure 2.9), surrounding the gain medium of the laser (a Fabry-Perot cavity arrangement). Light traveling between the mirrors of the cavity will constructively interfere with itself, leading to the formation of standing waves between the mirrors. Each of the modes in the standing waves will oscillate independently, with no fixed relationship between each other. It is essentially like a set of independent lasers all emitting light at slightly different frequencies. The individual phase of the light waves in each mode is not fixed. In lasers with only a few oscillating modes, interference between the modes can cause beating effects in the laser output, leading to random fluctuations in intensity. Normally, in lasers with many thousands of modes, these interference effects tend to average to a near-constant output intensity. The laser operation is

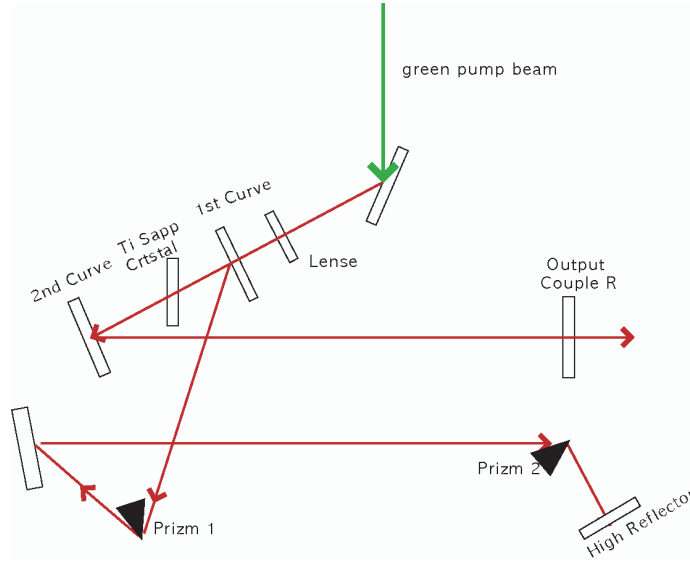


Figure 2.9: Design of KML oscillator system used in the experiments

known as a continuous waves (C.W.).

However, if each mode operates with a fixed phase between them, the laser output behaves quite differently. Instead of random or constant output intensity, the modes of the laser will periodically all constructively interfere with one another, producing an intense burst of light. Such a laser is said to be modelocked or phase-locked. These pulses occur separated in time taken for the light to make exactly one round trip of the laser cavity. This time corresponds to a frequency exactly equal to the mode spacing of the laser, $\delta\nu = \frac{1}{\tau}$. The duration of each pulse of light is determined by the number of modes which are oscillating in phase. If there are N modes locked with a frequency separation $\delta\nu$, the overall modelocked bandwidth is $N\delta\nu$, and the wider this bandwidth, the shorter the pulse duration from the laser. For example, for a laser producing pulses with a Gaussian temporal shape, the minimum possible pulse duration δt in a transform limited pulse duration is given by: $\Delta t = \frac{0.44}{N \cdot \Delta\nu}$, where the value 0.44 is known as the time-bandwidth product of the pulse, and varies depending

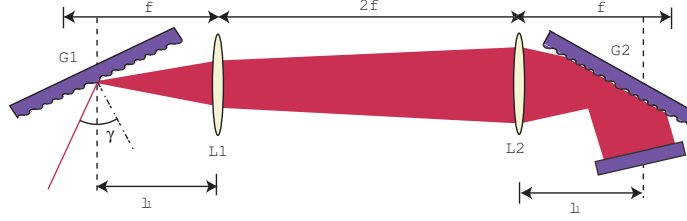


Figure 2.10: Grating-pair stretcher used to provide positive dispersion. Lenses (L1 and L2) are separated by twice their focal length. A reflector is used to fold the beam path. Difference in distance between the grating and lens and the focal length determines the total dispersion.

on the pulse shape. The Ti:Sapphire Oscillator used in our experiments follows Kapteyn-Murnane oscillator design pumped by a C.W. diode pumped solid state green laser (See Figure 2.9). The laser is capable of producing spectral bandwidth of 50 nm (25 fs FWHM transform limited) with average pulse energy of 4 nJ.

2.5.2 Amplified Laser System

Chirped Pulse Amplification (CPA) scheme amplifies the oscillator output pulse fluence up to a few $\frac{mJ}{cm^2}$. Architecture of the CPA laser system begins with a Ti:Sapphire oscillator described in previous section. The broadband ultrafast seeding pulse is directed to the grating pair pulse stretcher (see Figure 2.10) [47]. The grating pair is oriented such as longer wavelength components of the seeding pulse travel a shorter path than the shorter wavelengths, and hence they arrive at the amplifier stage sooner. The result is that a temporally stretched version of the seeding pulse heads on to the amplifier. Its duration is stretched out typically 20,000 times, and its amplitude reduced by an identical factor. The leading edge of the stretched seeding pulse is redder than its trailing edge with temporal profile of roughly 100 ps.

The stretching factor is defined by the effective grating separation $L = 2(l_g - f)$,

where f is the focal length of the lens and l_g , the distance from the lens to the grating. When l_g is equal to f , there is no dispersion, and when l_g becomes larger than f , the dispersion changes the sign. In practice, the lenses are replaced by a single spherical or parabolic mirror in a folded geometry, which eliminates chromatic aberration. Ignoring the amplifier for now, the pulse is recompressed using an identical parallel grating pair separated by $2l_g$ that introduces the opposite sign of chirp.

Amplification

Two types of Ti:Sapphire amplifier laser systems were used in my research. Until November 2003, a commercial multipass amplifier was used. The amplifier was designed to run at a 1 kHz repetition rate [48] (see Figure 2.11). In this scheme, a Pockels cell is used to inject a single pulse from the oscillator into the amplifier where it makes 8 passes with a slight offset at each cycle before being picked off and ejected.

Subsequent data in this thesis was taken with a new commercial system, which employs regenerative amplification scheme (See Fig 2.12), which replaced the multipass version. The new amplifier typically runs at a repetition rate of 1 KHz but also capable of running up to 5 KHz [49]. In this geometry the seeding pulse is injected into the amplifier using a fast-switching Pockels cells. This is performed by stepping the voltage in two stages, firstly by a quarter wave, in order to trap the pulse in the amplifier cavity and then up to a half wave for ejection. In our system, the pulse makes 12 roundtrips in the cavity before the gain is saturated.

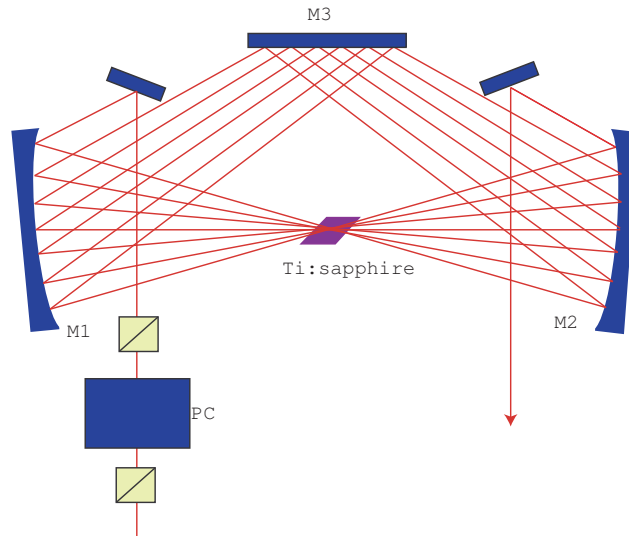


Figure 2.11: Multipass amplifier Design that was used at sector 7 prior to its decommission, which took place during our run in summer of 2003.

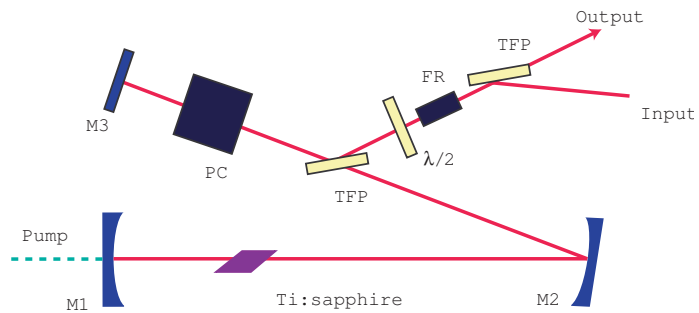


Figure 2.12: Current regenerative amplifier scheme from Positive Light. The unit is capable of delivering 30 fs pulse at average power output of 2.5 W.

Recompression

Out of the broadband amplifier, energetic chirped pulse is directed through a compressor grating pair. This is a pair of special reflective optical gratings oriented in such a way that longer wavelength components of the high energy chirped pulse travel a longer path through it than do the shorter wavelengths, and hence emerge from it retarded. The chirp which was initiated through stretcher stage is now undone. The spectrally broad energetic pulse emerging from the compressor optics now has all its spectral components occurring at the same instant [50][51]. Because of the extreme optical power densities, an amplified pulse from the compressor should not be directed through bulk optical matter such as windows at small beam diameters after the recompression stage.

2.6 Laser to X-ray synchronization

In the time-resolved experiments, synchronization between pump and probe is the most critical component because the time resolution of the experiments heavily depends on it. In an all optical pump probe experiment, timing synchronization between the probe (oscillator pulses) and pump (oscillator/amplified pulses) is perfect. However, for the time resolved experiments at the synchrotron, the pump (Amplified pulses) and probe (X-ray pulses) are not intrinsically synched to each other. Therefore, an active means of synchronization is required. Since the pulse duration of the X-rays at APS is typically 100 ps (FWHM), synchronization with precision less than a few tens of ps is sufficient to fully utilize time resolution of the probe.

Figure 2.13 shows a schematics of a laser to X-ray synchronization in the ex-

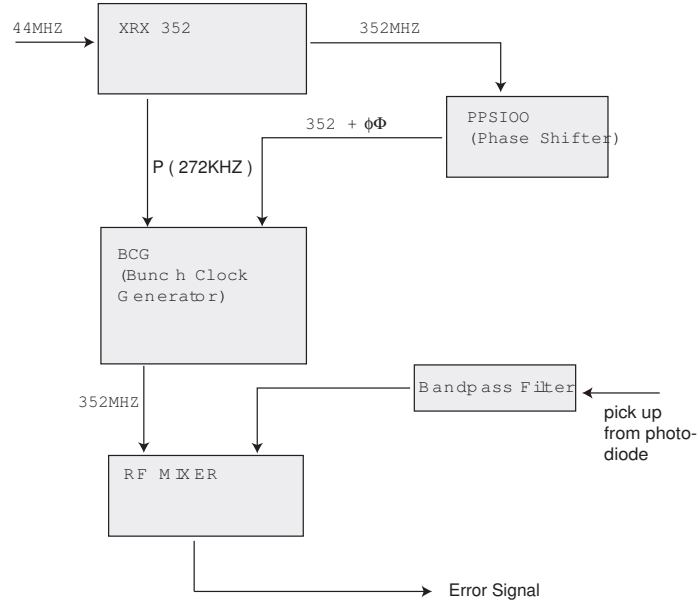


Figure 2.13: Laser to X-Ray Timing Synchronization Scheme. 44 MHz signal delivered from the storage ring facility is fed into the bunch clock generator (BCG) to reconstruct 351.9 MHz, which is mixed with 4th sub harmonic of the laser oscillator frequency. Error signal is used as a feedback to adjust the cavity length of the oscillator to minimize the error signal, thus locking laser system timing to the reference frequency of 351.9 Mhz.

periments. The reference RF signal for the timing system is provided by a master oscillator of the RF system for storage ring acceleration (351.9MHz). Since the source of the storage frequency is physically far away from the experimental site, it is necessary to distribute the RF signal to desired locations. In the APS timing delivery system, 351.9 Mhz is divided by eight to generated a phase related and frequency locked 44 Mhz signal. The 44 MHz is distributed via multi-mode fiber with affordable fiber optic components. Our experimental station has a phase-locked loop that multiples the 44 MHz to reconstruct 351.9 Mhz using BCG (See Figure 2.13 and 2.14).

The active synchronization scheme starts with the oscillator, which runs at 88MHz(4th subharmonic of the reference frequency). First an optical pick up from the os-

cillator pulse is fed into a fast rise time photodiode. The output of the photodiode is filtered through a 351.9MHz band pass filter where it is later mixed with the reference RF frequency. The output from the mixer is called error signal because it is directly correlated to the phase difference between two input frequencies. The error signal is fed into a feedback loop where high voltage is applied to the piezo-stage on the high reflector inside the oscillator to minimize the error signal. Thus the cavity length is always changing to phase lock two signals. Timing jitter between the RF and the laser is in order of a few picoseconds, which is negligible compared to the pulse duration of our X-ray probe at this time (~ 100 ps). Finally the laser amplifier is synchronized to a given subharmonics of the ring mater RF (See Figure 2.14).

By adding a phase to the reference RF, the relative delay between the laser and X-rays is controlled. The feedback system minimizes the error signal based on the modified reference signal ($351.9\text{MHz} + \text{Phase}$). This effectively changes the relative timing between the optical pulse and X-ray pulse. The minimal resolution of the phase shifter is about 20 ps, which is still acceptable given the pulse duration of synchrotron radiation. The maximum delay that the phase shifter can provide is 4.75 ns. A SRS535 digital delay generator provides arbitrary delayline for the optical pulse much longer than the limits of the phase shifter. This delay unit controls when the amplifier is triggered and oscillator pulse is amplified. A maximum delay of ± 1 ms can be achieved.

2.7 Detectors

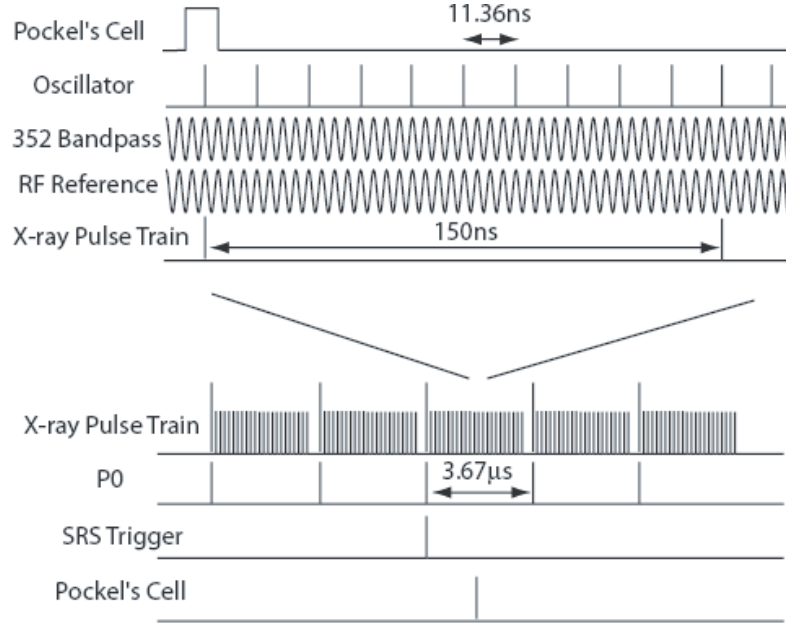


Figure 2.14: Overview of laser to synchrotron radiation timing at sector 7

2.7.1 Ion Chamber

When ionizing radiation such as X-rays passes through a gaseous medium, collisions with the gas molecules produces ion pairs. In most case, the chamber uses air as a gas medium. A DC voltage is applied between top and bottom parallel plates to create an electric field that attracts the ions to the oppositely charged plates (See Figure 2.15). Typically one of the plates carries high electric potential with respect to ground so that the circuitry is near ground potential. The other plate is usually held near zero volts and the resulting current is measured. Output from the ion chamber goes through current amplifier and voltage to frequency converter into data acquisition system. Due to large input area and easy usage the ion chamber is perhaps the most convenient tool to measure average integrated X-ray flux.

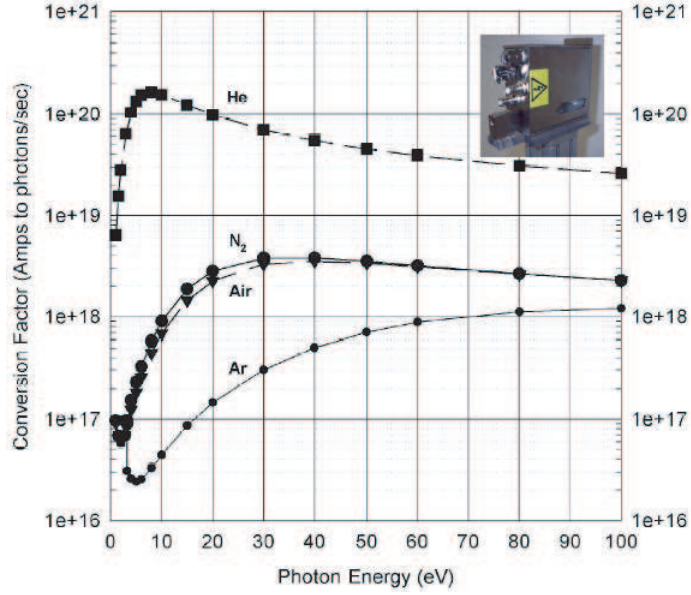


Figure 2.15: Ion chamber outputs current calibrated to number of X-ray photons. Figure taken from [5]

2.7.2 Avalanche Photo-Diode (APD)

In order to perform a time-resolved experiment with pulsed x-ray source, the synchrotron source such as APS requires X-ray detectors that are capable of picking out a single X-ray pulse from the train. Under normal operation mode, the time delay between individual pulse is about 150 ns, and thus a relatively fast rise time detector such as silicon Avalanche Photodiode (APD) is required. The rise time of typical APD is about 5 to 10 ns that is sufficient enough to distinguish between individual bunches (see Fig 2.16). For our experiments a windowless Advanced Photonix APD (SD 197-70-73-520) was used. However because APD is sensitive to optical infrared light, i.e. laser radiation, it is necessary to cover the APD with a thin aluminum foil.

In general this particular APD design can be used in either normal linear proportional mode at low gain, or in a single photon-counter mode. Latter one was

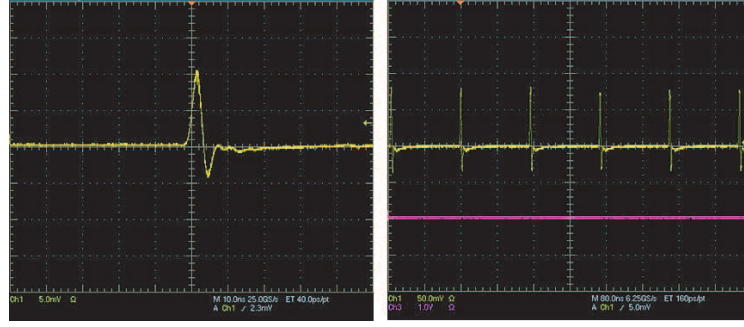


Figure 2.16: First figure (on left) shows typical rise time of APDs (5~10ns) that were used in the experiment. In this case APD was running under single photon counting mode. Figure on right was taken from APD under normal linear mode, and it shows X-ray pulse trains under standard fill pattern operation mode. The spacing between each singlet is approximately 150ns

used extensively in most of my experiments to deal with non-negligible systematic background from APD itself and gated integrators used for data acquisitions. In order to maintain high photoelectron detection probability only from X-rays, it is necessary to set detection threshold at proper value. Details of how single photon counting APD is incorporate into the experimental setup is elaborated in Chapter 4.

Diffractometer

Collecting diffracted x-rays from a crystal requires several degrees of freedom, which needs to be controlled with high degree of accuracy and repeatability. At the sector 7 D-Hutch, we have a Huber diffractometer that provides virtual Eulerian four-circle geometry (See Figure 2.17), which allows three degrees of freedom for the sample movement and an extra one for the detector. The four degrees of freedom allow arbitrary choice of reciprocal space coordinates h,k,l and either incident or exiting x-ray detection angle.

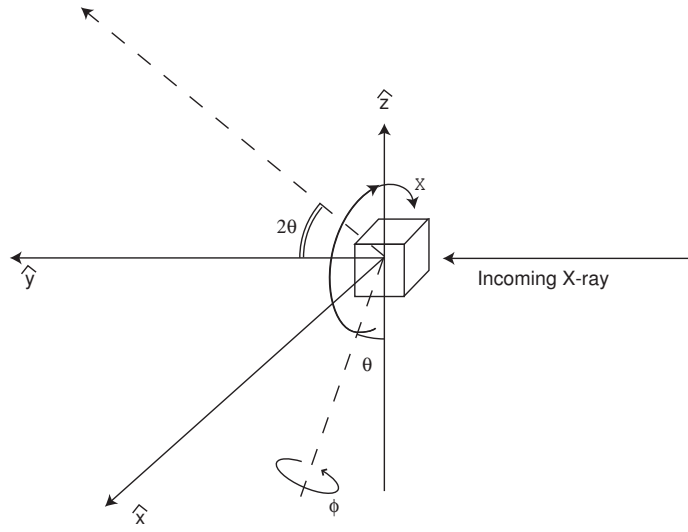


Figure 2.17: The HUBER diffractometer used in the experiment has four degrees of freedom in movement.

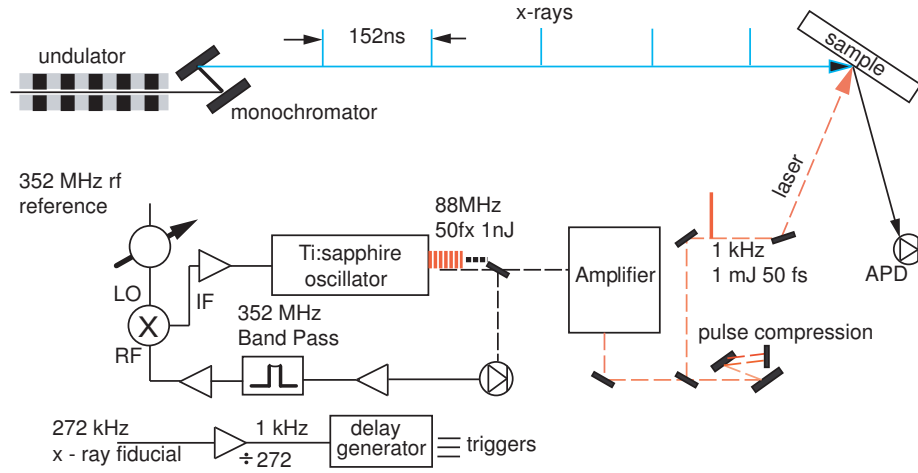


Figure 2.18: Experimental layouts at D-Hutch. Ti:Sapphire laser oscillator is synchronized to master 352 MHz RF reference frequency from the storage ring. An optical pulse from the laser amplifier that is seeded by the oscillator is delivered to the sample. With proper alignment spatial overlap between the optical pulse and the X-ray pulse onto the sample can be achieved. Notice that repetition rate of the synchrotron radiation is locked to the 352 MHz frequency as well. Therefore we can achieve timing synchronization between the X-ray pulses and the laser pulses

2.8 Expected Improvements

Most important aspects of the time-resolved diffraction experiment are the time resolution of the probe, the synchronization between pump and probe pulses, and the precision of diffractometer movement, which defines how accurately we can analyze the material in reciprocal space. Currently, even with recent repair and addition of encoders, the Huber goniometer is not functioning optimally. Its minimum resolution of movements is actually limited by the driver resolution. In order to fully utilize the capability of the device, upgrade of the driver is necessary. I note that the time-resolution of the synchrotron radiation is not always limited to 100 ps. It varies depending on the fill patterns and how much charge is contained in each pulse. Under 1296 bunch mode, there are 1296 uniformly spaced bunches with a nominal current of 0.08 mA and a spacing of 2.85 ns between bunches. With considerably less charge compared to that of 24 bunch mode (4.25 mA), we expect that pulse duration of the X-rays can be reduced as short as 20 to 30 ps FWHM. We could, therefore, obtain much better time resolution than present. Given shorter probe pulse duration, it is also necessary to come up with a more precise timing system. The 10 ps timing jitter between the pump and the probe as well as the minimally resolved time step with phase shifter require significant improvement. Issues involving the timing jitter in the pump probe system will be continuously addressed as more advanced synchrotron based X-ray source begin to emerge, which will be described in chapter 6.

CHAPTER III

Theory

I use three theoretical tools for analyzing and simulating laser induced dynamics in the crystals: a modified thermoelastic model, dynamical matrix for generating dispersion relation, and dynamical theory of X-ray diffraction. Typical wavelength of the phonon that constitutes the propagating strain pulse is much longer than the lattice parameter of a solid. I use the modified version of the thermoelastic model to simulate the propagation of impulsively generated strain pulses in a bulk material as well as at the heterostructure interfaces. Subsequently, the changes in the X-ray diffraction patterns due to the deformed lattice parameters are simulated by using dynamical theory of X-ray diffraction. Results from the simulation and the experimental data are compared to examine the theory. Nevertheless, for the phonon populations at the large wave vector limits (terahertz phonons), the wavelength of the phonons are comparable to the interatomic spacing. In this case, the assumption of cotinuum dynamics is not applicable. We need to pay attention to details of individual atomic placements. By calculating for atomic positions between neighboring atoms and the interatomic forces, I formulate a dynamical matrix for the system of

our interest. The dynamical matrix correlates the wave vector of the phonons to their energy, generating a phonon dispersion relation. Elaborate details of the calculation is presented in Appendix B. Use of the dynamical matrix becomes especially important as we will be able to probe terahertz phonon in the future. Toward end of the chapter, I add a brief explanation on how we can extract high frequency phonon information from the diffusely scattered X-rays.

3.1 Simulation of Strain Generation and Propagation

3.1.1 Stress and Strain Relation in Solids

Impulsive generation of non-equilibrium phonons and carriers in a semiconductor produces a stressed near-surface region within optical penetration depth. The stress consequently generates strain causing a condensed matter system such as a single crystal to deform. We investigate phonons at low enough frequency, the solid behaves as an elastic continuum and the treatment of an anisotropic elastic medium is valid. At a given frequency and a direction, it is possible to have three sound waves. They are different to each other in their direction of polarization and velocities. For sound waves traveling in a high symmetry direction, for instance $[001]$ in GaAs, one of the longitudinally polarized along $[001]$ and the other two are transversely polarized in mutually perpendicular directions.

To illustrate the method of visualizing propagation of sound, we can imagine a longitudinal wave propagating along a particular direction. In an elastic crystalline solid, strain caused by a stress exerted on a solid is considered to be proportional to the stress and the displacements from equilibrium are very small. Consider a

lattice structure with cubic symmetry, disregarding the degeneracy. In this case, there are six independent stress components, $\sigma_{xx}, \sigma_{yy}, \sigma_{zz}, \sigma_{xy}, \sigma_{xz}$, and σ_{zy} where the subscripts denote directions that the stress is acting on. σ_{ii} represents strain acting on one direction where the cross terms such as σ_{ij} , where $i \neq j$, stands for shear. For a cubic unit cell crystal such as GaAs or InSb, unit cell can be defined by orthogonal sets of basis vectors \hat{x}, \hat{y} , and \hat{z} . And small deformations applied to the unit cell system can be expressed as follows [52].

$$\begin{aligned} x' &= (1 + \varepsilon_{xx})\hat{x} + \varepsilon_{xy}\hat{y} + \varepsilon_{xz}\hat{z} \\ y' &= \varepsilon_{yx}\hat{x} + (1 + \varepsilon_{yy})\hat{y} + \varepsilon_{yz}\hat{z} \\ z' &= \varepsilon_{zx}\hat{x} + \varepsilon_{zy}\hat{y} + (1 + \varepsilon_{zz})\hat{z} \end{aligned} \quad (3.1)$$

Where $\eta_{\alpha\beta}$ represents the applied deformation. They are dimensionless and have values much less than 1 if the strain is small. Here the strain can be defined as

$$\begin{aligned} \eta_{\alpha\alpha} &\cong \varepsilon_{\alpha\alpha} = \frac{\partial u_{\alpha}}{\partial \alpha} \\ \eta_{\alpha\beta} &\cong \varepsilon_{\alpha\beta} + \varepsilon_{\beta\alpha} = \frac{\partial u_{\alpha}}{\partial \beta} + \frac{\partial u_{\beta}}{\partial \alpha} \end{aligned}$$

Where α and β are the indices for direction unit vectors and u_{α} is the displacement along the direction denoted by the index. For simplicity higher orders of stress tensor terms are ignored and the relation between the strain components and the stress components can be formulated through elastic compliance vector.

For more specialized and general stress-strain relation, in an anisotropic linear elastic materials, we have $\eta_{ij} = S_{ijkl}\sigma_{kl} + \alpha_{ij}\Delta T$ where α_{ij} is a thermal expansion coefficient, S_{ijkl} is the elastic compliance tensor of which inverse is related to the elastic modulus or stiffness tensor, and ΔT is the temperature change in the material. Note that S_{ijkl} is the elastic compliance tensor of which inverse is related to the elastic

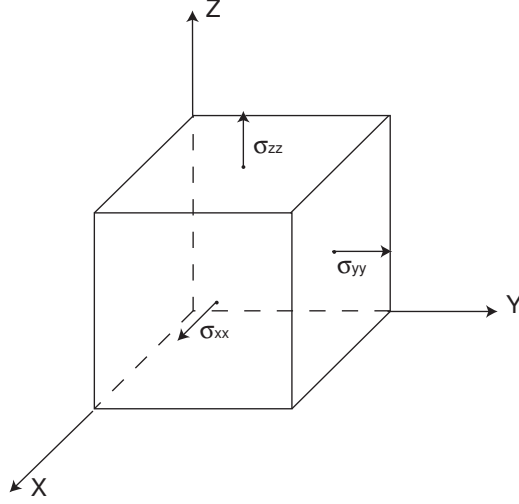


Figure 3.1: Schematics of 3 Dimensional Stresses in Cartesian coordinate

modulus or stiffness tensor, and ΔT is change in temperature on the material. Note that S_{ijkl} is a fourth order tensor and carries 81 possible components. Nevertheless it can be reduced down to 21 through the symmetry relation $S_{ijkl} = S_{klij} = S_{jikl} = S_{ijlk}$. This symmetric property of compliance tensors allow us to formulate the stress to strain relation in a more compact matrix form [52][53].

$$\begin{bmatrix} \eta_{xx} \\ \eta_{yy} \\ \eta_{zz} \\ \eta_{yz} \\ \eta_{zx} \\ \eta_{xy} \end{bmatrix} = \begin{bmatrix} S_{11} & S_{12} & S_{13} & S_{14} & S_{15} & S_{16} \\ S_{21} & S_{22} & S_{23} & S_{24} & S_{25} & S_{26} \\ S_{31} & S_{32} & S_{33} & S_{34} & S_{35} & S_{36} \\ S_{41} & S_{42} & S_{43} & S_{44} & S_{45} & S_{46} \\ S_{51} & S_{52} & S_{53} & S_{54} & S_{55} & S_{56} \\ S_{61} & S_{62} & S_{63} & S_{64} & S_{65} & S_{66} \end{bmatrix} \begin{bmatrix} \sigma_{xx} \\ \sigma_{yy} \\ \sigma_{zz} \\ \sigma_{yz} \\ \sigma_{zx} \\ \sigma_{xy} \end{bmatrix} + \Delta T \begin{bmatrix} \alpha_{11} \\ \alpha_{22} \\ \alpha_{33} \\ \alpha_{23} \\ \alpha_{13} \\ \alpha_{12} \end{bmatrix}$$

Where $S_{iii} = S_{ii}$ and $S_{iijj} = S_{ij}$.

Where $xx = 1, yy = 2, zz = 3, yz = 4, zx = 5, \text{ and } xy = 6$.

Later the computation becomes much simpler than the above because we assume uniaxial pressure wave and disregard presence of shear. In that case calculation is

possible with only S_{11}, S_{12} and S_{44} . It should be noted that linear part of these elastic equation does not account for dispersions.

3.1.2 Simulation of Laser Induced Strain Generation and Propagation

The most widely used model for strain generation and propagation in semiconductors is a thermoelastic model that was proposed by Thomsen et al. [6] approximately twenty years ago. The model assumes that the energy transfer from the photoexcited electrons to the lattice occurs through instantaneous thermal expansion while neglecting most of the carrier relaxation processes described in chapter 1. Optical radiation absorbed within the penetration depth increases the surface temperature thus exerting stress that causes a localized deformation. If the illuminated area is sufficiently large compared to the extent of the initial stress distribution along the surface normal, the stress near the center of the beam spot can be regarded uniaxial. In this approximation, the stress causes a displacement parallel to the surface and strain propagates throughout the crystal in form of a longitudinal acoustic wave which consists of broad spectrum of phonon modes (See Figure 3.2). Details of the model and associated assumptions are discussed in following paragraphs.

When you apply intense light with sufficiently short pulse duration (\sim sub-picoseconds) with photon energies close to or above the band gap of the semiconductor, you can generate a dense photoexcited electron and hole plasma near the surface. The process of excitation of the plasma is maintained throughout the duration of the light pulse and they remain in the conduction and valence band typically for tens of nanoseconds to a few microseconds. This excitation changes the equilibrium lattice

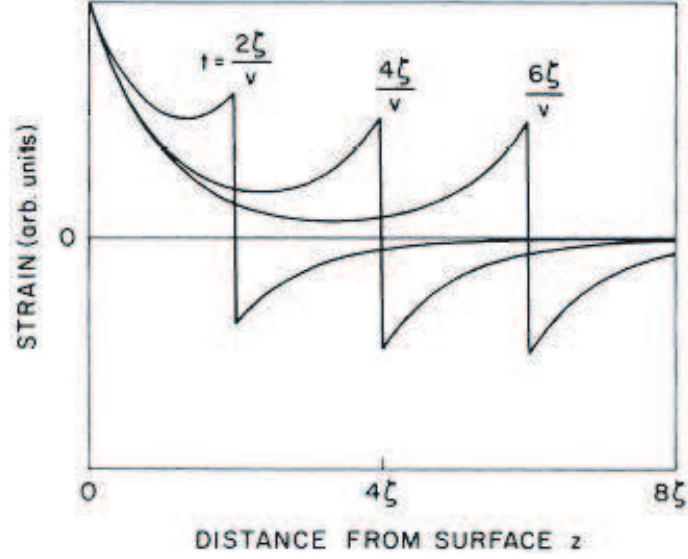


Figure 3.2: Calculated spatial dependence of the strain based on Thomsen's thermo-elastic model at different times following optical absorption [6].

spacing and introduces an electronic stress because the valence band electrons in general contributes to binding the lattice more effectively than the conduction electrons, and in result it basically changes energy band extrema. Such coupling between the excited carriers and lattice is governed by the deformation potential that binds the applied strain to changes in band. Following the initial excitation, the e-h pairs loose their energy through coupling with the lattice. During this process, the hot carriers impart most of their kinetic energy into the phonon bath system. Non-equilibrium incoherent phonons can be generated through this mechanism [54, 55].

In our numerical scheme, we consider a short laser pulse that deposits most of its energy into an isotropic substrate and generates a near instantaneous stress. We assume that the absorption depth μ is much smaller than the material thickness d , which is true for most of the experiment covered in my work. Also we assume that the linear dimension of the area A illuminated by the optical pulse with energy Q

is sufficiently larger than the absorption depth. The total energy deposited per unit volume at a distance z into the material can be written as

$$W(z) = (1 - R) \frac{Q}{A\mu} e^{-\frac{z}{\mu}}, \text{ where } R \text{ is the surface reflectivity.}$$

The corresponding heating of the medium gives a temperature rise that is

$$\Delta T(z) = \frac{W(z)}{C_v} \text{ where } C_v \text{ is the specific heat per unit volume.}$$

Assuming that resulting strain is going to be uniaxial and thus the stress only exerts on z-axis, only nonzero element in the strain tensor is η_{zz} .

Hence we have

$$\sigma_{zz} = \rho v^2 \eta_{zz} - 3B\alpha \Delta T$$

where B is the bulk modulus, ρ is material density and ν is the longitudinal speed of sound. Note that $\rho v^2 = \frac{3B(1-\nu)}{(1+\nu)}$, where ν is known as Poisson ratio.

We also have the wave equation $\rho \frac{\partial^2 \eta_{zz}}{\partial t^2} = \frac{\partial^2 \sigma_{zz}}{\partial z^2}$, which can be re-written as $\rho \frac{\partial^2 \eta_{zz}}{\partial t^2} = \frac{\partial^2 \sigma_{zz}}{\partial z^2}$ since $\eta_{zz} = \frac{\partial u_{zz}}{\partial z}$.

As a result, the wave-equation with differential expansion term as a driving force:

$$\frac{\partial^2 \eta_{zz}}{\partial t^2} - v^2 \frac{\partial^2 \eta_{zz}}{\partial z^2} = -v^2 \left(\frac{1+\nu}{1-\nu} \right) \alpha \frac{\partial^2 \Delta T}{\partial z^2}$$

If we assume that the strain is initially zero, that is $\eta(z, t < 0) = 0$ and that the stress at the surface is always zero, we have a solution that shows

$$\eta(0, t > 0) = \left(\frac{1+\nu}{1-\nu} \right) \alpha \Delta T(0, t > 0)$$

These boundary conditions ensure that there will be two acoustic waves that propagates in opposite directions in addition to a stationary strain. Thus the strain

$$\eta_{zz} = \eta_{stationary} + \eta_{+z} + \eta_{-z}$$

$$\eta_{zz}(z, t) = (1 - R) \frac{QB(1 + \nu)}{A\mu C(1 - \nu)} \left(e^{-\frac{z}{\mu}} \left(1 - \frac{1}{2} e^{\frac{-vt}{\mu}} \right) - \frac{1}{2} e^{-|z-vt|/\mu} \text{sgn}(z - vt) \right)$$

3.1.3 Effect of Plasma Diffusion and Recombination

When carrier diffusion process is faster than the associated attenuation, which is true for many semiconductor materials, the simple thermoelastic model, which is described in the previous section, becomes inadequate to describe the laser induced strain[3, 56, 4]. In this case, it is important to include contributions from generation, decay and heating of the plasma. First we make an assumption that e-h pairs are created instantly upon incident of the laser beam and that energy transfer from the plasma to the lattice occurs with a time constant less than 1 ps. In this case initial plasma density $n(z, t)$ is given by

$n(z, t) = \frac{n_0}{d} e^{-z/d}$ where n_0 is the number of photons per unit area absorbed at the surface and n_0 is the absorption depth d of the optical radiation. Subsequently the plasma diffuses and decays by the equation

$$\frac{dn(z, t)}{dt} = D_p \frac{d^2 n(z, t)}{dz^2} - An^3$$

Where D_p is the ambipolar plasma diffusion constant and A is the Auger decay parameter. Assuming that the thermal exchange between the plasma and the lattice occurs instantly, initial thermal distribution can be given as follows.

$$T(z, t = 0) = n(z, t = 0) \frac{(E_p - E_g)}{C_l}$$

Where E_p, E_g, C_l are photon energy of the pump laser beam, electronic energy

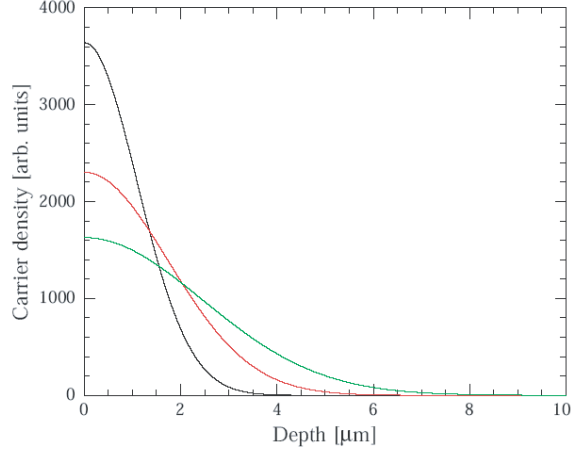


Figure 3.3: Temporal evolutions of photo-excited carriers with carrier and thermal diffusion processes taken into account.

bandgap, and lattice heat capacity per unit volume respectively. Subsequent evolution of the temperature is then governed by thermal diffusion and Auger heating

$$\frac{dT(z,t)}{dt} = D_t \frac{d^2 T(z,t)}{dz^2} + An^3 \frac{E_g}{C_l}$$

Changes in the local equilibrium lattice constant, strain at depth z and time t is calculated to be $\eta_e(z,t) = \alpha_t T(z,t) + \alpha_p n(z,t)$ where α_t is thermal expansivity and α_p is the deformation potential coupling term. The changes in the lattice temperature and plasma density generate two acoustic waves propagating in opposite directions. This occurs because the equilibrium lattice constant depends both on temperature and on the plasma density. For phonon modes that are associated with acoustic wave propagation, we will assume that all wavelengths are sufficiently long that there is no acoustic dispersion. The propagating waves can be given by

$$\begin{aligned} \eta_-(z,t) &= -\frac{1}{2} \int_0^t \frac{d\eta_e(z-vt',t-t')}{dt'} dt' \\ \eta_+(z,t) &= -\frac{1}{2} \int_0^t \frac{d\eta_e(z+vt',t-t')}{dt'} dt' \end{aligned}$$

And the strain is then

$$\eta_{total}(z, t) = \eta_e(z, t) + \eta_+(z, t) + \eta_-(z, t)$$

Numerical output from above equations is later incorporated into the dynamical X-ray diffraction and compared with experimental data where its validity is test with different input parameters.

3.1.4 Dynamical Matrix and Dispersion Relation

Most fundamental dynamics observed in a solids state physics touch upon the concept of lattice vibrations, and it is often used to explain sound and heat transport and various other phenomena occurring in solid materials. In modern lattice dynamics, solid crystalline objects are often viewed as arrays of atoms with finite masses that are capable of motion. Superposition of vibrations of atoms around their equilibrium sites due to the interactions with neighboring atoms or external forces provide very pronounced mechanism that are often described through following equations.

$$D(k) = \sum_R D(R) e^{-ikR} \quad (3.2)$$

$$n_j(q) = \frac{1}{e^{hw(q)/kT} - 1} \quad (3.3)$$

The dispersion relation can be directly derived from a dynamical matrix (Eq. 3.2), which is a the Fourier transform of sum of force constant matrices between interacting atoms, which is explained in later part of the section. From this expression, we deduce frequency of a particular phonon mode Ks from its wave vector. At room temperature, majority of phonons reside near the center of Brillouin zone, and the phonon density due to the thermal vibration can be described by Bose-Einstein

statistics (Equation 3.3): mean excitation number of the normal mode ks at temperature T . Such equilibrium phonon dynamics has been well understood up to this day.

However if an atomic vibration is artificially initiated at a particular point in a periodic medium in a such case of generation of laser induced phonons, the vibration will spread like a water wave throughout the rest of the crystal. In this case, dynamics of phonon becomes far more complex than it is due to thermal variations and classical approximation of phonon dynamics is no longer valid. Nevertheless interpretation of phonon dynamics based on dispersion relation should still be valid. In this section I would like to discuss how the basis of dispersion relation can be formulated.

Introductory solid state example of lattice dynamics is a linear chain of atoms that are connected by springs. In an equilibrium state, positions of atoms can be expressed as $z_n^0 = n \cdot a$ where n and a are a integer number and a lattice parameter. And the instantaneous positions of the atoms and associated displacements are related by $z_n = z_n^0 + u_n$. And the potential of the system can be given by

$$U = U^0 + \frac{1}{2}k(u_{n+1} - u_n)^2 + \frac{1}{2}k(u_n - u_{n-1})^2 + \dots$$

And the force on the atom is given by

$$F_n = -\frac{dU}{dx_n} = -2ku_n + k(u_{n+1} + u_{n-1})$$

In general the exerted force on atoms can be written in following form

$$F_n = -\sum_m \Phi(m, n)u_m$$

Where $\Phi(m, n)$ are force constants associated between m th and n th atoms.

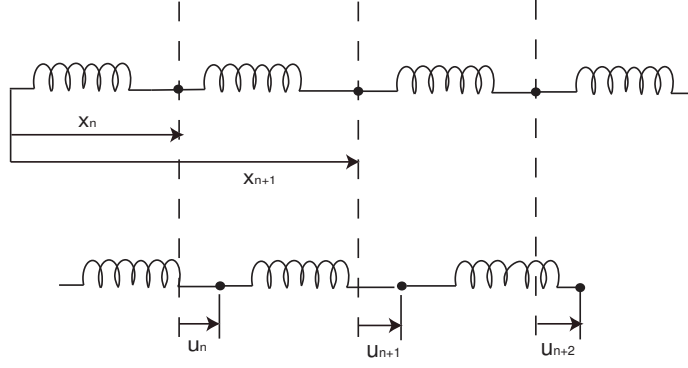


Figure 3.4: Arrays of atoms in a lattice structure can be viewed as a chain in which masses are connected by springs

We expand above relation to a three dimensional picture. In this case instantaneous position of atoms $r_n = r_n^0 + u_n$ and displacement r_n^0 are again related by where denotes lattice positions at equilibrium and the distance between atoms n and m is defined by $r_m^0 - r_n^0 = n_1a + n_2b + n_3c$ where a , b and c are basis vectors. For the simple cubic lattice, which we mostly work with, the basis vectors are orthogonal and have equal length. And thus the associated potential energy of the 3 dimensional lattices can be denoted by

$$U = U^0 + \sum_m \Phi_{i,j}(n, m) u_i(n) u_j(m) + \dots$$

Where $\Phi(m, n)$ s are called force constant matrix.

The components of force on atom n are given by $F_i(n) = -\frac{\partial}{\partial u_i(n)}$ and this leads to the equation of motion, similar formalism from 1-dimensional case.

$$F(r) = M \ddot{u}_i(r) = \sum_m \Phi_{i,j}(n, m) u_j(m)$$

Now assume a plane wave with polarization and wave vector k : $u(n) = u^0 e^{i(k \cdot r_n^0 - \omega t)}$.

e , then the equation of motion now becomes

$$M\omega^2 e_i = \sum_m \Phi_{i,j}(n, m) e^{i[k \cdot (r_m^0 - r_n^0)]} e_j$$

Here we define the dynamical matrix, which is a Fourier transform of the force constant matrix, which allows one to extract energy related information for any given wave vector, and it is given by relation $\|D_{i,j} - \omega^2 \delta_{ij}\| = 0$. Numerical values for elements of the force constants matrix for widely used semiconductor materials such GaAs or InSb are extensively studied and tabulated in many crystallographic literatures [57][58] and its analytical solutions are given in Appendix B.

3.2 Theory of X-ray Diffraction

In previous sections, I made discussions on the continuum treatment of phonons that is valid in short-wavelength regime and more generalized treatment using dynamical matrix. In this section, theoretical treatments of our probe, X-rays, will be elaborated. In the beginning, wave-like nature of X-rays will be explained and used to formulate X-ray diffraction and how it can be used to simulate time-resolved dynamics in a localized region inside solids. And then I would like to introduce particle-like nature of the probe by showing how lattice dynamics can be explored using momentum of X-rays and crystal-momentum.

3.2.1 Formulation of X-ray Diffraction

X-rays were discovered by W.C. Rontgen in 1895. Since then they have been used as an invaluable tool to probe the structures of matters ranging from periodic lattices such as crystals, protein crystals and up to more complex and celebrated samples

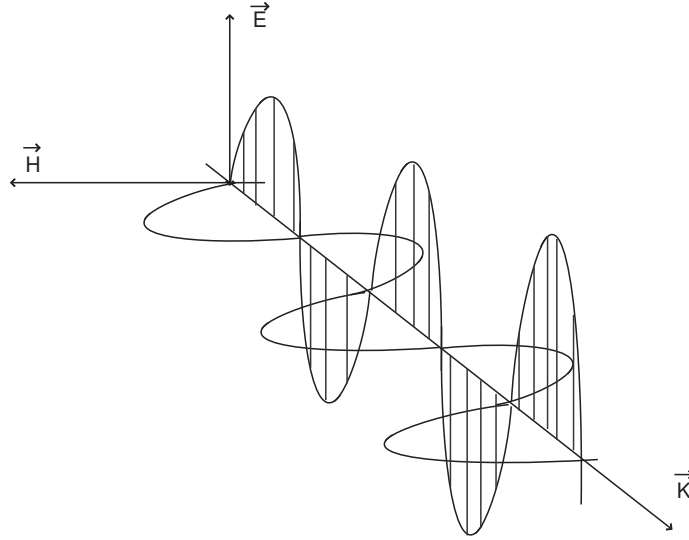


Figure 3.5: Propagation of Electromagnetic waves in free space

like DNA. The wavelength of X-rays is typically a few angstroms, comparable to the inter-atomic spacing in solids. This means that lattice structure of a crystal behaves as a diffraction grating for x-ray photons. Just as we would do in an optical diffraction experiments, by measuring the relative intensities from diffraction patterns from the crystal, we can obtain quantitative measurement of size of unit cells and structural arrangements, which beyond capabilities of optical probing methods.

In order to construct a complete picture of x-ray photons interacting with matters such as atoms in materials that we explore, we take a bottom to top approach. Concept of x-ray scattering from an electrons in materials can be used to formulate x-ray scattering from a single atom or arrays of atoms in a large scale. At a very fundamental level, the classical view of photon to electron scattering can be used. X-rays are electromagnetic waves that is often characterized by its wave length λ and propagating direction \hat{k} (See Fig. 3.1).

Now imagine an electromagnetic wave, $E(z, t) = E_0 \cdot e^{ikz} \cdot e^{-i\omega t} \hat{e}$ incident on a

single electron. Since they are transverse waves, we have $\hat{\varepsilon} \cdot \hat{k} = 0, \hat{k} \cdot \bar{E} = \hat{k} \cdot \bar{H} = 0$.

Resulting sinusoidal acceleration of the electron in the photon field can be given by

$$a(t) = \frac{F(t)}{m_e} = -\frac{e \cdot E(t)}{m_e}$$

Taking account for the speed of the EM wave, consider the effect of this field seen by an observer distance R away.

$$E_e(R, t) = \frac{e}{4\pi\varepsilon_0 c^2 R} a(t) = -r_0 E_{incident} \frac{e^{-ikR}}{R} \cdot \cos(\phi)$$

Where r_0 is the Thomson scattering length for a single electron defined by $r_0 = \frac{e^2}{4\pi\varepsilon_0 m_e c^2}$ and ϕ is the angle between location of the observer and the propagation direction.

Now expand this case to where one applies this formalism on to any array of atoms, the outgoing wave from N electrons will be the superposition of contributions from all the associated electrons (See Fig. 3.3). We need to account for a path length difference, and integrate over the whole electron population around atoms.

$$E_{atoms}(R, t) = \sum_{n=1}^N \int e^{-ir \cdot (k-k')} \cdot \rho_n(r) \cdot E_{electron}(R, t) d^3r \quad (3.4)$$

Once again expand the formalism to a perfect solid crystal case, and outgoing radiation becomes a superposition of intensities from arrays of atoms.

$$E_{crystal} = \sum_{m=1}^N E_m \cdot e^{ir_m \cdot (k-k')}$$

For a case of atoms with different types of basis (bm) generated with lattice R_l ,

$$E_{crystal} = \sum_{lattice} \sum_{basis} E_m \cdot e^{i(R_l + b_m) \cdot (k-k')} = \sum_{basis} E_m \cdot e^{ib_m \cdot (k-k')} \sum_{lattice} e^{iR_l \cdot (k-k')} = F \sum_{lattice} e^{iR_l \cdot q}$$

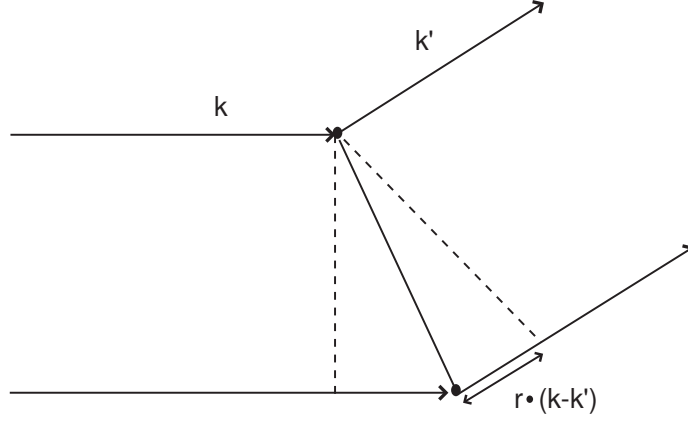


Figure 3.6: The path difference of scattered radiation between atoms at separation r .

where F is the structure factor, which contains intrinsic information about constitution and arrangement of atoms in a crystal.

Explicit derivation of the structure factor for GaAs zinc-blend structure is shown in Appendix A. From above expression, we expect high intensity at certain wave vector, which suffice following condition, $(k - k') \cdot R_l = 2\pi n$. This result is better known as Bragg law, which is widely used to determine crystal structure based on a condition for constructive interference of the diffracted x-rays scattered from a set of parallel lattice planes.

Although the Bragg law gives a simple and convenient method for calculating the separation in crystallographic planes, more elaborate analysis is necessary to obtain the intensity of scattering from a spatial distribution of electrons within each cell. Fourier analysis of equation 3.4 reveals that the Fourier transform for an infinite crystal case is non-zero only for a discrete set of values of $(k - k') = \delta K$, namely the reciprocal lattice vectors. The primitive reciprocal lattice vector for the one-dimensional crystal (for simplicity) is $b = \frac{2\pi \hat{x}}{a}$ where \hat{x} is the unit vector and the

general reciprocal vector is $G = hb$. The condition for the constructive interference is given by $(k - k') = \Delta k = G = \frac{2\pi}{d}$, where d is the lattice spacing between planes. The directions of the diffracted beams are given by the set of vectors k that satisfy this equation. However the formulism describes a classical x-ray scattering from a perfect crystal assuming no loss and motions in atoms, and it is insufficient to explain more elaborate dynamics within crystal structures.

3.2.2 Theory of Dynamical X-ray Diffraction

In order to analyze a localized incremental change inside a realistic periodic structure such as a propagating strain pulse, classical kinematics theory cannot be used for several reasons. For Bragg reflections with large structure factors, classical theory often overestimates the overall diffraction efficiency. In practical cases involving realistic crystals, attenuations of the incident beam due to the loss of intensity due to diffracted beam needs to be accounted for and its characteristic length scale is known as extinction length [59]. It is often necessary to characterize large nearly-perfect crystals and multilayered structures by diffraction technique. Kinematical modeling of the systems showed considerable discrepancies in predicting detailed structure near the Bragg peaks in multilayered samples because it does not account for interference effect between reflection amplitude contributions from each layers. It is also incapable of predicting the diffraction pattern that depends on geometries of incident beam to the sample. It often involves the use of dynamical theory of x-rays to simulate the diffraction profiles and intensities in the case mentioned above.

Most importantly to us, in order to study dynamics of localized non-equilibrium

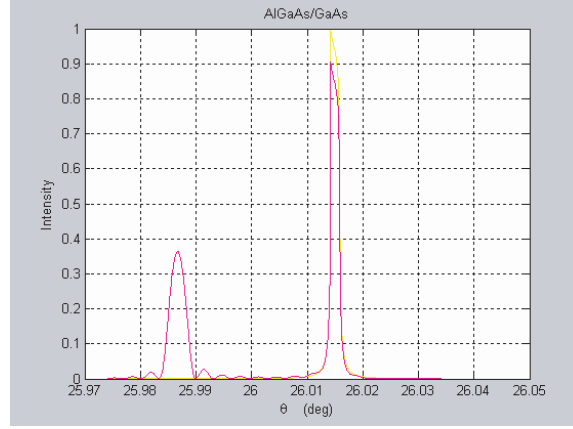


Figure 3.7: Propagation of Electromagnetic waves in free space

phonon in which strain field induced by laser beam extends far into the crystal, a quantitative interpretation of the diffraction pattern can only be obtained through use of dynamical theory of x-rays.

During last few decades, several developments of dynamical theory have been published [60][61]. Initial motivation of theory is to come up with a systematic formulation to calculate strain or composition depth profile and compare it with the experimental data. Among them, the best to fit the experimental rocking curve is to solve Takagi-Taupin equation. In the initial approach the theory treats sets of wave-propagations in a crystal as an eigenvalue problem and applies boundary conditions to obtain intensities of Bragg reflections.

At a fundamental level, a wave field in the crystal can be expressed by a Bloch function, $\psi(r) = \sum_h \Psi_h \exp(-2\pi i k_h \cdot r)$, where h is the reciprocal lattice vector and k_h are the wave vectors inside the medium which is constrained by conservation relation $k_h = k_0 + h$ where k_0 is the wave vector of the x-ray in vacuum. And ψ_h is a function of position, so that it can represent all possible diffracted waves in the

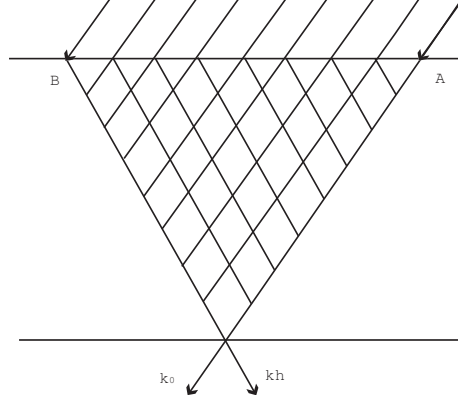


Figure 3.8: Propagation of Electromagnetic waves in free space

crystal.

The crystal potential, or dielectric function, $\chi(r) = \frac{V(r)}{E_e}$, in which $V(r)$ is the electrostatic potential in the crystal and E_e being the accelerating potential of an electron, can be expanded in a Fourier series such that, $\chi(r) = \frac{1}{v} \int_{\text{unit cell}} \chi(r) \exp(2\pi i h \cdot r) dr$, where v is the unit cell volume.

At this point the Bloch wave solution can be obtained through Schrodinger equation. By making an assumption that ψ_h and $\chi(r)$ are constant within a unit cell and that $\nabla^2 \psi_h(r)$ is small compared to $\psi_h(r)$, following sets of equations can be obtained.

$$\frac{\partial \psi_h(r)}{\partial s_h} = (2\pi i K \beta_h \psi_h(r)) - i\pi K \sum_{h' \neq h} \chi_{h-h'}(r) \psi_{h'}(r)$$

Where $\frac{\partial}{\partial s_h}$ refers to differentiation respect to the space coordinate parallel to k_h and parameter β_h is given by $\beta_h = \frac{(k_h^2 - k_0^2)}{2K^2}$, where k_h and k_0 are x-ray wave vectors inside crystal and K is the wave vector in vacuum.

Such assumption is justified because difference of wave-vectors of x-rays in a crystal and in vacuum is negligible. In a specialized case that $\chi(r)$ depends only on one coordinate, normal to the entrance surface and in the case of two strong waves, which is the most important in x-ray diffraction experiments, two possible solutions

to the wave question remains.

$$\begin{aligned}\frac{\partial \psi_0(r)}{\partial s_0} &= -i\pi K \chi_h^-(r) \psi_h(r) \\ \frac{\partial \psi_h(r)}{\partial s_h} &= -i\pi K \chi_h^-(r) \psi_h(r) + 2i\pi K \beta_h \psi_h(r)\end{aligned}$$

Where, χ_h and χ_h^- are the Fourier coefficient of the dielectric susceptibility. And finally the we impose a boundary condition at the entrance and exit surface. In a simplistic case of a single crystal, it can be given as (see Fig. 3.1),

$$\chi_0(r) = \chi_0^I(r) \exp(-2i\pi(K_0 - k_0) \cdot r)$$

$$\chi_h(r) = 0$$

However for more elaborate case of multilayer sample or to calculate for localize strain effect inside the crystal, which applies to works describe in this thesis, multiple boundary conditions are required, and thus boundary condition needs to be modified to,

$$\chi_0(r) = \chi_0^I(r) \exp(-2i\pi(K_0 - k_0) \cdot r)$$

$$\chi_h(r) = -i\pi K \chi_h^-(r) \psi_0(r) \exp(-2i\pi(K_0 - k_0) \cdot r) + 2i\pi K \beta_h \psi_h(r)$$

The solution to the Takagi-Taupin equation can be given by a ratio between diffracted displacement field and the incident displacement field as a function of depth into the crystal, z .

$$X(z) = \frac{\sqrt{|\gamma_H|} \psi_H(z)}{\sqrt{|\gamma_0|} \psi_0(z)}$$

Where γ_0 and γ_H are the direction cosines of the incident and diffracted waves respect to normal incidence.

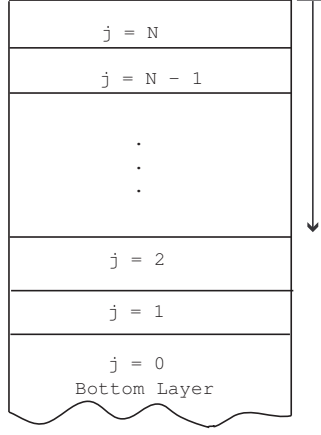


Figure 3.9: Solution to the Takagi-Taupin equation can be obtained by calculating solutions at each layer or mesh points

In Bragg case, an analytical solution can be given by

$$X(z) = \frac{S_j X(z_{j-1}) + i[B_j + C_j X(z_{j-1})] \tan[S_j A_j(z_j - z_{j-1})]}{S_j - i[C_j + B_j X(z_{j-1})] \tan[S_j A_j(z_j - z_{j-1})]}$$

$$A = \frac{\lambda r_e F'_H}{V \sqrt{|\gamma_0 \gamma_H|}}, B = -\frac{F_H}{F'_H}$$

$$C = Y + ig, S = \sqrt{C^2 - B^2}$$

$$Y = -[(1+b)F'_0 + (\frac{\pi V}{\lambda^2 r_e})b\alpha_H]/2 |F'_H| \sqrt{b}, g = -(1+b)F''_0/2F'_H \sqrt{b}$$

$$\alpha_H = -2(\theta - \theta_{Bragg}) \sin(2\theta_{Bragg}) - 2(k_\perp \varepsilon_\perp + k_\parallel \varepsilon_\parallel) \sin(2\theta_{Bragg}), b = \left| \frac{\gamma_0}{\gamma_H} \right|$$

k_\perp and k_\parallel are geometrical factors given by

$$k_\perp = \cos(\phi) \tan(\theta_{Bragg}) - \sin(\phi) \cos(\phi)$$

$$k_\parallel = \sin(\phi) \tan(\theta_{Bragg}) + \sin(\phi) \cos(\phi)$$

Where ϕ is the angle between reflecting planes and the sample surface.

$$\varepsilon_\perp = \frac{(a_\perp - a_{j+1})}{a_{j+1}}$$

$$\varepsilon_\parallel = \frac{(a_\parallel - a_{j+1})}{a_{j+1}}$$

a_\perp and a_\parallel are the in-plane and normal layer lattice constant while a_{j+1} is the lattice constant of subsequent layers. Where j is the layer number and Z_j is the depth at

the top surface of the layer from the crystal surface (see Fig. 3.3). The formula applies for polarization. For π state structure factor F_H needs to be replaced with $F_H \cdot \cos(2\theta_{Bragg})$. Solutions to these wave equations are later carried out by numerical integration using scheme suggested by Wei and with use of computers.

3.3 Probing Phonons Dispersion Relation with X-Rays

As X-rays incident on a crystal, by measuring the emerging angles or energies of scattered X-rays, we can obtain direct information about the phonon spectrum because X-rays scatter with emission/absorption of phonons. In general, the resolution of minute photon frequency shift would be difficult to measure with X-rays, but total scattered radiation of all frequencies as a function of scattered angle in the diffuse background can still be measured away from Bragg condition. Imagine a slight displacement of an atom in crystal structure from its equilibrium position due to thermal vibrations or external forces illuminated by monochromatic X-ray radiation. For outgoing radiation pattern, which is vastly complicated by interference from small distortions, we essentially need to calculate a time average diffraction pattern of a classical EM wave from excited crystal structure.

We first consider a monochromatic x-ray radiation of wave vector k_0 incident on a perfect crystal with stationary array of atoms. From section 2.1, we found out that outgoing wave at some wave vector k' can be expressed as $\psi = F \cdot \sum_{lattice} \exp(iR_l(k - k'))$. Let each atom n to be perturbed away from its equilibrium condition by displacement u_n . Consider a lattice with single atom in a basis, then $u_i = r_i - R_i$. Then we can write the resulting intensity as,

$I = \langle \psi \psi^* \rangle = |F|^2 \sum_{i,j} e^{iq \cdot (R_i - R_j)} \langle e^{iq \cdot (u_i - u_j)} \rangle$, where q would be the crystal momentum or momentum transfer to satisfy Bragg condition. Now realizing that $|u_i|$ are small values to approximate the time average, the expression can be re-written as,

$$I = |F|^2 \cdot \sum_{i,j} e^{iq \cdot (R_i - R_j)} e^{\frac{1}{2} \langle (q \cdot (u_i - u_j))^2 \rangle}$$

And then treating the atomics motion as a superposition of plane waves,

$u_i = \sum_{k,\lambda} C_{k,\lambda} \hat{\varepsilon}_{k,\lambda} e^{i(k \cdot R_i - \omega_{k,\lambda} t + \delta)}$, where $C_{k,\lambda}$ is the amplitude of the displacement, $\varepsilon_{k,\lambda}$ is the frequency and δ is the associated phase. Replacing the exponential term, $\frac{1}{2} \langle (q \cdot (u_i - u_j))^2 \rangle = 2M(q) - \frac{1}{2} \sum_{k,\lambda} \left\{ \langle C_{k,\lambda}^2 \rangle (q \cdot \varepsilon_{k,\lambda})^2 \cos(\hat{k} \cdot (R_i - R_j)) \right\}$, where $M(q)$ is directly related to Debye-Waller factor, $\frac{1}{2} \sum_{k,\lambda} \langle C_{k,\lambda}^2 \rangle (q \cdot \varepsilon_{k,\lambda})^2$. Then the equation for the total intensity can be expanded to,

$$I = F^2 e^{-2M(q)} \sum_{i,j} e^{iq \cdot (R_i - R_j)} \cdot e^{\frac{1}{2} \sum_{k,\lambda} \left\{ \langle C_{k,\lambda}^2 \rangle (q \cdot \varepsilon_{k,\lambda})^2 \cos(\hat{k} \cdot (R_i - R_j)) \right\}}$$

In above equation, $M(q)$ carries information about rms displacement of the atoms, and the factor gives the magnitude of the diffraction intensity remaining in the Bragg peaks after transfer of intensity to the thermal diffuse scattering by the thermal motions of atoms. In short, physical interpretation of the Debye-Waller factor is random motions of atoms about their equilibrium position due to thermal energy, which observable quantity in X-rays diffraction not in optical measurements.

Since we expect that amplitude of the displacement is going to be a small term, second exponential term can be expanded in a power series, and thus we finally

obtain,

$$I = F^2 e^{-2M(q)} \sum_{i,j} e^{iq \cdot (R_i - R_j)} + F^2 e^{-2M(q)} \sum_{i,j} e^{iq \cdot (R_i - R_j)} \cdot e^{\frac{1}{2} \sum_{k,\lambda} \left\{ \langle C_{k,\lambda}^2 \rangle (q \cdot \varepsilon_{k,\lambda})^2 \cos(\hat{k} \cdot (R_i - R_j)) \right\}} + \dots$$

In above expression we realize that the first term reflects the geometrical reflection where intensity is attenuated by Debye-Waller term. Most of the missing intensity can be retrieved away from the diffraction condition, the second term, which represents the diffuse scattering. Of course subsequent terms correspond to higher order diffuse scattering terms. Therefore, by scanning reciprocal space where Bragg condition is not met, given that there is inelastic scattering (phonon and x-ray interaction) you can make out changes in the intensity on the diffuse scattering term. And from this intensity fluctuation, you can deduce phonon population at different lattice sites and obtain their frequency information through dynamical matrix that is discussed in the previous section.

CHAPTER IV

Time Resolved X-Ray Diffraction

4.1 Generation and Propagation of Acoustic Pulse at a Buried Interface

4.1.1 Probing with X-rays

Thermal transport in nanoscale material is a fundamental problem in condensed matter physics and is of great importance for development of practical devices [62]. Of particular importance at small length scales is the interface between materials, phonons transfer heat between materials and their scattering is particularly sensitive to the details of the interface [63, 64]. Early studies of phonon propagation across a super-lattice used superconducting tunnel channels as a phonon source and detector [65]. Recently femtosecond laser have found use in nanoscale thermal transport measurement, including all optical measurements of thermal conductivity [66, 67] and thermal boundary resistance of solid-solid [68] and solid-liquid interfaces [69]. In these experiments the laser plays a dual role, both creating the phonons (coherent and incoherent) and detecting them indirectly through changes in the optical properties. In contrast X-ray techniques are able to yield quantitative information about the atomic positions. TRXD has proven a versatile probe to study bulk and surface

lattice dynamics on picosecond and faster time scales. Recent X-ray experiments have included measurements of strain generation following short pulse laser excitations in metals [70] and semiconductors [71][3, 4, 56], phonon damping in thin Ge films [72] and phonon folding in multiple quantum wells [73, 74].

In this chapter, novel experiments on the generation and transport properties of a coherent acoustic wave-packets in an AlGaAs/GaAs multilayer sample are presented. Above-band-gap excitation in semiconductors by ultrafast laser pulses leads to the generation of a near instantaneous stress due to the creation and relaxation of electron-hole plasma. The plasma is initially present only in a thin layer near the surface. As the plasma diffuses and recombines, thermalizing with the lattice, strain is produced in the form of thermal expansion and an elastic response consisting of two compressive pulses. In a simple thermoelastic model, the thermalization process is fast and the plasma diffusion is slow compared with the acoustic transit time across the optical penetration depth. The model predicts a symmetric bipolar uniaxial strain pulse that propagate into the bulk [6]. One of pulses immediately propagates into the bulk. The other propagates towards the free surface, becoming a tensile pulse following reflection. A similar effect occurs in metals; however, diffusion (thermal and carrier) can seldom be neglected. We expect that the above-band-gap excitation in the GaAs by the ultrafast laser leads to the generation of a near instantaneous stress due to the creation and relaxation of a dense electron-hole plasma. The plasma is initially present only in a thin layer where the photo-excited carriers are generated. As the plasma diffuses and recombines, thermalizing with the lattice,

strain is produced in the form of thermal expansion and an elastic response consisting of two counter propagating compressive pulses. The thermalization process is fast and the plasma diffusion is slow compared with the acoustic transit time across the optical penetration depth, such that a simple thermoelastic model describes the resultant strain. For bulk materials, this model predicts symmetric bipolar uniaxial strain pulses that propagate at the longitudinal speed of sound. One of the pulses immediately propagates into the bulk; the other propagates towards the free surface, becoming a tensile pulse following reflection.

One of the central goal to this thesis is to gain quantitative understanding about coherent displacement of lattice upon ultrafast optical excitation. Even in a single crystal, it is difficult to analyze strain propagation due to high density carrier diffusion that dominates the overall strain dynamics in bulk substrates at early times (within hundreds of picoseconds), which is later accompanied by thermal diffusion process. Therefore, it is necessary to spatially isolate the impulsively generated strain pulse from rest of the crystal dynamics. For this purpose, we have acquired a specially designed multilayer sample that would allows us to isolate the athermal strain pulse in the film layer from the substrate dynamics. By observing how much the lattice spacing changes in the epitaxial layer and then comparing to the case in the substrate simultaneously, we can study contributions from different laser induced dynamics effect the lattice structure. Furthermore, by varying the pump laser fluences, we examined the limits of the thermoelastic model.

4.1.2 Experimental Apparatus and Procedure

For this particular experiment, professor Rachel Goldman's group at the Material Science & Engineering department of the University of Michigan grew a sample consisting of a single 1.5 micrometer thick (001) surface oriented $\text{Al}_{0.3}\text{Ga}_{0.7}\text{As}$ layer on (001) bulk GaAs using molecular beam epitaxy. The AlGaAs film was capped it with a thin (5 nm) protective GaAs layer (See Figure 4.1) to prevent oxidiazing of the film. The particular alloy of AlGaAs was chosen to be transparent to the pump laser beam while having an excellent acoustic match with the substrate. The multilayer sample is placed at the center of the HUBER goniometer and oriented in the symmetric (004) Bragg geometry at room temperature for X-ray energy of 10 keV. From the difference in the Bragg angles, the mismatch in lattice spacing along growth direction is calculated to be 0.09%. The small X-ray modulation between the Bragg peaks are due to finite thickness effects in the film and interference between X-rays diffracted from the wings of the AlGaAs and GaAs rocking curve, which, as stated in chapter 2, can be predicted from dynamical X-ray theory. Although the lattice mismatch between two materials is small, two distinct Bragg peaks are resolved (See Figure 4.1).

The material composition ratio of 3 to 7 in the AlGaAs/GaAs heterostructure is chosen to form a specialized energy band structure in the multilayer sample. Ideally at a low enough temperature, all the electrons are confined to the valence band and the material is an insulator. However at room temperature, some electrons with sufficient energy could make transitions to the conduction band and become free

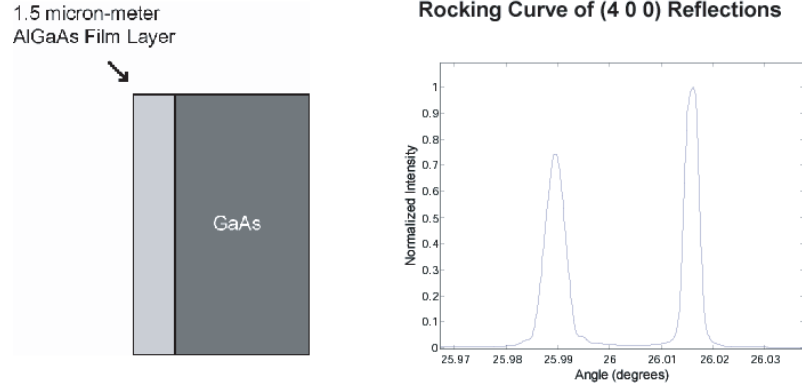


Figure 4.1: 1.5 μm AlGaAs/GaAs epitaxial sample grown on (001) GaAs substrate was used in this experiment. Figure on the right shows a static X-ray diffraction trace from the sample. Two individual (004) Bragg peaks are clearly resolved.

carriers. At equilibrium, the probability of electrons having enough energy to make the transition is given by Fermi distribution function. For near perfect crystals such as Si or GaAs, this Fermi energy level is approximately at the center of the energy gap. A short laser pulse with energy above the bandgap excites electrons from the valence band to the conduction band in the substrate. The sudden presence of the free carrier plasma generates impulsive strains, which propagates throughout the bulk medium.

In the experiment, laser pulses are incident on the air-side of the AlGaAs layer at a 1 KHz repetition rate. The laser photon energy, 1.55 eV, is significantly less than the band gap of this particular AlGaAs alloy, 1.79 eV, such that the film is effectively transparent to the laser (See Figure 4.2). The photons are absorbed in the GaAs substrate approximately within $1\mu\text{m}$. the conduction band of the AlGaAs is also sufficiently higher in energy than that of the GaAs such that the hot photoexcited carriers are confined to the GaAs. On a longer time scale, thermal transport across the boundary will heat the AlGaAs as the GaAs cools down. Since the X-ray Bragg

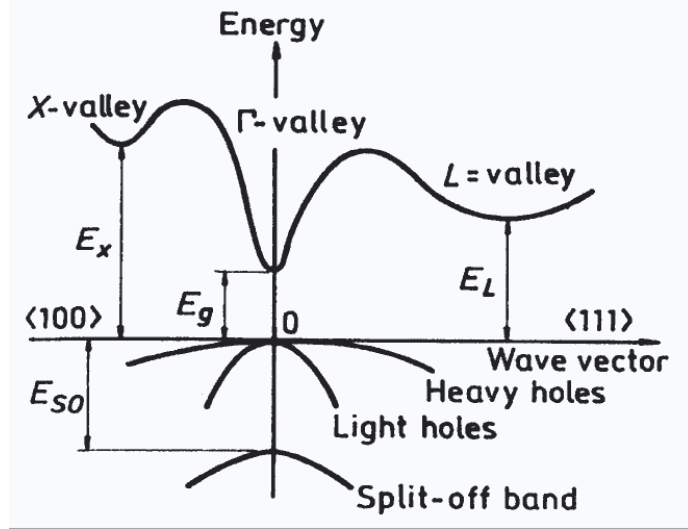


Figure 4.2: Energy band diagram of GaAs and AlGaAs. Band diagrams themselves do not look much different for those two alloys. Nevertheless their electronic structures are quite distinctive. For GaAs at room temperature $E_g = 1.42$ eV, $E_L = 1.71$ eV, $E_X = 1.90$ eV. For AlGaAs $E_g = 1.80$ eV, $E_L = 1.92$ eV, $E_X = 1.95$ eV.

peaks from the film and the substrate can be separately resolved, propagation of the laser-generated strain pulse and the temperature can be independently measured in the substrate and film.

4.1.3 Observation of Unipolar Strain Pulse

In our experiment, propagation of the strain pulse is modified by the existence of the AlGaAs film which separates the free surface from the region of photoexcitation. Since the frequency of the phonons associated with the strain is low compared to frequency of the X-ray probe, time-resolved diffraction can be considered in the quasi-elastic regime [75]. Figure 4.3 (a) shows a time scan of the diffraction at an angle of 27.546° on the high angle side of AlGaAs Bragg peak. The initial increase in the diffraction intensity corresponds to shifting of the Bragg peak to a greater angle, and thus a decrease in lattice spacing due to the compressive pulse being

launched from the GaAs substrate. Approximately 300 ps later, the leading edge of the strain pulse in the film arrives at the solid to air interface, and it reflects back toward the substrate side. During this process, a π phase shift is introduced in the strain pulse due to the effectively infinite acoustic mismatch between air and AlGaAs layer, and it gives rise to a tensile reflected strain pulse. As a result, the compression pulse becomes an expansion pulse; the lattice spacing of the AlGaAs layer increases and the Bragg peak shifts to smaller angles. This interpretation is supported by the subsequent decrease in the x-ray intensity on the high angle side of the Bragg peak as seen in Figure 4.3 (a). We can confirm this interpretation from the opposite behavior seen in the time-resolved diffraction efficiency measured at an angle 27.5415° on the low angle side of the unperturbed AlGaAs Bragg peak (See Figure 4.3 (b)). As the unipolar strain pulse is transmitted back into the GaAs substrate, the Bragg peak from AlGaAs returns to its initial value, indicating that no significant thermal expansion due to heat transfer across the interface has occurred. Within the limits of our detection, we see no evidence of a partial reflection from the interface.

The acoustic propagation time across the film is measured to be about 300 ps and is consistent with propagation of the strain pulse at the longitudinal speed of sound (4955 m/s) and thickness of $1.5\ \mu\text{m}$ AlGaAs layer. In the present case, determination of the film thickness by the propagation time is limited by the temporal resolution, and to a lesser extent on the details of the strain profile. We note that the width of the pulse can be determined from the time delay between the peak and the zero crossing

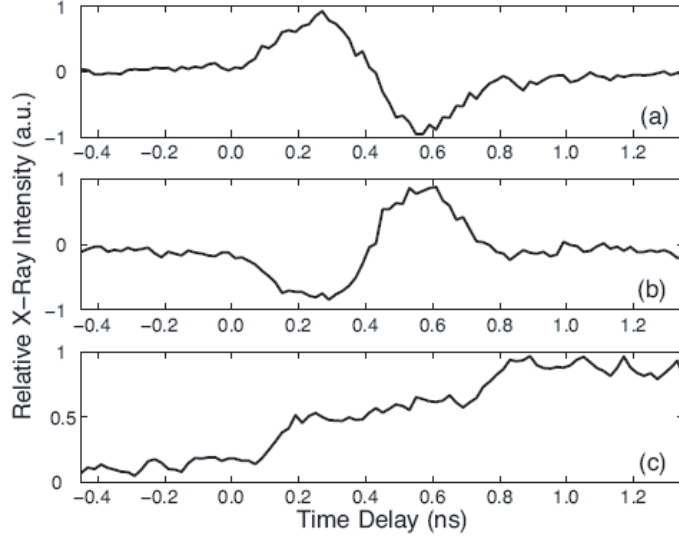


Figure 4.3: Intensity of the X-ray diffraction (measured relative to before excitation and normalized to the maximum) following femtosecond laser excitation above the gap in the GaAs substrate. Three different angles near the (004) Bragg peaks are shown: (a) 27.546° , on the high angle side of the AlGaAs peak; (b) 27.5415° on the low angle side of the AlGaAs peak; and (c) 27.5690° on the low angle side of the GaAs peak.

in the relative diffraction efficiency. At this precise instance, the integrated strain in the film is zero (equal amounts of compression and expansion). We estimate the pulse width of the strain to be $0.75 \mu\text{m}$ or $1.1 \mu\text{m}$ $1/e$ length assuming an exponential profile.

As the initial compressive strain pulses propagate away from the heated photo-excited region of the substrate layer, it leaves behind a region of thermal expansion, as can be seen from Figure 4.3 (c). The X-ray diffraction efficiency at 27.569° , on the low angle side of the unperturbed GaAs Bragg peak, increases with time as the strain pulse propagates out of the region of laser excitation. After approximately 600 ps, the component of the strain pulse that was launched into the AlGaAs layer returns to the substrate as an expansive pulse. This results in a further increase in

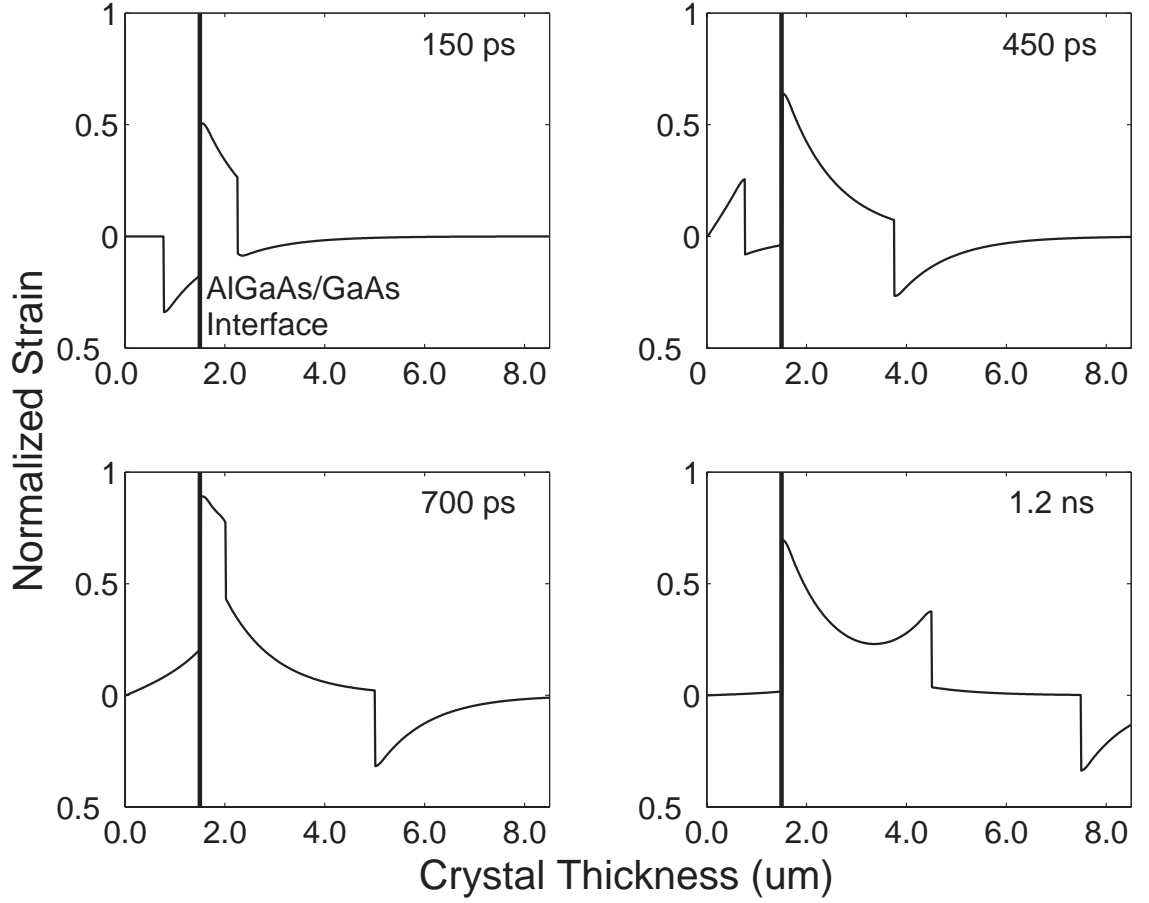


Figure 4.4: Simulation of the strain as a function of depth at four different time-delays following laser-excitation where the energy is deposited in a thin region of the GaAs substrate. A simple thermoelastic model is used in which the strain is due to differential thermal expansion and diffusion is slow. An elastic response is generated which travels at the longitudinal speed of sound. The transmission coefficient for the pulse at the heterostructure interface is unity and the reflection coefficient at the free surface is -1. Notice that a unipolar compression pulse propagates through the AlGaAs film, reflects off the free surface becoming a tensile pulse, and later transmits into the GaAs substrate.

the local lattice spacing, as can be seen by the additional increase in X-ray diffraction (the amplitudes of thermal expansion and strain pulses add). In fact, the change in diffraction efficiency nearly doubles indicating that the non-acoustic component to the strain has not significantly evolved on the \sim ns time-scale (See Figure 4.4). Not shown in the figure, the diffraction efficiency gradually decreases as the tensile strain travels deep into the bulk out of the X-ray probed region leaving the thermally expanded region behind to decay on the longer time-scale of diffusion and carrier relaxation.

4.1.4 Comparison with Simulation

In our simulation, changes in the atomic lattice spacing are obtained by calculating the total strain from bulk material. In optically opaque materials such as GaAs, the rapid changes in the localized excited region of the crystal cause the lattice to respond elastically. Thermoelastic model presents an analytic solution that describes the generation and propagation of laser induced strain as it was discussed in the chapter 3. Recall that for more realistic simulation, carrier and thermal diffusion have been included. And also because we are dealing with multilayer structure, a modified boundary condition is necessary to account for the lattice dynamics at the material interface.

In general, the calculation of transmission probability between two solids is not a simple problem. In our AlGaAs/GaAs sample, due to significant difference in the band gap structure, excited carriers do not transmit through the solid to solid interface. On the other hand, the propagating strain term, which was given as

$\eta_+(z, t)$ in chapter 2, may transmit through the interface due to closely matched lattice parameter. Under the assumption that phonon wavelength are sufficiently long such that contribution from acoustic dispersion is negligible, the solid-solid boundary condition follows continuum acoustics and scattering at the interface. The transmission probability can be calculated for any incident angle and mode. The simplest picture derivable from the acoustic mismatch model is that each material can be ascribed an acoustic impedance defined by $Z_i = \rho_i v_i$. The transmission probabilities are

$$Z_{GaAs \rightarrow AlGaAs} = \frac{4Z_{AlGaAs}Z_{GaAs}}{(Z_{AlGaAs} + Z_{GaAs})^2}$$

and

$$Z_{AlGaAs \rightarrow GaAs} = 1 - Z_{GaAs \rightarrow AlGaAs}.$$

The transmission across the solid-solid interface is calculated in the acoustic mismatch limit to be $t = 0.995$, so that in this limit reflections are expected to be negligible. Since the GaAs protective layer is thin compared to the phonon wavelength, the free surface of the film is taken as AlGaAs-vacuum interface, which results in a near perfect reflection of the compressive strain accompanied by a phase shift of 180 degrees.

Figure 4.5 shows data and simulation of a time and angle scan about the (004) AlGaAs peak. The glitches in the data at approximately 0.2 and 0.6 nanoseconds are due to the periodic topping off of the electron bunch charge in the storage ring and this a rise in average X-ray flux. From the shift in the Bragg peak, we estimate

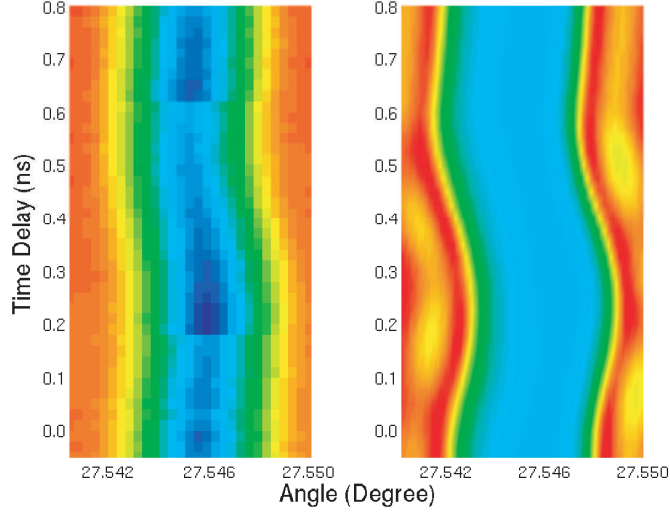


Figure 4.5: Time and angle resolved X-ray diffraction from AlGaAs film showing the propagation of a short acoustic pulse that was generated in the GaAs substrate. Experimental data are on the left and a simulation in which strain is incorporated into dynamical diffraction theory is on the right.

the maximum strain in the AlGaAs film to be 2×10^{-5} . The data is modeled using dynamical theory of X-ray diffraction modified to incorporate strain. The effect of the strain to the lattice parameter was accounted for by adjusting the angular deviation parameter [76, 77].

$$\alpha_H = -2 \cdot (\Delta\theta_{Bragg} - \eta_{total} \cdot \tan\theta_{Bragg}) \cdot \sin(2\theta_{Bragg})$$

The simulation using the strain profiles shown in Figure 4.5 reproduces the behavior seen in the data indicating that strain is well described by the generation of an instantaneous stress in the substrate and a very small acoustic mismatch at the heterostructure interface.

4.2 Measurements of Thermal Expansion versus Deformation Potential

In this section, origins of impulsively generated strain pulse will be discussed. Using TRXD measurements and results from simulation, we made a quantitative comparison of strain contributions from electronic and thermal stress in semiconductors upon ultrafast laser excitation. In a direct semiconductor such as GaAs, the process of the photo-excitation of electrons persists throughout the duration of the light pulse given that the electron states near the top of valence band are available. The spatial profile of the acoustic strain pulse is strongly influenced by electron relaxation routes. Thomsen et al [6] note that impulsive strain dynamics can be described by a thermoelastic model under the assumption that the energy transfer from the electron to lattice occurs via instantaneous lattice heating. It has been found that contributions from deformation potential certainly cannot always be neglected [78]. We present a novel method to determine which of the two is the dominant mechanism responsible for the generation of the strain pulse.

4.2.1 Experimental Layout

In our previous work, we have demonstrated a near perfect transmission of coherent acoustic wave packets at a buried interface of (001) surface oriented $\text{Al}_{0.3}\text{Ga}_{0.7}\text{As}/\text{GaAs}$ heterostructure. Due to the selective properties of sample composition ratio, only the strain component exerted by the acoustic wave was allowed to enter the film layer until both the epitaxial layer and the substrate come to a thermal equilibrium. However in order to obtain a numerical value for the strain amplitude, we need more

than an observation of the relative changes in X-ray diffraction efficiency on either side of rocking curve. It is necessary to know how much the Bragg peak shifts due to propagating strain pulse.

The experimental set up was similar to our previous experiments with an exception of a couple modifications. Instead of positioning the detector on one side of rocking curve, we constantly moved the point of detection to obtain the overall shape of the rocking curve. This way we can measure how the Bragg peak shifts and calculate changes to the lattice spacing. Furthermore rather than taking data with a gated integrator with APD in a linear proportion mode, a single photon detection scheme is employed. Although it takes a longer time to collect the data, single photon counting is much less susceptible to systematic noise than the gated integrator or dark current from APD in proportion mode. In our new data acquisition scheme we set three TTL gates with fixed time delays ($1/P_0$ apart) that are synchronized with incoming laser and X-ray pulses (See Figure 4.6). The first gate is put prior to the laser incident to the X-ray pulse to monitor diffracted X-ray counts before the laser excitation. The second gate is placed such that it is coincident with the arrival of laser pulse to the GaAs sample. An additional gate was placed after the second one to observe a long term thermal relaxation process in the crystal. Since we are always looking at a same electron bunch, any variation in individual bunch charge caused such as top-up is normalized out of the data sets.

Detector deadtime correction is necessary to increase the accuracy of our measurement. The X-Ray count rate can vary over many orders of magnitude while

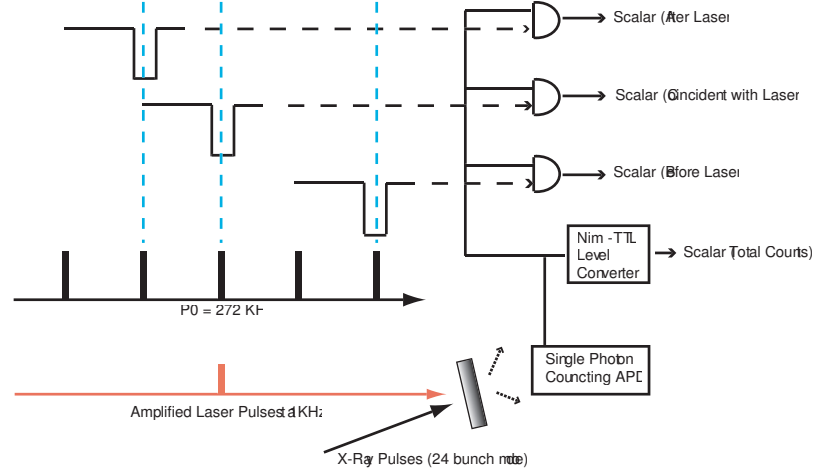


Figure 4.6: Data acquisition layout of time resolved X-ray counting scheme. APS counts are collected before, during, and after incident of the laser pulse to the GaAs crystal. Total counts are also being collected to give us a normalization factor.

scanning from base of the rocking curve to its peak. It is possible to collect multi-photon events recorded into our data set. The saturation broadens the apparent width of the Bragg peak and, as a result, reduces the sensitivity of the detection scheme. For dead time losses using a short pulsed source, we employ post acquisition analysis (See Figure 4.7). Since there should be at most a single X-ray photon count per pulse, the probability of an observed count per source pulse is given by m/f where m is the observed counting rate and f is the source pulse frequency, which is given by the repetition rate of our regenerative amplifier. The average number of true events per source pulse is by definition equal to n/f where n is true counting rate.

By applying the Poisson distribution $P(x) = \frac{(\bar{x})^x e^{-\bar{x}}}{x!}$ to predict the probability that at least one true event took place can be expressed as $P(> 0) = 1 - P(0) = 1 - e^{-\bar{x}} = 1 - e^{-\frac{n}{f}}$. Since the detector is on at start of each pulse, a count will be recorded if at least one true event occurs during the pulse. Only one such count can

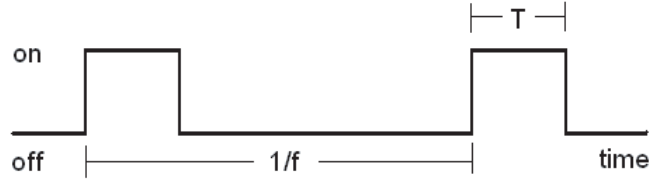


Figure 4.7: Pulsed radiation source, which has time-dependent intensity behavior, may require dead time loss correction

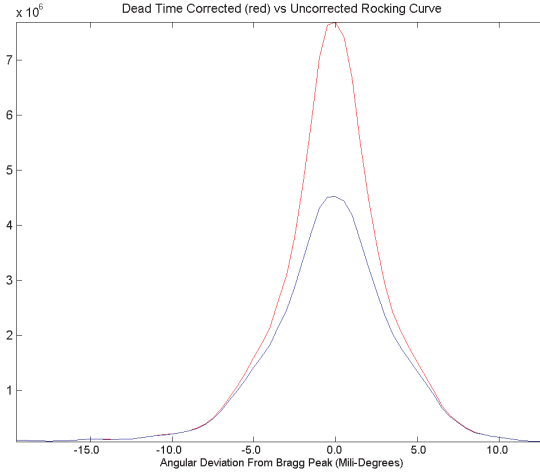


Figure 4.8: Rocking Curve about (004) reflection. Plot shows the comparison between data set with and without dead time correction.

be recorded, so the above expression is also the probability of recording a count per source pulse. By equating those two expressions, we have $\frac{m}{f} = 1 - e^{-n/f}$. Under these conditions, the maximum allowable counting rate should be just the pulse repetition rate of the laser. Solving above equation in terms of n , we drive $n = f \ln(\frac{f}{f-m})$, which is valid under assumption that $T < \tau < (\frac{1}{f} - T)$. Expanding the logarithmic term for $m \ll f$, we finally arrive to $n \cong \frac{m}{1-m/2f}$. Through this dead time correction the FWHM of the rocking curve gets reduced to 70 percent of the uncorrected one (See Figure 4.8).

4.2.2 Origin of Impulsive Strain Generation in GaAs

Measurement of Impulsively Generated Strain

We can quantitatively measure the amplitude of strains using time resolved X-ray diffraction. However, it is still difficult to determine the amplitude of the impulsively generated strain in a single crystal because strain contributions from thermal and carrier are superimposed on top of the propagating strain. Using the multilayer sample with very closely matched lattice parameter and considerably different electronic structure such as AlGaAs/GaAs, we can isolate the impulsive strain in the film layer. And thus, by measuring shifts of the Bragg peak in the film layer, we can measure the strain amplitude.

In a single crystal material, it is difficult to determine the amplitude of initial strain pulse alone because complex and fast scale dynamics of carrier diffusion distorts the strain profile that can be obtained from Bragg peak shift. Nevertheless by measuring Bragg peak shift in the film layer, we can easily measure this quantity. With the laser fluence absorbed by the AlGaAs/GaAs sample at $0.057 \frac{mJ}{cm^2}$, the maximum shift in Bragg peak approximately 0.19 mili-degree (See Figure 4.9), which corresponds to amplitude of the propagating strain is measured. At an equilibrium d-spacing of GaAs crystal is 5.65325 \AA . Using Bragg's law we can calculate new d-spacing from angle shift and thus the amplitude of the strain, which is 1.36×10^{-4} .

Relative Strength Measurement: Thermal Expansion VS Deformation Potential

In this section, we make a rough calculation to figure out the origin of the impulsive strain propagation in GaAs. First we assum that the strain is generated from

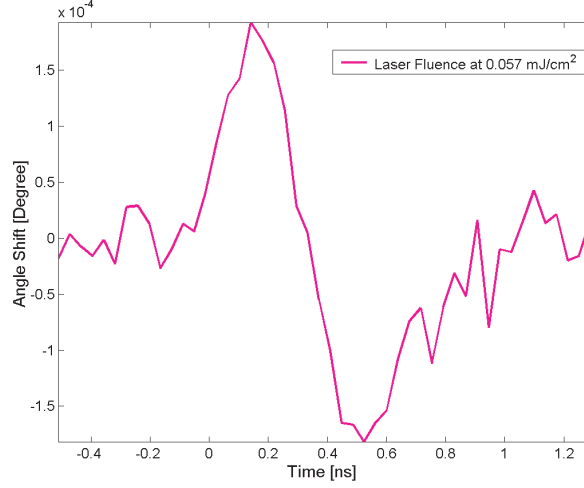


Figure 4.9: Propagation of a strain pulse in AlGaAs epitaxial film layer. Peak of Bragg peak shift accordance with lattice spacing changes.

thermal expansion upon laser excitation. Relevant parameters for the calculation is given in Appendix C. In theory the strain due to thermal expansion can be given as

$$\eta_T = \frac{a}{\Delta a} = \alpha_T \Delta T = \alpha_T \frac{\partial T}{\partial F} F$$

Where F is the absorbed fluence.

$$\frac{\partial T}{\partial F} = \frac{\hbar\omega - E_g}{\mu C_l \hbar\omega}$$

Assuming a linear inter-band absorption, for photon energy 1.55eV, we have

$$\frac{\partial T}{\partial F} = \frac{0.13eV}{(10^{-4}cm)(330\frac{mJ}{g})(5.32\frac{g}{cm^2})(1.55eV)} \cong 0.48Kcm^2/mJ$$

And therefore, thermal strain is

$$\eta_T = F \cdot (2.75 \times 10^{-6} \frac{cm^2}{mJ})$$

It is very evident that, for the laser fluence $0.057 \frac{mJ}{cm^2}$, a typical thermo-elastic model vastly underestimate the amplitude of the strain.

In the second calculation, we assume that the strain is generated solely due to volume deformation potential scattering. For the expected lattice strain due to electronic stress, we take an alternate approach. At this fluence significant number of photoexcited carriers will be promoted to the conduction band and cause lattice pressure, which is

$$P_{electron} = -\frac{\partial F}{\partial V} = -N \frac{\partial E_g}{\partial V}$$

Electronic pressure should balance the lattice pressure that is

$$P_{lattice} = -B \frac{\Delta V}{V}$$

Where the Bulk modulus is defined by $B = -V \frac{\partial P}{\partial V}$.

Therefore, the volume deformation by the electronic pressure can be expressed as

$$\frac{\Delta V}{V} = -\frac{N}{B} \frac{\partial E_g}{\partial V} = -\frac{n}{B} V \frac{\partial E_g}{\partial V} = n \frac{\partial E_g}{\partial V}$$

Where n is now the carrier density. Assuming that the strain is isotropic, we may safely state $\frac{\Delta V}{V} = 3 \frac{\Delta a}{a}$. This assumption is valid for $\Delta a \ll a$. Imagine small strain exerted on one of the directions of the crystal, then we expect small such that overall lattice constant now becomes: . Since $V = a^3 = a_0^3(1 + \Delta a/a)^3$, we can Taylor expand it out to

$$V = V_0 + \frac{\Delta V}{V} = a_0 + 3 \frac{\Delta a}{a_0}$$

$$\frac{\Delta a}{a} \cong \frac{n}{3} \frac{\partial E_g}{\partial P} = \alpha_p = \alpha_p \frac{\partial n}{\partial F} F$$

where $\frac{\partial n}{\partial F} = \frac{1}{\hbar \varepsilon \mu}$ Therefore strain contribution from deformational potential is

$$\eta_{pressure} = \frac{1}{3(1.55eV)(10^{-4}cm)} \frac{(0.115 \frac{eV}{GPa})}{10^6 mJ/cm^3/GPa} F = 2.47 \times 10^{-4} \frac{cm^2}{mJ} \cdot F$$

This gives us a strain value of 1.407×10^{-5} for the laser fluence at $0.057 \frac{mJ}{cm^2}$.

The calculated value for the deformation potential matches the experimental value, 1.36×10^{-4} within $3 \sim 4\%$ precision. This remarkably closely matched value leads us to see that impulsively generated acoustic pulse is indeed caused by the coupling between excited carriers and strain rather than thermalization from phonons. The TRXD experiment of the heterostructure at relatively low laser fluence, experimental data are in good agreement with a strain profile that is produced predominantly by impulsive stress as predicted by the numerical simulation (See Figure 4.9). Nevertheless it has been later found that our numerical scheme thus our intuitive understanding in strain generation and propagation falls short does not extend to the case under high laser fluence.

4.3 Laser Fluence Dependent Excitation Dynamics

In this chapter, our original theoretical conjectures and assumptions of strain generation and propagation are put into test at varying laser fluence. We discuss about discrepancies between the prediction from the numerical model and data. Accordingly, appropriate modifications will be incorporated into the existing model to simulate the strain generation and propagation.

4.3.1 Effect of Free Carrier Absorption

Optically excited free carriers eventually relax down to valence band while imparting most of their kinetic energy to the lattice through various processes. Among the mechanism shown in Figure 4.10, the optical absorption behavior is heavily influenced by free carrier absorption (FCA) under heavy excitation level. Typically the recombination through traps does not affect the absorption behavior because the traps already fill at much lower optical intensity level. Band to band luminescence also becomes insignificant at high laser intensities. Auger recombination does dominate at high carrier density but it alone does not necessarily affect the strain generation behavior of the crystal such as GaAs. Nevertheless excitation by high power femtosecond lasers leads to the saturation in carrier plasma density due to finite number of electrons that can be excited to the conduction band within the time window of tens of femtoseconds. Under such condition, the probability of the free carriers being excited by the incident photons increases drastically. As a result optical absorption in the crystal is no longer governed solely by the linear absorption coefficient [7]. In the experiments covered in previous chapters, interband excitation process is governed by the intensity independent absorption coefficient for photons. At high enough excitation it has been previously shown that the absorption is not linear and an optical limiting of the transmission of the light into the material occurs [79, 80, 81]. The nonlinearity of the absorption is attributed to FCA.

Manipulation of the intensity of infrared radiation transmitted through semiconductors by varying the concentration of free carriers has been extensively studied

since 1950s when FCA was demonstrated as a means of optical limiting in semiconductors [80, 81]. For example, passive nonlinear optical power limiter has extensive potential use as an effective devices for protecting sensitive optical components from high power lasers and optical transient. Ideally these devices should have a high transmission for relatively weak input radiation but effectively block intense signals that may damage the critical device by utilizing intrinsic nonlinearities in the materials.

The fact that free carriers can absorb electromagnetic radiation has been known for a long time. In 1880s, Lorentz qualitatively [82] demonstrated a theory of optical properties of insulators, where he assumed that insulating materials contain electrons that are bound to equilibrium positions by harmonic forces. The theory was later extended by Drude et al [83], to the case of metals containing free electrons. The theory of FCA was eventually applied to the case of semiconductor materials to obtain absorption coefficient for wavelength longer than the fundamental absorption edge. It had been already expected that the dynamics of photon absorption would be heavily influenced by presence of free charge carriers. Classical and quantum mechanical investigation also have supported the qualitative aspects of the theory [84].

4.3.2 Observation of Free Carrier Absorption

In our subsequent experiment, by measuring how much the lattice spacing changes at varying laser fluences, we observe how the carrier density changes under different excitation levels. Figure 4.11 shows shifts of the Bragg peak in AlGaAs due strain

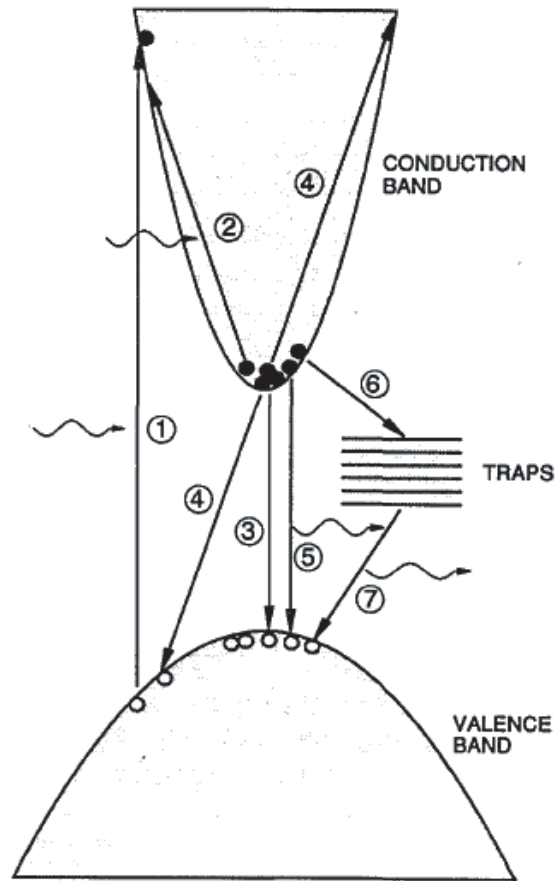


Figure 4.10: Simplified version of band gap of direct semiconductor [7]. Figure shows various energy relaxation routes of photo-excited carriers. (1) carriers are initially excited optically from valence to conduction band. (2) FCA process where excited electrons are once again excited by incident photons and promoted deep into the conduction band. (3) Non-radiative recombination. (4) Auger recombination process where excess energy of an electron is transfer to another carrier as it recombines with holes. (5) Luminescent transitions (6) trapping of free carriers and (7) recombination.

pulse propagation at 5 different laser fluence levels. The peak amplitude of the strain pulse starts to saturate beyond the laser fluence of $0.111 \frac{mJ}{cm^2}$. This behavior indicates that the carrier density indeed saturates under heavy excitation. Therefore, it is necessary to include effect of FCA to correctly reproduce the experimental result in the simulation.

4.3.3 Incorporation of FCA in the Numerical Simulation

Free Carrier Cross Section Absorption Coefficient

The continuity equation for the carrier concentration in a plane perpendicular to the laser beam has been given as

$$\frac{\partial n(z, t)}{\partial t} = -\alpha \cdot I(z, t) \quad (4.1)$$

In above equation, the intensity of the laser pulse as a function of space and time is given by $I(z, t)$ in units of number of photons per unit area and time and α is the linear absorption coefficient. The absorption by free electrons and holes is proportional to the free carrier pair concentration. Under low to moderate excitation levels, equation (4.1) closely follows an experimental result. Nevertheless at high excitation ($10^{18}/cm^3$ or more) extra term is necessary to account for the effect of FCA. In equation (4.2) interband absorption is given by the linear absorption coefficient α and the FCA by the cross-section σ . Both variables are independent of light intensity. The FCA concentration is equal for electrons and holes at high excitation levels and is denoted by $n(z, t)$. The variation of the light intensity $I(z, t)$ with respect to the distance z from the surface is given by the total absorption [85]

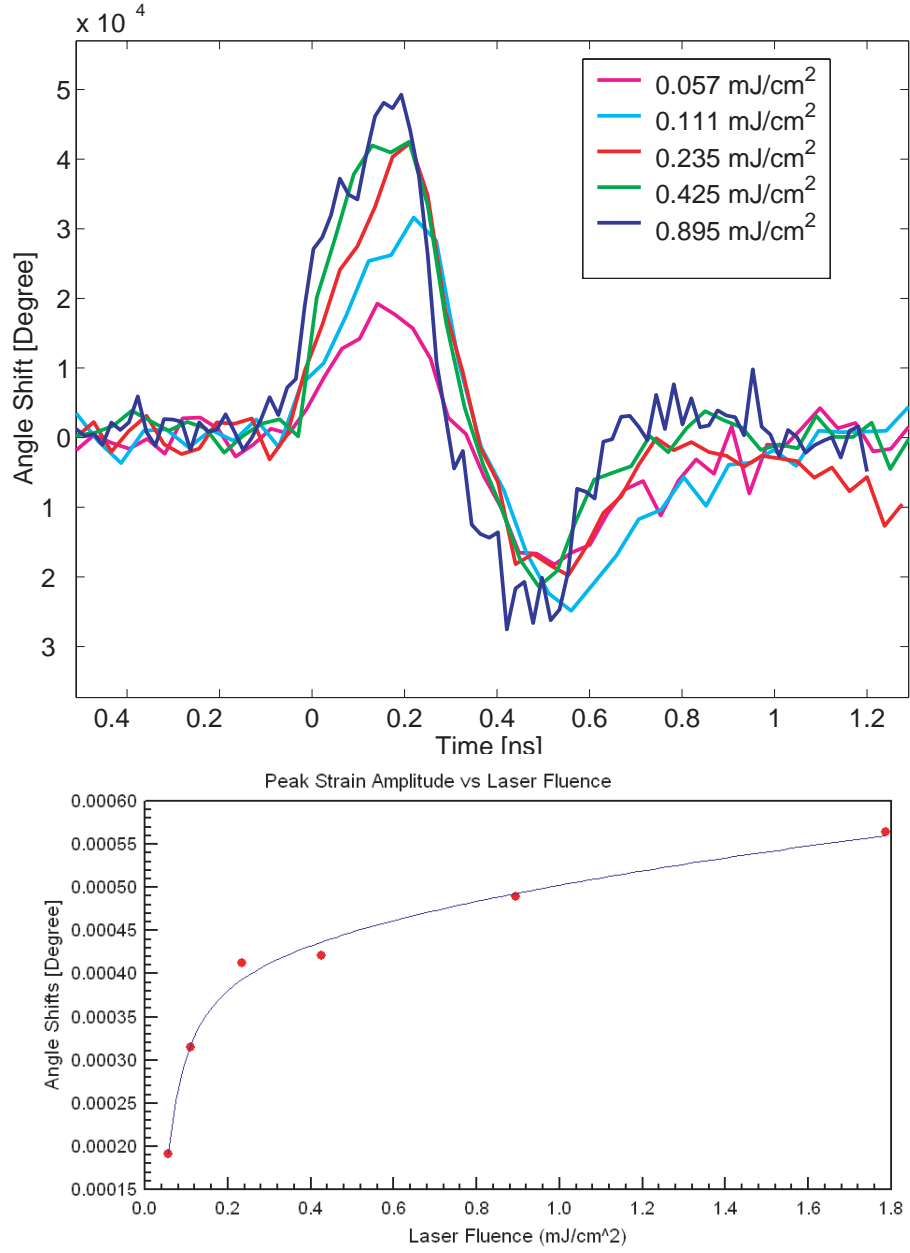


Figure 4.11: Amplitude of strain pulse saturates at high laser fluence levels. Plot on left shows propagation of strain pulse in AlGaAs at different laser fluence. Plot on right shows how maximum amplitude of the strain pulses varies depending on the fluence. This optical limiting effect is credited to free carrier absorption process, which may be better known as free carrier absorption.

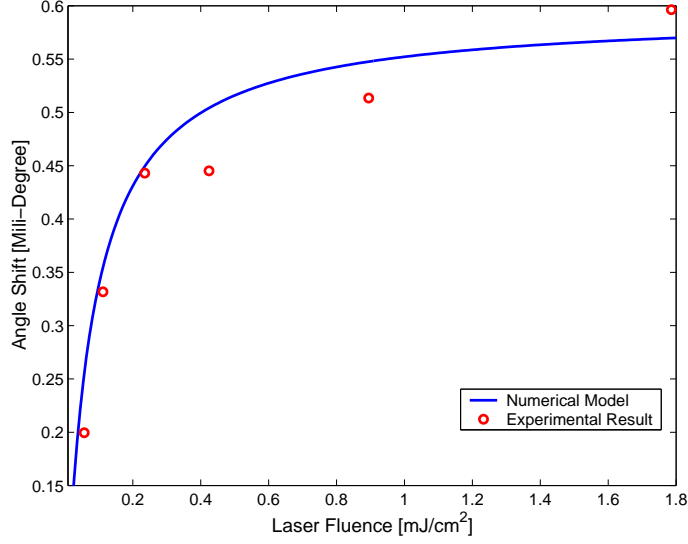


Figure 4.12: After accounting for both the interband absorption and the free carrier absorption by its cross section, numerical model now simulates the optical limiting effect.

$$\frac{\partial I(z, t)}{\partial z} = -(\alpha + \sigma \cdot n(z, t)) \cdot I(z, t) \quad (4.2)$$

From equation (1) and (2), we solve for the density,

$$n(z, t) = \frac{n(0, t) \cdot \exp(-\alpha \cdot z)}{1 + \frac{1}{2} \frac{\sigma}{\alpha} n(z, t) \cdot [1 - \exp(-\alpha \cdot z)]}$$

Typically the value of the free carrier absorption cross section coefficient for GaAs crystal at 800 nm is expected to lie between 10^{-15}cm^2 and 10^{-17}cm^2 . However precise value of the parameter for GaAs and at this laser wavelength has not been reported to my knowledge. Figure 4.12 shows the Bragg peak shifts at different laser fluence for both the simulation and experiment. From a best fit of the numerical model to the data, the FCA cross section value of $\sim 6.6 \times 10^{-16} \text{cm}^2$ was obtained. This value is used for the rest of the simulation in following sections.

Comparison between Experiment and Simulation

The modified carrier density distribution due to FCA alters both the film and the substrate dynamics, which is significantly different from the case where linear absorption coefficient was the dominant term for photon absorption. As can be seen in Figure 4.13, the numerical model without the incorporation of FCA does not correctly predict the experimental data. For instance, the data shows that the amplitude of the initial compression pulse is considerably greater than the amplitude of the tensile pulse in the film layer (See Figure reffig:schemes). However the earlier simulation shows that the amplitude of the strain and tensile pulses are equivalent. There are other distinctive features between the data and the simulation in the GaAs substrate level. The model initially predicted that in the time scale of the tensile pulse coming back to the substrate, non equilibrium lattice dynamics are mostly governed by the strains generated from the deformation potential. However experimental data clearly shows that prominent heating mechanism develops during the time scale less than 1 ns from the photoexcitation. Magnitude of the strain generation by this heating is nearly comparable to that of the deformation potential-based strains as well. Most plausible explanation for this fast heating mechanism is excess kinetic energy from the free carriers being directly relayed to phonon system thus to heating up the lattice.

In interband excitation process, the photons do not directly contribute to the rise of lattice temperature until the carriers recombine and give off their kinetic energy. Due to FCA, the probability of light transmission through the crystal be-

comes smaller because of the reduced optical penetration depth and extremely high carrier density. When the crystal itself becomes more opaque to incident photons, the crystal experiences vastly enhanced auger recombination and this enhances the heating process. Figure 4.14 shows the comparison between the experimental data and simulation after effect of FCA to carrier density distribution and heating of the substrate are taken into account. Despite minor deviation between the data and the simulation, numerical modeling now resembles the data very closely. At these density level, some of earlier assumptions may begin to break down. For example, it is possible that the highly energized free carriers from FCA diffuses into the film layer from the substrate. However we were not able to observe such diffusion process at this time.

4.3.4 Long Thermal Equilibrium Process

Unlike early time scale dynamics where various effects such as free carrier absorption, Auger recombination, and carrier diffusion competes, later time dynamic is much simpler to deal with. After a few hundred nanoseconds to microseconds later, the majority photoexcited electrons recombines with holes and the energy goes to the lattice. AlGaAs and GaAs come to a thermal equilibrium at different rate because two materials carry distinct thermal conductivity.

Figure 4.15 shows that GaAs substrate lattice constant is expanded much more than in the AlGaAs because of free carrier density distribution with excess kinetic energy to spare to phonon bath is confined in the substrate level. At sufficiently early times (within 10s of nanoseconds) AlGaAs medium begins to heat up as thermal

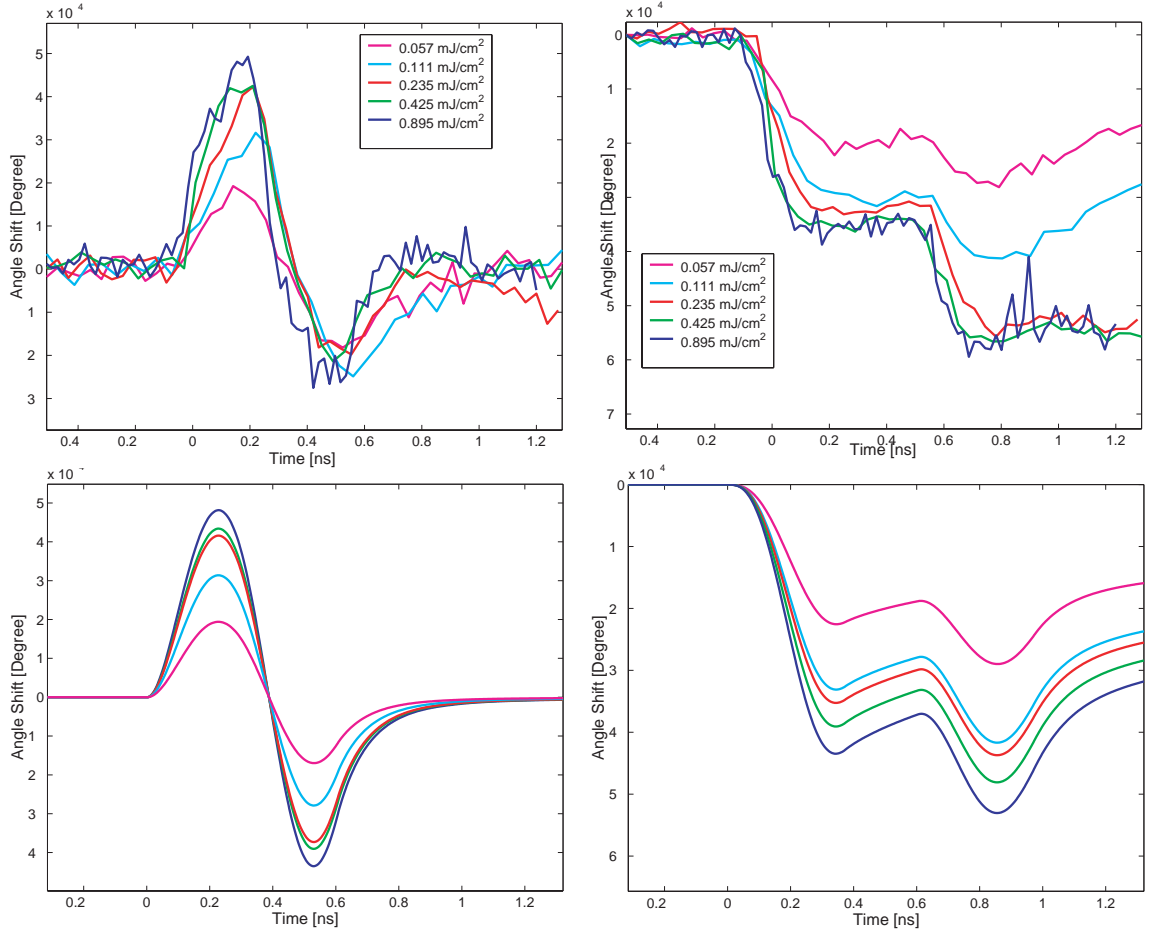


Figure 4.13: Numerical model still does not predict the data even after the saturation in carrier density has been taken into account. Notice that ratio between the compression pulse and the tensile pulse in the film layer drastically deviates from 1 at high laser power. Also notice that there is considerable heating effect at higher laser fluence, which develops relatively slowly within 1 ns period in the GaAs substrate.

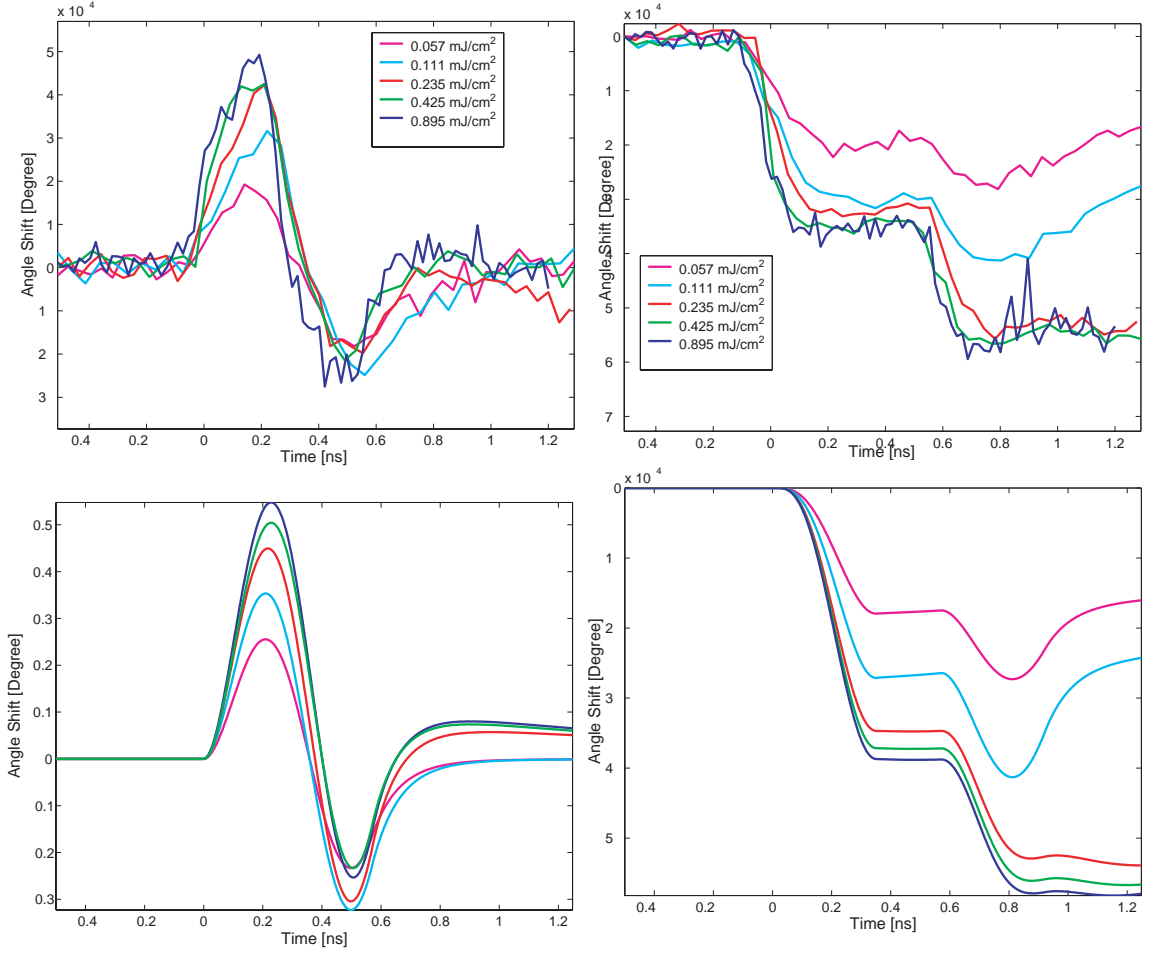


Figure 4.14: After incorporating free carrier interband absorption, numerical model follows the experimental data much closely. Top left shows the strain propagation in AlGaAs and bottom left is the simulation. Accordingly top right shows the strain generation and propagation in GaAs substrate and bottom right is the numerical counter-part.

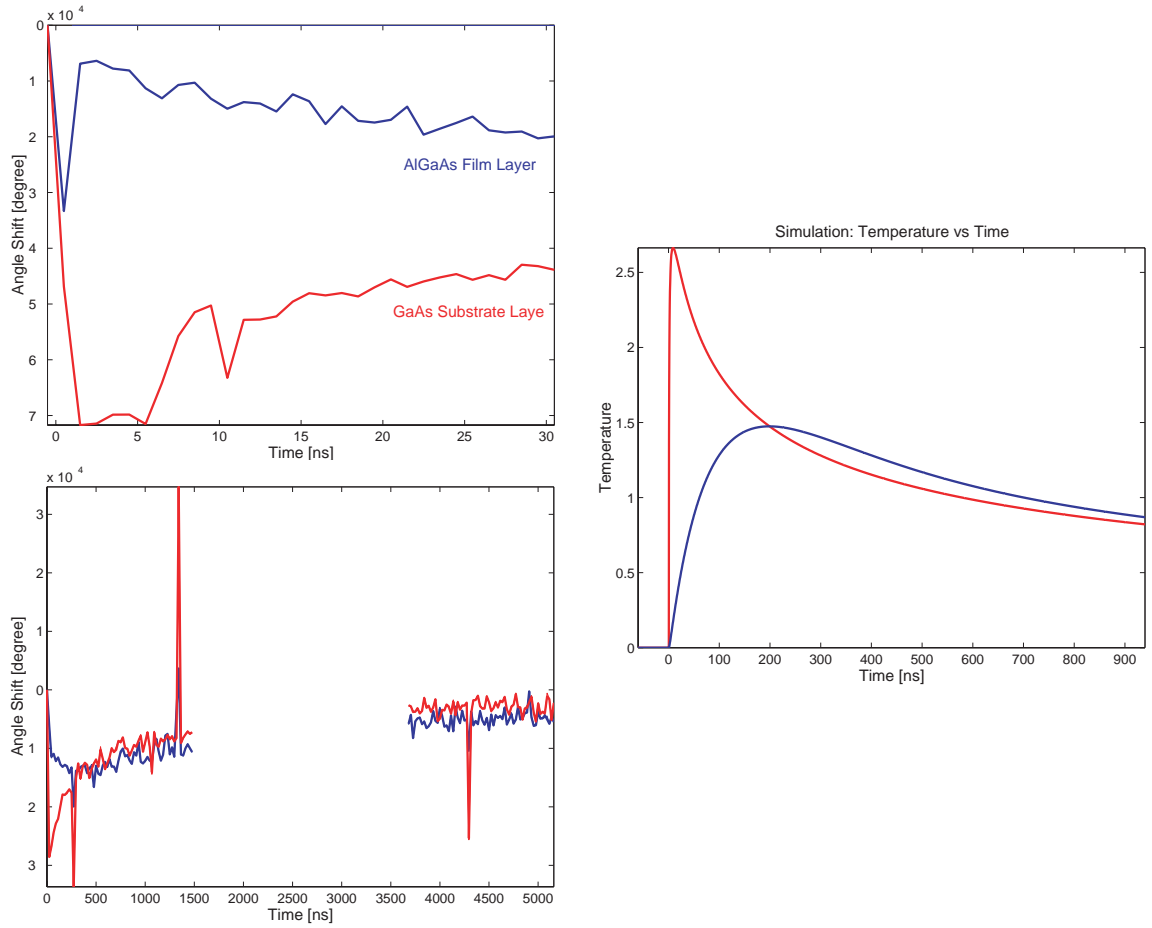


Figure 4.15: long term thermal behavior of the multilayered structure. Initially as heated surface of the GaAs substrate cool down the film layer begins to heat up as heat energy gets transmitted through the interface. Eventually both systems come to a thermal equilibrium.

conduction takes place at the heterostructure interface. Approximately 200 ns later two semi-conducting medium comes to a thermal equilibrium at the interface and begins to cool down together. This mechanism is well predicted by solving thermal diffusion equation at the boundaries (See Figure 4.15). In the data figure, there are occasional spikes separated by several hundreds of nanoseconds. The spikes are strain and tensile pulses that are bouncing inside the crystal, from which we can deduce thickness of the wafer. We can also learn about thermal conductivities by observing heat exchange processes between two materials.

CHAPTER V

Time-Resolved Inelastic X-Ray Scattering

5.1 Motivation

The field of time resolved X-ray diffraction extends to studying non-equilibrium phonon dynamics of various wave vectors. When one applies intense light on a semiconductor material, charge carriers (electrons or holes) with an excess kinetic energy, $\Delta E \geq \frac{3}{2}kT_l$, where T_l is the lattice temperature, are expected to lose the energy by emitting incoherent phonons until the equilibrium condition, $\frac{2\langle\Delta E\rangle}{3k} = T_e = T_h = T_l$, is reached. During this process, the energy relaxation routes of the free carriers are initially dominated by the emission of optical phonons: the interband process creates LO and TO phonons within a narrow band of allowed wave vectors ($q \approx 0$). Subsequently the optical phonons with frequency Ω decay to acoustic phonon pairs with approximate half the frequency $\Omega^* = \Omega/2$.

The high frequency non-equilibrium acoustic phonons in semiconductors have been extensively studied a variety of different methods such as Brillouin scattering, Raman scattering, detection with bolometer and Tube X-ray source scattering [86, 87, 8, 9, 88, 89]. However each of the previous method had short-comings. For

instance, Brillouin scattering allows one to directly measure the wave vector and polarization component of the scattering acoustic phonons with good sensitivity and time resolution. However its wave vector range is limited to be near the Brillouin zone center (accessible wave vector range is about $1/1000$ of the full zone). Raman scattering can give accurate frequencies of Raman active phonon modes, however, again only at the zone center or zone boundary for the second order scattering. Other methods suffer from relatively slow intrinsic time resolution of the electronic devices. Furthermore most of these experiments were carried out in a specially designed lab environment where the sample is kept under liquid Helium temperature. I note that the study of room temperature dynamics is highly desirable because most of the semiconductor devices operate at the room temperature. There certainly are gaps in our current understanding of the non-equilibrium phonons. Elastic X-ray scattering at the advanced synchrotron facilities may provide us with opportunities to study such phonon dynamics in unprecedented precision and time-resolution. Measurement of the emerging angles of scattered X-rays from the sample yields direct information about the phonon spectrum because X-rays scatter with emission/absorption of phonons. In general the resolution of minute phonon frequency shift (< 1 meV) is difficult, if not impossible, to measure with a typical spectroscopy or elastic scattering methods. Nevertheless total scattered radiation of all frequencies as a function of scattered angle in the diffuse background can still be measured away from the Bragg condition.

In this chapter, we look into uniaxial properties of strain propagation. By de-

iving dispersion relations for phonon modes propagating at different directions, I have investigated the uniaxial properities of the strain generation and propagation. Furthermore by utilizing the large wave vector of the X-ray probe, we present initial studies of high frequency phonon dyanmics that are not limited to the coherent population.

5.2 Experimental Schemes

In the experiments that will be covered in this chapter, direct observation of laser induced LA phonons (coherent and incoherent) in a bulk Indium Antimonide (InSb) is accomplished using ultrafast laser pumped and X-ray probed time-resolved scattering. This particular material is chosen over more prefect crystal such as Si or GaAs because it is a polar semiconductor with a narrow direct band gap (0.17 eV). Thus, we expect to generate large density laser induced phonons upon ultra-short (femto-second pulse width) high power laser excitation [86, 4].

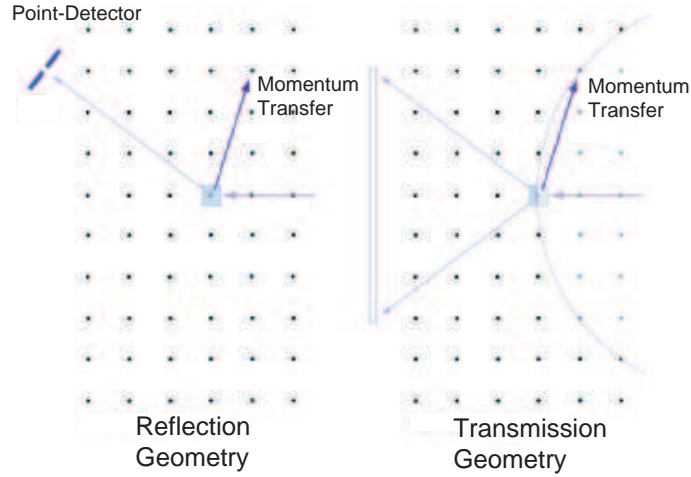


Figure 5.1: Two types of X-ray scattering setup. Figure on left shows a point detector scheme, while figure on right shows imaging scheme to study phonons. Through out most of the work covered in the thesis, first method was used.

There are two geometries to measure wave-vector dependent phonon dynamics (See Figure 5.1) using X-ray scattering. The first one is in standard reflection geometry, where the momentum transfer is a point like probe of reciprocal space determined by the sample and detector orientation. A second case is in transmission geometry where an area detector collects the scattered X-rays behind the sample. In the latter, the momentum transfer is a planar projection of the detector is onto the Ewald sphere, and thus this scheme is capable of providing a simultaneous collection of a spherical surface in reciprocal space.

5.2.1 Transmission Geometry

The transmission geometry is favored in various synchrotron based experiments because it is much simpler to setup and it provides overall pictures of phonon spectrum in a very intuitive form. In this method, X-ray is directed to the sample perpendicular to the surface of the sample. And scattered X-rays coming out of the opposite face of the sample surface are collected with an imaging detectors such as image plate and X-ray CCD camera. In above example, the X-ray scattering is due to thermal vibration of atoms, and is called thermal diffuse scattering (TDS). The amplitude of the thermal vibration is given in terms of phonon density,

$$I_{TDS} = \frac{\hbar}{2M} \sum_j \frac{|Q\varepsilon_j(q)|^2}{\omega_j(q)} \left\{ n_j(q) + \frac{1}{2} \right\}. \quad (5.1)$$

where M is that atomic mass, $j = 1, 2, 3$ indexes the three modes of polarization vector, and $\omega_j(q)$ is the frequency of the phonon and n is the phonon density given by Bose-Einstein statistics.

In preliminary experiments, we measured the TDS signal from a GaAs wafer

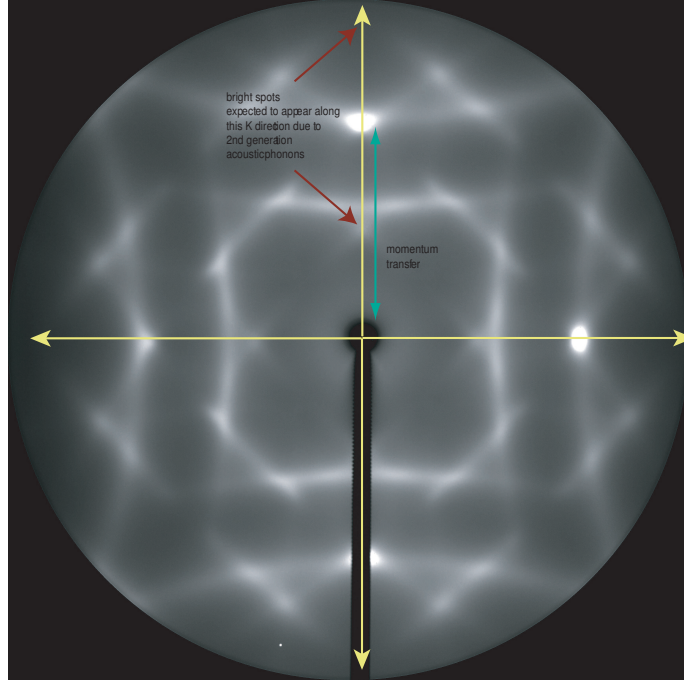


Figure 5.2: Imaging of thermal population of phonons in (100) GaAs crystal. This phonon image was taken back in 2003 when we were still trying to use imaging method to study laser induced phonon dynamics.

(See Figure 5.2). This method simultaneously collects diffuse scattered X-rays from multiple reciprocal sites, which translates to drastic advantage in data acquisition rate compared to the point detection scheme. Nevertheless this detection scheme was later not pursued for a few reasons. First unless whole experimental carried out under vacuum or Helium gas enclosure, measurements of scattered X-rays are very susceptible to heavy air scattering. More importantly we could not gate the image plate because our X-ray chopper was permanently damaged.

5.2.2 Reflection Geometry

In the reflection geometry, (100) surface oriented InSb crystal is placed at the center of the HUBER goniometer and probed with X-ray photons at an energy of 10 KeV. SPEC is a data acquisition software that controls diffractometer and automates

data acquisition procedure. It is often used in a diffraction experiment because it calculates for the orientation matrix that converts the real space coordinate to reciprocal space coordinate of the sample. SPEC takes two calibration reflections and then calculated appropriate orientation matrix so that we probe the lattice structure scan reciprocal space coordinate instead of angles (See Figure 5.3). Using an APD as the point detector, we perform a single photon counting diffraction experiments.

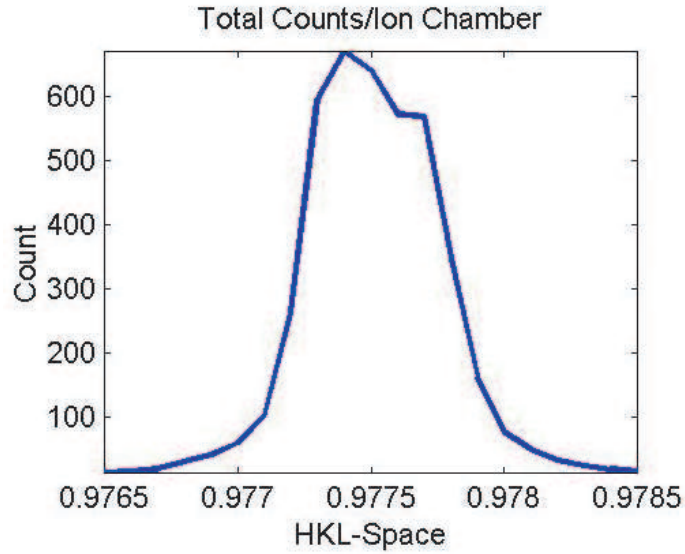


Figure 5.3: Rocking curve of InSb about 111 reflections. Slight deviation on HKL space is due to systematic error in orientation matrix. Nevertheless for our application, the deviation can always be accounted for during error analysis.

From a dispersion relation of the material we can directly relate reciprocal space value to phonon frequency/energy. Time-resolved aspect of the setup is identical to previous experiments. However it is important not to exceed the maximum data acquisition rate. For this purpose HUBER detector arm is equipped with automatic filter box, so that we can control the count rate going into APD without accessing the X-ray hutch.

5.3 Non-Equilibrium Lattice Dynamics in InSb

5.3.1 Uniaxial Property of Propagating Strain

Measurement of X-ray diffraction from laser induced coherent acoustic phonon propagation at frequencies up to tens of Gigahertz was previously made and confirmed with numerical simulations [4]. It has been found that the laser induced phonon dynamics is consistent with an interpretation that impulsive excitation of a solid occurs on a time scale shorter than the material hydrodynamic response time and generates coherent acoustic phonons across a range of wave vectors near the Brillouin zone center and peaks at a wave vector of order one inverse laser penetration depth [3]. In our experiments, we used SPEC to scan through various known directions. We initially scanned the momentum transfer along (111) direction at various time series about the 111 Bragg reflection. And then later we scanned the momentum transfer perpendicular to the surface normal to verify the existence of non-uniaxial strain components.

Parallel to Surface Normal: Scan along (1 1 1)

Figure 5.4 shows the time and angle (momentum transfer) scan. In the figure, each line out along the time axis is a time scan of a particular phonon mode. Each time scan shows an oscillatory behavior in the X-ray diffraction efficiency (See Figure 5.5). By obtaining the periodicity of the oscillation with Fourier Transform as a function of the wave vector, the acoustic phonon dispersion relation is mapped out near the Brillouin zone center (See Figure 5.6). By assuming the properties of uniaxial strain pulse [3], we are able to deduce speed of sound in InSb along (111)

direction. With the proper unit conversion: $Speed = \frac{(Frequency) \times (LatticeSpacing)}{(\Delta q)}$, we obtain a value for LA phonon speed to be 3807.6 m/s, which is closely matched to the tabulated value of 3880 m/s. Our data clearly indicates that the strain wave along (111) direction consists of LA phonons.

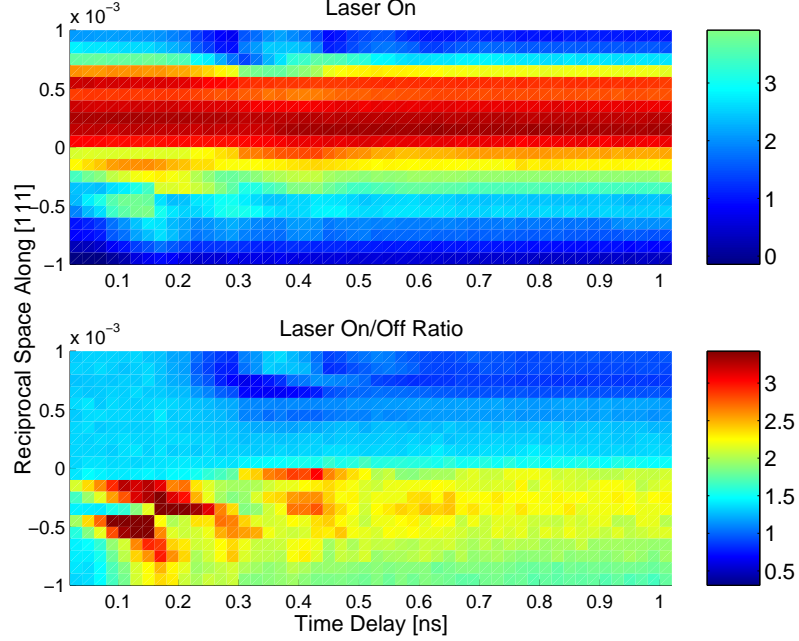


Figure 5.4: 2D (reciprocal space along (111) and time) scan about (111) Bragg reflection in InSb. We are able to observe coherent lattice vibrations slightly away from Bragg condition (zone center). Oscillations too far off the zone center cannot be resolved due to limitations in current probe pulse duration.

5.3.2 Perpendicular to Surface Normal: Scan along (1 -1 0)

In our previous data, we observed coherent motions of lattice along (111) direction in this (111) surface oriented InSb sample (See Figure 5.7). If the strain wave is indeed uniaxial, we should not see any coherent oscillation along perpendicular direction to the surface normal such as along the direction of (1-10). Figure 5.7 shows 2D scan: reciprocal and time scans along (1-10) direction.

Contrarily to our expectation, we observe coherent oscillations of lattice along

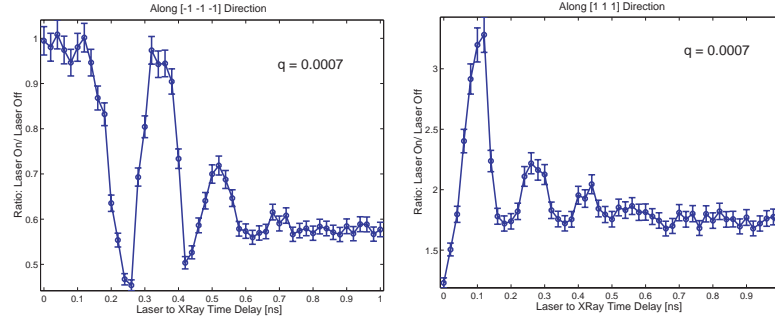


Figure 5.5: Time scans in InSb at particular wave vector, $q = 0.0007$. Basically each line out of Figure 5.4 should look like this except lower q value corresponds to oscillation at lower frequency: High q means higher frequency.

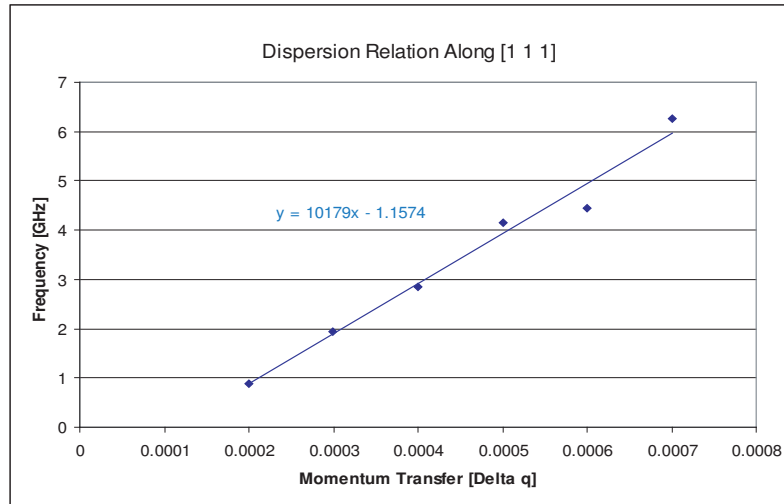


Figure 5.6: Experimentally observed oscillation frequency vs. wave vector. The slope should give out the group velocity of LA phonons along [111] direction. Dispersion relation of the material near zone center has been mapped out.

(1-10) with a comparable amplitude to the previous scan taken along (111). The result shows coherent phonons that are polarized along (1-10). We mapped out a dispersion relation for this data set and calculated for the speed of sound. We obtain value of 2032 m/s that is off by almost factor of 2 from LA phonon values. We strongly suspect that the oscillation is result of TA phonon propagation. Tabulated value for TA along is 1870 m/s, and along 110 are 2290 and 1620 m/s respectably.

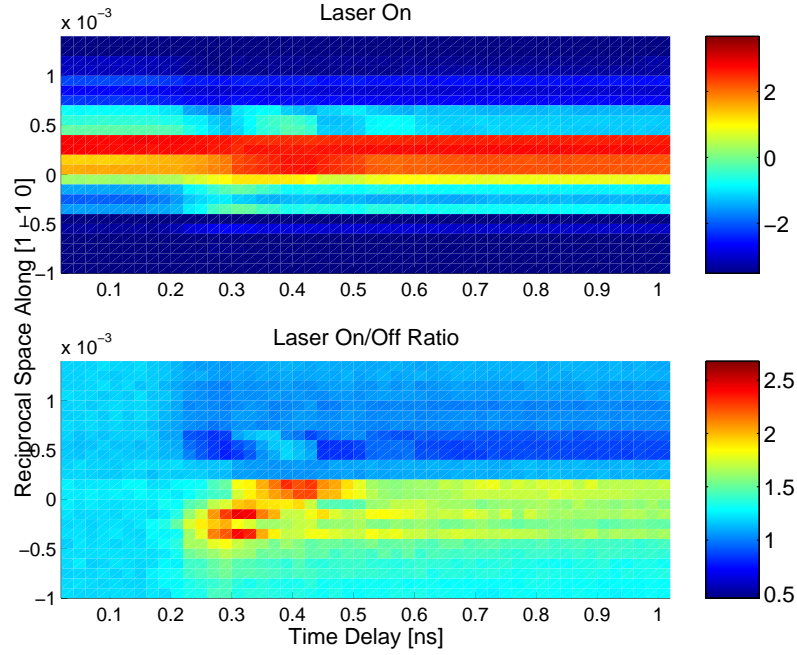


Figure 5.7: 2D (Reciprocal space vs. Time) scan about (111) InSb Bragg reflection. The scan was taken along (1-10) direction, which is perpendicular to previous scan direction. Presence of oscillatory behavior of lattice on this orthogonal vector direction suggests that impulsively generated strain may not be uniaxial.

This is a puzzling new finding, which demonstrates a strong possibility that the impulsive generated strain is not, at least in this time scale, consist of mostly LA modes of phonons. Mechanism of TA phonons generation at this time seems unclear. Surface wave generated from surface imperfection of this bulk sample can be strong possibility for TA phonon mode generation. We note that there is 200 ps time delay

between time zero and when the strain begins to build up in above scan. Notice that in Figure 5.7, the strain develops considerably slower than in Figure 5.4. In fact we find that there is no laser induced strain effect perpendicular to the strain propagation direction (1 1 1) until 200ps after the photoexcitation. 200 ps is sufficient time for low frequency phonons to travel a distance of approximately $1 \mu\text{m}$, which closely corresponds to the penetration depth of the X-ray probe. As the phonon mode spreads through out this probing region, we become more sensitive to them. Considering the fact I could see coherent motions of oscillation in any arbitrarily chosen direction, the explanation of the surface acoustic wave seems quite feasible at this time.

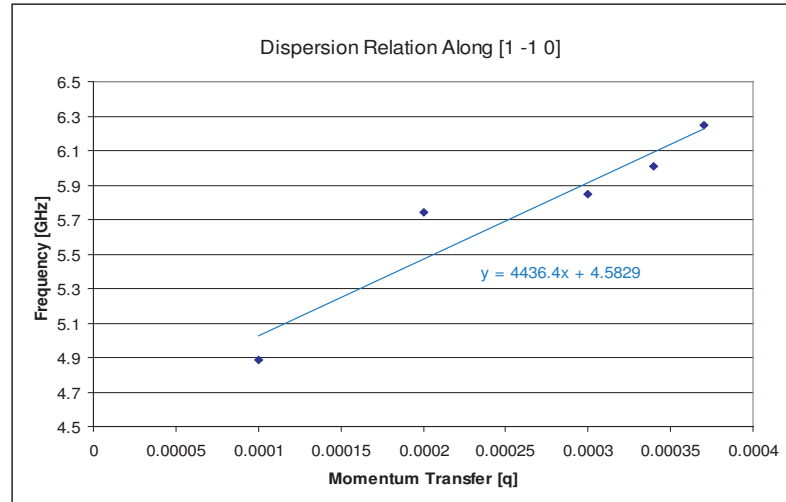


Figure 5.8: Experimentally observed oscillation frequency vs. wave vector along [1 -1 0]. The slope gives out the group velocity of TA phonons potentially along any direction.

5.4 Observation of Terahertz Acoustic Phonons

Up until now, I have mostly studied incoherent or/and coherent acoustics at relatively low frequency ranges where propagation of strain pulses and associated

phonon modes are well predicted by the wave equation of the lattice dynamics in the continuum limit. Figure 5.9 shows the spectrum of acoustic waves inside InSb that we have explored. According to the figure, at above frequency of 20 GHz, laser induced effect seems to disappear. However, given a long enough data acquisition time to improve the statistics, the presence of non-equilibrium phonons can be observed at much higher frequency (See Figure 5.10). The data shows that presence of the non-equilibrium phonon population extends to near 1 THz.

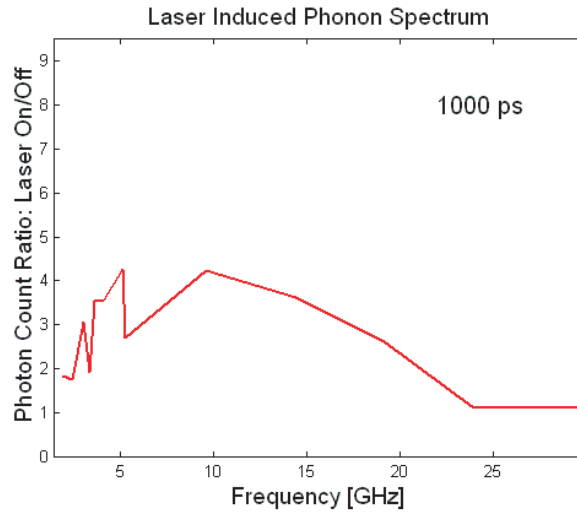


Figure 5.9: Temporal evolution of laser induced phonon frequency spectrum at low LA branch. Initial bandwidth of the mode is narrow [see top left], but it becomes broad as time progresses. And also center of the frequency slowly toward lower frequency region.

The fact that our experimental scheme is sensitive to phonons with frequency near a THz or above at the room temperature opens the door for time-resolved study on THz phonon populations upon ultrafast laser excitation. The acoustic mismatch model and most phonon wave dynamics work under the assumption that phonons are governed by continuum acoustics because we deal phonons with wavelength much greater than typical inter-atomic spacing. However, for high frequency phonons

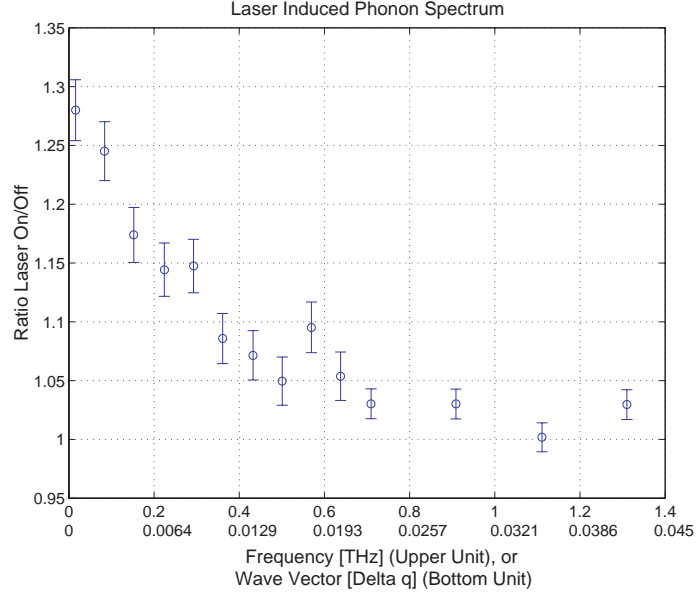


Figure 5.10: Laser induced effect on lattice dynamics extends far more than what we just demonstrated. Current experimental scheme is capable of studying phonon dynamics at up to frequency of 0.5 THz where treatment of continuum dynamics of lattice dynamics will break down.

(~ 100 GHz or higher), continuum acoustic correlation at solid interfaces or bulk material does not hold any longer. More advanced theoretical models should complement such new experimental findings, which is beyond the scope of this study at this time.

5.5 Laser Induced Zone Boundary Acoustic Phonons

We made a serious effort to see an existence of high frequency ($4\sim 5$ THz) acoustic phonons at zone boundary, which are the direct down-conversion products from the optical phonons (LO mode). This is an extremely daunting task because at such large wave vectors, data acquisition rate of the time-resolved study becomes very small (~ 0.1 Hz). And also there is no assurance that we have sufficient time resolution to see this phenomena that has been mostly theoretically laid out [86, 90]. Ones again

InSb sample was used. This time, however, geometry of grazing incidence of X-rays is used (~ 1 degree). The grazing incident geometry limits the penetration of X-rays to about 200 nm, which is relatively well matched with the optical penetration depth of 100nm at a wavelength of 800 nm.

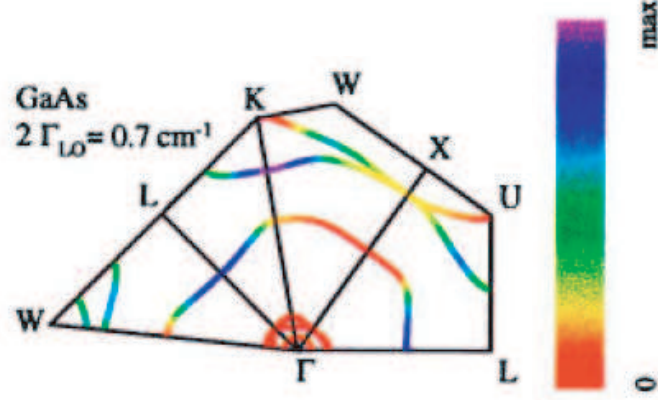


Figure 5.11: Theoretical prediction of phonon population distribution upon ultrafast laser excitation. The colored scale on the right side of the contour figure gives the p phonon density. The non-equilibrium phonon population has a preferential decay direction along K. Other less dense non-equilibrium phonon populations may also be observed in our experiment [8][9].

Due to very low count rate, educated guesses were necessary to pick regions of our interest. Theoretical work has been laid out by Debernardi [9] for GaAs, a crystal with very similar structural properties to InSb. Three reciprocal sites $(3.5 \ 3.5 \ 3.5)$, $(2.5 \ 3.5 \ 2.5)$, and $(2.5 \ 3 \ 3)$ were chosen. We oriented the crystal and the goniometer such that the detector probes the designated reciprocal spaces. Afterwards we counted for about 5 hours at each point. On $(2.5 \ 3.5 \ 2.5)$, where we expect mixed mode of LA and TA, the ratio during laser excitation was 1.02 ± 0.05 and 3.8 micro-second later the ratio was also 1.02 ± 0.05 . On $(2.5 \ 3 \ 3)$ where very small laser induced phonon population is expected, ratio during and after

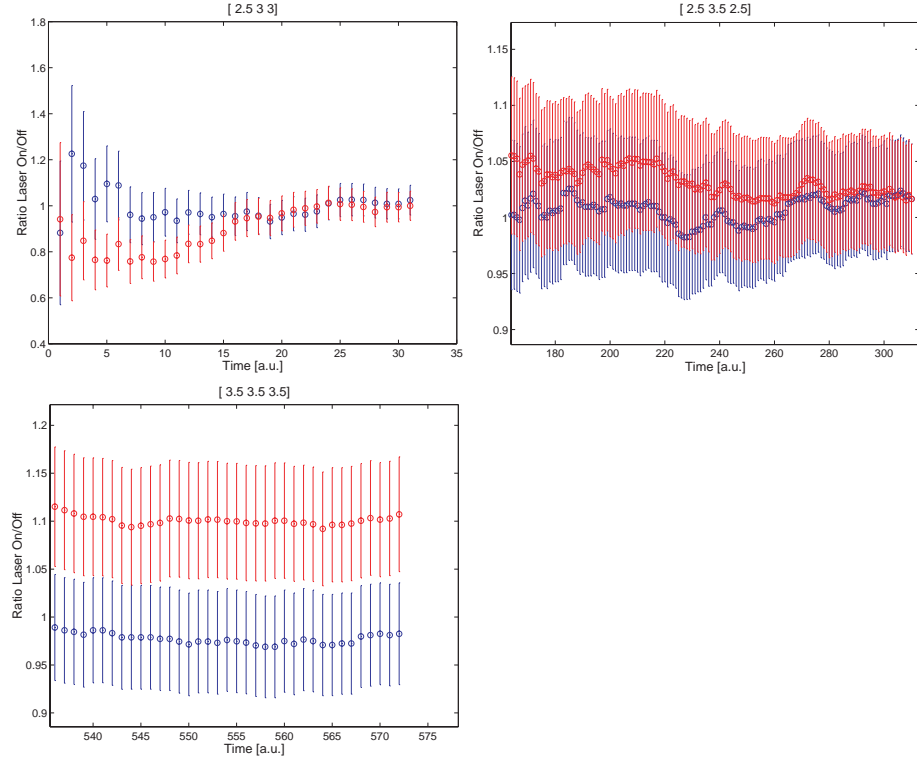


Figure 5.12: Three zone boundary regions were chosen for the counting experiment. As time progresses error bar becomes smaller as our statistics gets better. On first two sites, the ratio basically converges to 1. Nevertheless on zone boundary along $[1\ 1\ 1]$ direction, there is a considerable laser induced effect.

the laser incidence were both 0.99 ± 0.06 . On first two measurement, we did not observe any effect that is statistically significant. However on our last scan on (3.5 3.5), 2σ effect was observed. The ratio between laser on and laser off was 1.11 ± 0.06 during the laser incidence and 0.98 ± 0.05 after 3.8 micro-seconds later. Although very limited amount of data has been collected, the result implies physical significance. At the zone boundary, there exists a laser induced effect with directional preference. The data may indicate that we are directly observing the down conversion of phonons; however to be convincing it would be desirable to take full spectrum at multiple delays with significantly better statistics. At this point, the success of the experiment is severely limited by X-ray photon flux at the current synchrotrons. We can improve the experimental setup by using higher repetition rate lasers such as a regenerative amplifier that runs at 100s of kHz. Even then, our measurement may still be limited by the time-resolution of the X-ray probe. Ultimately I believe that the experiment can be accomplished at more advanced X-ray source facilities such as Linac Coherent Light Source, of which details will be presented in following chapter.

CHAPTER VI

Summary and Outlook



Figure 6.1: Taking Static Images with X-rays. Floral Radiography. X-rays are used to take still picture of flower. Differential transmission of X-rays through the flower is imprinted on to X-ray film [10].

Nowadays people are very familiar with the term X-rays. Kids that are barely old enough to attend an elementary school seem to be aware of their ability to pass and see through matter. Their use has been embedded in our every day lives for some time. Aside from doing my research, I personally benefited from the use of X-rays when I fell off from my skate-board and injured myself last year. Nevertheless

when I talk about doing a time-resolved study using X-rays, I often receive confused reactions, even from people with considerable science background. Typically when people talk about usefulness of X-rays, their practical use as a powerful spatial probe comes to their minds because conventional knowledge of X-ray are tied to making pictures of static objects (See Figure 6.3).

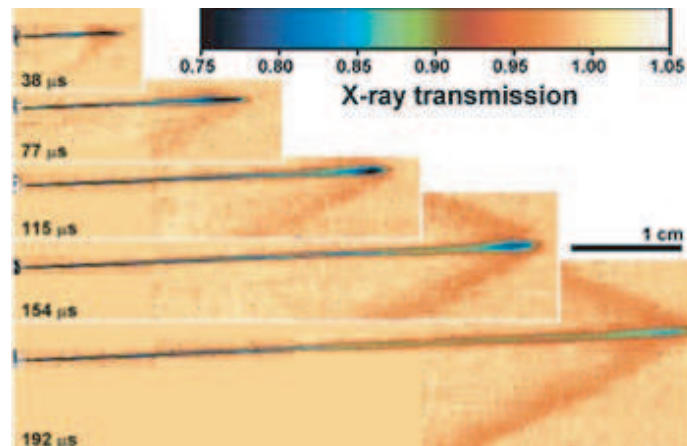


Figure 6.2: Making Movies with X-rays. Fast time dynamics such as fuel-injection system can be studied with time-resolved X-ray technique. Researchers at Argonne National Laboratory can monitor amount of X-ray energy that is absorbed by the fuel spray. Micro-second dynamics of fuel spray cannot be probed with optical method [11].

Since the discovery of X-ray radiation by Wilhelm Roentgen in 1895, X-rays have been the most useful probe of the microscopic properties of materials. Attributes of X-ray radiation such as its short-wavelength, long penetration depth and strong interaction with core electrons are particularly useful when exploring structural properties of condensed matter systems. Applications of X-rays extends from scientific researches such as probing biological tissues and nano-crystals up to taking parts in manufacturing industrial tools and metallurgical or chemical substances. However, demands from the scientific communities for more sophisticated use of X-rays led to

rapid developments of advanced apparatus and facilities such as X-ray Synchrotrons. Nowadays with an arrival of very bright monochromatic X-ray source which carries very small spatial divergence, structural and material properties of various systems are studied with unprecedented precision and accuracy. From the beginning, the aspect of spatial resolution of the X-ray has been vastly emphasized and explored. On the other hand, its temporal resolution as a probe is much less appreciated.

Contrarily to popular beliefs, idea behind the time-resolved X-ray science is quite simple. Just as one could make a movie of a moving object with camera-recorders, real time dynamics of a matter at an atomic level can be studied with X-rays provided that we have fast enough shutters. Experimentally, it is still quite challenging. As early as 1980s, the time-resolved aspect of X-ray science has received significant attention. But the actual progress has been rather slow until late 1990s when ultrafast laser technologies and advanced X-ray sources such as synchrotrons were introduced. Since then several novel approaches for exploring the temporal characteristics of condensed matter systems have been pursued (See Figure 6.2). Nonetheless, the field of ultrafast X-ray physics is relatively new.

6.1 Progresses in Time-Resolved X-Ray Science

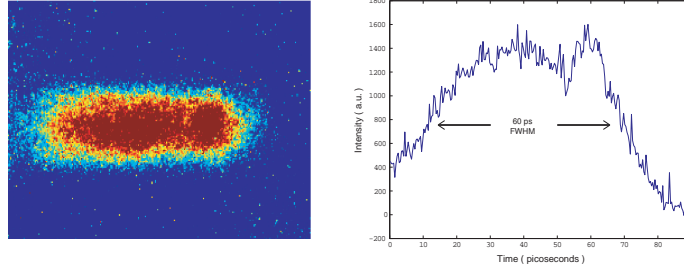


Figure 6.3: A streaked image of an 10KeV X-ray bunch measured with a X-Ray streak camera on April 4, 2003. The detector is developed at David Reisaf group at the University of Michigan. A FWHM of 60ps was measured.

Current time-resolution of experiments at the third generation synchrotron is typically limited by the X-ray pulse duration of about 100 ps. This is about three orders of magnitude longer than the time-resolution that is routinely achieved in ultrafast optical pump-probe experiment. This short-coming hinders our understanding of transient dynamics that occur at shorter time scale than the X-ray pulse duration. Another aspect of ultrafast X-ray science, which requires a vast improvement, is flux. In the X-ray pump probe experiment, count rate is limited by the repetition rate of the laser system, which typically ranges from a kHz to hundreds of kHz at best. The repetition rate of the X-ray pulse is a few MHz. For every X-ray photon we collect, a few thousands will be lost.

Among the efforts to improve the time-resolution in the X-ray pump-probe experiment, X-ray streak camera can be used to reduce the pulse duration down to a few picoseconds. In this device, X-ray photons strike the cathode, which is kept under vacuum inside the camera, and generates an electron pulse that inherits the temporal profile of the initial X-ray pulse. The electron bunch propagates between two deflection plates. When the electrons pass the plate region, a ramped voltage

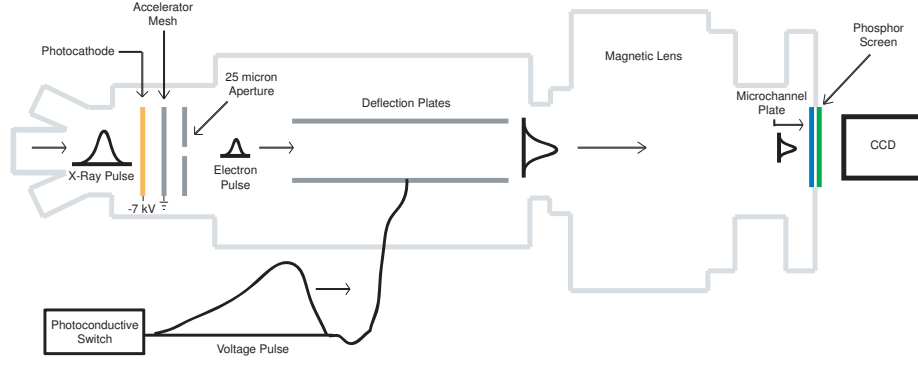


Figure 6.4: A compact streak camera developed in David Reisaf group at the University of Michigan. X-Ray pulse incidents upon a CsI photocathode, which subsequently emits secondary electrons. The electrons are then accelerated by an applied electric field down the bore of the detector. The rising edge of a voltage pulse is applied to the deflection plates as the electron bunch passes by. Electrons arriving at separate times experience a different deflection voltage, and thus the electron bunch become streaked. The bunch is later amplified and imaged by micro-channel plate, phosphor screen and a CCD.

from a photo-conductive switch is applied to each plate. The beam is swept by the ramping electric field and electrons at the leading edge of the pulse are mapped to different location on the phosphor screen from the electrons at the trailing edge. Use of this device was successfully demonstrated [12] by measuring coherent acoustic phonon oscillations up to 0.1 THz in InSb bulk crystal. Nevertheless low quantum efficiency often limits versatility of the experiments.

Among other techniques to produce femtosecond time-resolution, a slicing technique has drawn much attention lately. In this scheme ultrafast laser beam co-propagates with electrons through a wiggler and generate significant energy modulations in the electrons that are temporally overlapped with the laser pulse. The modulated electrons later are spatially separated from the main electron bunch in the dispersion section of band-magnets and produces monochromatic X-ray beam with femtosecond pulse duration. This noble project is under preparation at the Ad-

vanced Light Source and it will be used for experiments starting early 2006. While the schematics described above may deliver much shorter X-ray pulse, it comes at an expense of losing a lot of X-ray photons.

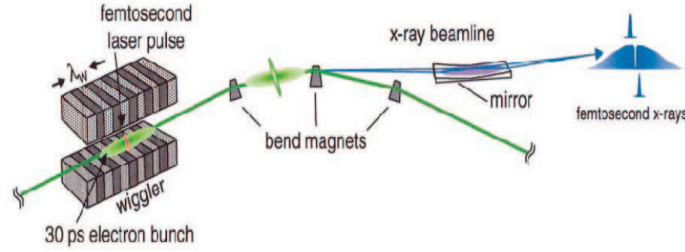


Figure 6.5: Schematics of the slicing source that are under development at Advanced Light Source [3].

Recently linear accelerator based ultrafast X-ray source has been developed. In this scheme the electron bunches from an injector are compressed through two stages. First energy chirp is introduced to the electron bunch by applying RF field to create a correlation between energy and length along propagation direction of the bunch. And then this chirped electron bunch is compressed while propagating through dispersive section where trailing edge of the bunch catches up with the lead edge. Sub-Picosecond Pulse Source (SPPS) follows above scheme to produced 80fs FWHM X-ray pulses at a repetition rate of 10 Hz. In this case, upper limit of the time-resolution in a pump-probe experiment is set by jitter between the accelerator machine and the laser system (a few picoseconds). Thus it is necessary to devise an alternate method to fully utilize the capability of the machine.

Cavalieri et al [12] have recently demonstrated that relative arrival time of the electron bunch to the laser can be measured within a couple hundred femto-seconds using electro-optic sampling technique. In this scheme, a transform-limited laser

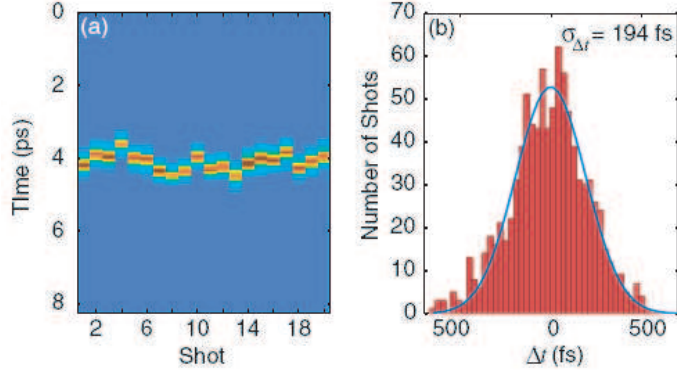


Figure 6.6: (a) The bright band in each column is the electro-optic signal, and its location indicates the time of arrival of the electron bunch with respect to the laser probe pulse and the width corresponds to the electron bunch duration. (b) Normalized arrival time histogram of 1000 consecutive single shots.

oscillator pulse is sent from the laser lab to the Final Focus Test Beam (FFTB) site via 150 meters long single mode optical fiber. To achieve the delivery of a transform limited pulse through the fiber, a novel pulse compression scheme was employed. Inside FFTB, the optical beam out of the fiber is directed through electro-optic crystal along with the electron bunch inside the vacuum pipe. By systematically recording when the rotation in polarizations of laser beam occurs and then pairing the laser pulse with its relative arrival time to the electron bunch, it is possible to perform a femtosecond time-resolution experiment at SPPS. In fact, my colleague and also a friend, David M. Fritz, has been working on a laser pumped and X-ray probed experiment at SPPS based on the novel timing scheme described above. In his work, he intends to learn about the decay mechanism of coherent optical phonon modes in Bismuth. Prior to this attempt, such an experiment has not been possible on any synchrotron facilities because a temporal resolution of at least 300 fs is required to see the coherent oscillations of the lattice in Bismuth. His preliminary data set indicates

that the proposed electro-optic-sampling scheme provides adequate time-resolution to study femtosecond dynamics at linear accelerator based X-ray sources.

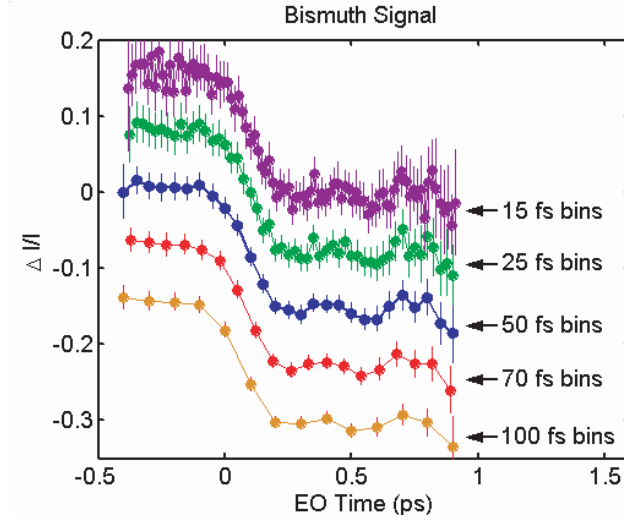


Figure 6.7: Time-Resolved X-ray pump-probe data taken at SPPS by David M. Fritz during summer of 2005. Using a novel timing scheme developed by Adrian et al [12], lattice dynamics occurring at sub-picosecond time scale can now be observed at an accelerator-based facility. Latest technologies in ultrafast X-ray field will soon give us sufficient tool to test our fundamental understanding of condensed matter physics.

Finally, X-ray free electron laser developments are under way in several locations around the world. This particular X-ray source addresses issues of both the time-resolution and the flux of the X-rays. The Linac Coherent Light Source (LCLS) project, which is expected to be completed by 2009, is a prime example of such efforts. The fundamental design is similar to that of SPPS except it utilizes coherent oscillations of individual electrons in a bunch to produce 6 orders of magnitude more X-ray photons per pulse than current 3rd generation synchrotrons. Upon the completion of LCLS, several experiments can be performed that will take advantage of unprecedented temporal and spatial resolution of the X-rays.

6.2 New Sciences

Given the capabilities of upcoming ultrafast and ultra-bright X-ray sources, there is not a slightest trace of doubt in my mind that a lot of questions that we cannot answer at this time will be answered. In advanced facilities such as LCLS, the atomic structures of nano-scale objects and small clustered molecules can be imaged. Even biological materials without periodic structures could possibly be studied. Furthermore, it could be an opportunity to develop a new field of condensed matter physics. Most of the knowledge and the modeling scheme of lattice dynamics in solids are based on continuum wave dynamics. However if we are given an ability to observe non-equilibrium acoustic phonons at an arbitrary wave vector in a crystalline medium, we will need to come up with a new physics to explain what we will see. For example most widely accepted modeling scheme at heterostructure boundaries is acoustic mismatch model. As it is demonstrated in my work, acoustic mismatch model readily serves its purpose when we study low wave-vector phonons. However it is also demonstrated that ultrafast optical pulses with sufficient energy can excite phonons at least up to 1THz, where acoustic mismatch model cannot be used. As we become sensitive to phonon modes with mean free-path comparable to lattice parameters, interpretation based on the acoustic mismatch model will certainly break down. Use of the diffuse-mismatch model, of which validity is still not well established, will be more appropriate. We will also be able to see frequency down conversion process of THz acoustic phonons to lower acoustic modes. Although we can already detect phonon modes up to THz, we do not have sufficient X-ray photon

flux or time-resolution to obtain meaningful data to explain high frequency phonon dynamics. However if facilities such as LCLS can deliver its promised specs, we will be able to study such dynamics, possibly even at a single shot experiment. Until then, I will still be doing my part to study these phenomena but our work will certainly become more feasible as more advanced technologies become available.

APPENDICES

APPENDIX A

Structural Factor Calculation

```
% Numerical Calculation of Structure Factor

% this function requires aff_not.m and aff.m

% Imaginary part of form factor found from http://www-cxro.lbl.gov/optical_constants/

% In this appendix, structure factor for a ZincBlend specifically GaAs is calculated.

global Arsenic1 Gallium1 Arsenic0 Gallium0

a = 5.6419;

for h = 0:4

    for k = 0:4

        for l = 0:4

            if( sqrt( $h^2 + k^2 + l^2$ ) <= 4 )

                K = 2*pi/a * [h; k; l];

                aff_not(0, 0, 0);

                aff(h, k, l);

                Gallium = Gallium1 - Gallium0 + 28.03 + 0.5363*i;

                Arsenic = Arsenic1 - Arsenic0 + 31.4350 + 0.720972*i;

                [h; k; l]
```



```

sum = Gallium*exp(-i*dot(K,[0;0;0]));

sum = sum + Gallium*exp(-i*dot(K,[a/2;a/2;0]));

sum = sum + Gallium*exp(-i*dot(K,[0;a/2;a/2]));

sum = sum + Gallium*exp(-i*dot(K,[a/2;0;a/2]));

sum = sum + Arsenic*exp(-i*dot(K,[a/4;a/4;a/4]));

sum = sum + Arsenic*exp(-i*dot(K,[3*a/4;a/4;3*a/4]));

sum = sum + Arsenic*exp(-i*dot(K,[3*a/4;3*a/4;a/4]));

sum = sum + Arsenic*exp(-i*dot(K,[a/4;3*a/4;3*a/4]));

sum

end

end

end

end

```

```

function [Gallium, Arsenic] = aff(h,k,l)

global Gallium1 Arsenic1

% Lattice constant and Sin Theta over Lambda

a = 5.6419;

stl = sqrt( $h^2 + k^2 + l^2$ )/(2*a);

%Ga

a1 = 15.2354;

b1 = 3.06690;


a2 = 6.7006;

b2 = 0.2412;


a3 = 4.35910;

b3 = 10.7805;


a4 = 2.96230;

b4 = 61.4135;


c = 1.71890;


f = a1*exp(-b1*stl*stl) + a2*(-b2*stl*stl) + a3*exp(-b3*stl*stl) + a4*exp(-b4*stl*stl)

+ c;

```

Gallium1 = f;

%As

a1 = 16.6723;

b1 = 2.63450;

a2 = 6.07010;

b2 = 0.2647;

a3 = 3.4313;

b3 = 12.9479;

a4 = 4.2779;

b4 = 47.7972;

c = 2.531;

f = a1*exp(-b1*stl*stl) + a2*(-b2*stl*stl) + a3*exp(-b3*stl*stl) + a4*exp(-b4*stl*stl)
+ c;

Arsenic1 = f;

```
function [Gallium, Arsenic] = aff(h,k,l)
```

```
global Gallium0 Arsenic0
```

```
% Lattice constant and Sin Theta over Lambda
```

```
a = 5.6419;
```

```
stl = sqrt( $h^2 + k^2 + l^2$ )/(2*a);
```

```
%Ga
```

```
a1 = 15.2354;
```

```
b1 = 3.06690;
```

```
a2 = 6.7006;
```

```
b2 = 0.2412;
```

```
a3 = 4.35910;
```

```
b3 = 10.7805;
```

```
a4 = 2.96230;
```

```
b4 = 61.4135;
```

c = 1.71890;

f = a1*exp(-b1*stl*stl) + a2*(-b2*stl*stl) + a3*exp(-b3*stl*stl) + a4*exp(-b4*stl*stl)

+ c;

Gallium0 = f;

%As

a1 = 16.6723;

b1 = 2.63450;

a2 = 6.07010;

b2 = 0.2647;

a3 = 3.4313;

b3 = 12.9479;

a4 = 4.2779;

b4 = 47.7972;

c = 2.531;

$$f = a1*\exp(-b1*stl*stl) + a2*(-b2*stl*stl) + a3*\exp(-b3*stl*stl) + a4*\exp(-b4*stl*stl) \\ + c;$$

$$\text{Arsenic0} = f;$$

APPENDIX B

Matlab Code for GaAs Dynamical Matrix Calculation

% This Matlab Code forms a Dynamical Matrix of a Zinc-Blend Structure % for given
sets of wave-vector q1, q2, q3 % And then, it outputs associated phonon frequency
(i.e. dispersion relation)

function e = DM_ZincBlend(q1,q2,q3)

% Interatomic Force constants for GaAs

% in units of 10^4 dyn cm-1

% Frank Herman, J. Phys. Chem. Solids Vol. 8, pp405-418 (1959)

a = 4.9536;

b = 3.0822;

u = 0.2366;

l = -0.3194;

v = 0.4638;

d = 0;

u1 = -0.2629;

l1 = -0.0643;

v1 = 0.2494;

d1 = -0.2788;

u11 = 0.1088;

l11 = -0.1197;

u111 = 0.1321;

l111 = 0.1321;

v111 = 0.0605;

d111 = 0.0605;

u1111 = -0.7493;

l1111 = 1.5176;

v1111 = -0.1474;

d_p1111 = 0.0843;

d_n1111 = (0.5)*(d_p1111 - l1111);

% Pi is pie

PI = pi;

% Analytical solution to obtaining Dyamical Matrix elements

$$G11 = 4*a + 4*l*(1 - \cos(\pi*q2)*\cos(\pi*q3));$$

$$G11 = G11 + 4*u*(2 - \cos(\pi*q3)*\cos(\pi*q1) - \cos(\pi*q1)*\cos(\pi*q2));$$

$$G11 = G11 + 8*u1 + 4*l1 + 2*l11*(1 - \cos(2*\pi*q1)) + 2*u11*(2 - \cos(2*\pi*q2) - \cos(2*\pi*q3));$$

$$G11 = G11 + 8*u111 + 4*l111 + 8*l1111*(1 - \cos(2*\pi*q1)*\cos(\pi*q2)*\cos(\pi*q3));$$

$$G11 = G11 + 8*u1111*(2 - \cos(2*\pi*q2)*\cos(\pi*q3)*\cos(\pi*q1) - \cos(2*\pi*q3)*\cos(\pi*q1)*\cos(\pi*q2));$$

$$G12 = 4*v*\sin(\pi*q1)*\sin(\pi*q2) - \sqrt{-1}*4*d*\sin(\pi*q3)*(\cos(\pi*q1) - \cos(\pi*q2));$$

$$G12 = G12 + 8*v1111*\sin(\pi*q1)*\sin(\pi*q2)*\cos(2*\pi*q3);$$

$$G12 = G12 + 8*d_p1111*\cos(\pi*q3)*(\sin(\pi*q1)*\sin(2*\pi*q2) - \sin(\pi*q2)*\sin(2*\pi*q1));$$

$$G12 = G12 - \sqrt{-1}*8*d_n1111*\sin(\pi*q3)*(\cos(\pi*q1)*\cos(2*\pi*q2) - \cos(\pi*q2)*\cos(2*\pi*q1));$$

$$G14 = -a*(1 + \exp(-\pi*\sqrt{-1}*(q1+q2)) + \exp(-\pi*\sqrt{-1}*(q2+q3)) + \exp(-\pi*\sqrt{-1}*(q3+q1)));$$

$$G14 = G14 - l1*((1 + \exp(-\pi*\sqrt{-1}*(q2+q3))) * \exp(-2*\pi*\sqrt{-1}*q1) + (\exp(-\pi*\sqrt{-1}*q2) + \exp(-\pi*\sqrt{-1}*q3)) * \exp(\pi*\sqrt{-1}*q1));$$

$$\begin{aligned}
G14 &= G14 - u1*((1+\exp(-PI*\sqrt{-1}*(q3+q1)))\exp(-2*PI*\sqrt{-1}*q2) + (\exp(-PI*\sqrt{-1}*q3) + \exp(-PI*\sqrt{-1}*q1))\exp(PI*\sqrt{-1}*q2)); \\
G14 &= G14 - u1*((1+\exp(-PI*\sqrt{-1}*(q1+q2)))\exp(-2*PI*\sqrt{-1}*q3) + (\exp(-PI*\sqrt{-1}*q1) + \exp(-PI*\sqrt{-1}*q2))\exp(PI*\sqrt{-1}*q3)); \\
G14 &= G14 - l111*((\exp(-PI*\sqrt{-1}*(2*q2-q3)) + \exp(-PI*\sqrt{-1}*(2*q3-q2)))\exp(-PI*\sqrt{-1}*q1) + \exp(PI*\sqrt{-1}*(q2+q3)) + \exp(-2*PI*\sqrt{-1}*(q2+q3))); \\
G14 &= G14 - u111*((\exp(-PI*\sqrt{-1}*(2*q3-q1)) + \exp(-PI*\sqrt{-1}*(2*q1-q3)))\exp(-PI*\sqrt{-1}*q2) + \exp(PI*\sqrt{-1}*(q3+q1)) + \exp(-2*PI*\sqrt{-1}*(q3+q1))); \\
G14 &= G14 - u111*((\exp(-PI*\sqrt{-1}*(2*q1-q2)) + \exp(-PI*\sqrt{-1}*(2*q2-q1)))\exp(-PI*\sqrt{-1}*q3) + \exp(PI*\sqrt{-1}*(q1+q2)) + \exp(-2*PI*\sqrt{-1}*(q1+q2))); \\
\\
G15 &= -b*(1 + \exp(-PI*\sqrt{-1}*(q1+q2)) - \exp(-PI*\sqrt{-1}*(q2+q3)) - \exp(-PI*\sqrt{-1}*(q3+q1))); \\
G15 &= G15 - d1*((-1 + \exp(-PI*\sqrt{-1}*(q2+q3)))\exp(-2*PI*\sqrt{-1}*q1) + (-\exp(-PI*\sqrt{-1}*q2) + \exp(-PI*\sqrt{-1}*q3))\exp(PI*\sqrt{-1}*q1)); \\
G15 &= G15 - d1*((-1 + \exp(-PI*\sqrt{-1}*(q3+q1)))\exp(-2*PI*\sqrt{-1}*q2) + (-\exp(-PI*\sqrt{-1}*q3) + \exp(-PI*\sqrt{-1}*q1))\exp(PI*\sqrt{-1}*q2)); \\
G15 &= G15 - v1*((1 + \exp(-PI*\sqrt{-1}*(q1+q2)))\exp(-2*PI*\sqrt{-1}*q3) + (-\exp(-PI*\sqrt{-1}*q1) + \exp(-PI*\sqrt{-1}*q2))\exp(PI*\sqrt{-1}*q3)); \\
G15 &= G15 - d111*(\exp(PI*\sqrt{-1}*(q2+q3)) - \exp(-2*PI*\sqrt{-1}*(q2+q3)) + (\exp(-PI*\sqrt{-1}*(2*q2-q3)) - \exp(-PI*\sqrt{-1}*(q3-q2)))\exp(-PI*\sqrt{-1}*q1));
\end{aligned}$$

$$G15 = G15 - d111*(\exp(\text{PI}*\sqrt{-1}*(q3+q1)) - \exp(-2*\text{PI}*\sqrt{-1}*(q3+q1)) + (-\exp(-\text{PI}*\sqrt{-1}*(2*q3-q1)) - \exp(-\text{PI}*\sqrt{-1}*(q1-q3)))*\exp(-\text{PI}*\sqrt{-1}*q2));$$

$$G15 = G15 - v111*(\exp(\text{PI}*\sqrt{-1}*(q1+q2)) - \exp(-2*\text{PI}*\sqrt{-1}*(q1+q2)) + (-\exp(-\text{PI}*\sqrt{-1}*(2*q1-q2)) - \exp(-\text{PI}*\sqrt{-1}*(q2-q1)))*\exp(-\text{PI}*\sqrt{-1}*q3));$$

$$G13 = \text{conj}(G12);$$

$$G16 = G15;$$

$$G21 = \text{conj}(G12);$$

$$G22 = G11;$$

$$G23 = G12;$$

$$G24 = G15;$$

$$G25 = G14;$$

$$G26 = G15;$$

$$G31 = G12;$$

$$G32 = \text{conj}(G12);$$

$$G33 = G11;$$

$$G34 = G15;$$

$$G35 = G26;$$

$$G36 = G14;$$

$$G41 = \text{conj}(G14);$$

$$G42 = \text{conj}(G24);$$

$$G43 = \text{conj}(G34);$$

$$G44 = G11;$$

$$G45 = \text{conj}(G12);$$

$$G46 = G31;$$

$$G51 = \text{conj}(G15);$$

$$G52 = \text{conj}(G25);$$

$$G53 = \text{conj}(G35);$$

$$G54 = G12;$$

$$G55 = G11;$$

$$G56 = \text{conj}(G23);$$

$$G61 = \text{conj}(G16);$$

$$G62 = \text{conj}(G26);$$

$$G63 = \text{conj}(G36);$$

$$G64 = \text{conj}(G46);$$

$$G65 = G23;$$

$$G66 = G11;$$

$$D(1,1) = G11;$$

$$D(1,2) = G12;$$

$$D(1,3) = G13;$$

$$D(1,4) = G14;$$

$$D(1,5) = G15;$$

$$D(1,6) = G16;$$

$$D(2,1) = G21;$$

$$D(2,2) = G22;$$

$$D(2,3) = G23;$$

$$D(2,4) = G24;$$

$$D(2,5) = G25;$$

$$D(2,6) = G26;$$

$$D(3,1) = G31;$$

$$D(3,2) = G32;$$

$$D(3,3) = G33;$$

$$D(3,4) = G34;$$

$$D(3,5) = G35;$$

$$D(3,6) = G36;$$

$$D(4,1) = G41;$$

$$D(4,2) = G42;$$

$$D(4,3) = G43;$$

$$D(4,4) = G44;$$

$$D(4,5) = G45;$$

$$D(4,6) = G46;$$

$$D(5,1) = G51;$$

$$D(5,2) = G52;$$

$$D(5,3) = G53;$$

$$D(5,4) = G54;$$

$$D(5,5) = G55;$$

$$D(5,6) = G56;$$

$$D(6,1) = G61;$$

$$D(6,2) = G62;$$

$$D(6,3) = G63;$$

$$D(6,4) = G64;$$

$$D(6,5) = G65;$$

$$D(6,6) = G66;$$

% Calculates for eigenvalue, frequency square

e = eig(D);

e = abs(sqrt(e))

% returns frequency e

APPENDIX C

Physical Parameters of GaAs

material property	tabulated values
Electronic Source	www.ioffe.rssi.ru/SVA/NSM/Semicond
Crystal structure	Zinc Blende
Density	5.32 g/cm^3
Lattice constant	5.65325 \AA
Energy Gap	1.424 eV
Auger coefficient	$\sim 10^{-30} \text{ cm}^6/\text{s}$
Electron Diffusion Coefficient	$200 \text{ cm}^2/\text{s}$
Hole Diffusion Coefficient	$10^2/\text{s}$
Specific Heat	0.33 J/g K
Thermal Conductivity	0.55 W/cm K
Thermal Diffusivity	$0.31 \text{ cm}^2/\text{s}$

BIBLIOGRAPHY

BIBLIOGRAPHY

- [1] G. C. Cho, T. Dekorsy, H. J. Bakker, R. Hovel, and H. Kruz. *Phys. Rev. Lett.*, 77(4062), 1996.
- [2] Klaus Sokolowski-Tinten, Christian Blome, Juris Blums, Andrea Cavalleri, Clemens Dietrich, Alexander Tarasevitch, Ingo Uschmann, Eckhard Förster, Martin Kammler, Michael Horn von Hoegen, and Dietrich von der Linde. *Nature*, 422(287), 2003.
- [3] A. M. Lindenberg, I. Kang, S. L. Johnson, T. Missalla, P. A. Heimann, Z. Chang, J. Larsson, P. H. Bucksbaum, H. C. Kapteyn, H. A. Padmore, R. W. Lee, J. S. Wark, and R. W. Falcone. *Phys. Rev. Lett.*, 84:111–114, 2000.
- [4] D. A. Reis, M. F. DeCamp, P. H. Bucksbaum, R. Clarke, E. Dufresne, M. Hertlein, R. Merlin, R. Falcone, H. Kapteyn, M. M. Murnane, J. Larsson, Th. Missalla, , and J. S. Wark. *Phys. Rev. Lett.*, 86:3072–3075, 2001.
- [5] <http://www.adc9001.com/documents/company/publications/primers/ionchamberconversions.pdf>.
- [6] C. Thomsen, H. T. Grahn, H. J. Maris, and J. Tauc. *Phys. Rev. B*, 34:4129–4138, 1986.
- [7] Martin Kull and Jean-Louis Cutaz. *J. Opt. Soc. Am. B*, 7(1463), 1990.
- [8] Alberto Debernardi. *Phys. Rev. B*, 57, 1998.
- [9] R. Baltramiejunas, A. Zukauskas, V. Latinis, , and S. Jursenas. *Pos'ma Zh. Eksp. Theo. Fiz.*, 46(67), 1987.
- [10] Merrill G. Raikes. *RadioGraphics*, 23:1149–1154, 2003.
- [11] <http://www.anl.gov/MediaCenter/logos21-1/>: X-rays penetrate secrets of diesel engine.
- [12] A. L. Cavalieri, D. M. Fritz, S. H. Lee, P. H. Bucksbaum, D. A. Reis, J. Rudati, D. M. Mills, P. H. Fuoss, G. B. Stephenson, C. C. Kao, D. P. Siddons, D. P. Lowney, A. G. MacPhee, D. Weinstein, R. W. Falcone, R. Pahl, J. Als-Nielsen, C. Blome, S. Düsterer, R. Ischebeck, H. Schlarb, H. Schulte-Schrepping, Th.

- Tschentscher, J. Schneider, O. Hignette, F. Sette, K. Sokolowski-Tinten, H. N. Chapman, R. W. Lee, T. N. Hansen, O. Synnergren, J. Larsson, S. Techert, J. Sheppard, J. S. Wark, 14 M. Bergh, C. Caleman, G. Huldt, D. van der Spoel, N. Timneanu, J. Hajdu, R. A. Akre, E. Bong, P. Emma, P. Krejcik, J. Arthur, S. Brennan, K. J. Gaffney, A. M. Lindenberg, K. Luening, and J. B. Hastings. *Physical Review Letters*, 94(114801), 2005.
- [13] H. Ehrenreich. *Phys. Rev.*, 120(1951), 1960.
 - [14] H. Ehrenreich et al. *J. Appl. Phys. Suppl*, 32(2155), 1961.
 - [15] E. M. Conwell. *Solid State Physics*. Academic, New York.
 - [16] D. L. Rode. *Phys. Rev. B*, 2(1012), 1970.
 - [17] D. L. Rode and S. Knight. *Phys. Rev. B*, 3(2534), 1971.
 - [18] A. Ecli, M. O. Scully and A. L. Smirl, , and J. C. Matter. *Phys. Rev. B*, 16(191), 1977.
 - [19] A. Ecli, A. L. Smirl, C. Y. Leung, and M. O. Scully. *Solid-State Electronics*, 21(51), 1978.
 - [20] C.V. Shank and D.H. Auston. *Phys. Rev. Lett.*, 34(479), 1975.
 - [21] R. Leadon and J. A. Naber. *J. Appl. Phys*, 40(2633), 1969.
 - [22] E. J. Yoffa. *Phys. Rev. B*, 21(2415), 1980.
 - [23] E. J. Yoffa. *Phys. Rev. B*, 23(1909), 1981.
 - [24] D. von der Linde and R. Lambrich. *Phys. Rev. Lett.*, 42(1090), 1979.
 - [25] A. Mooradian and H. Y. Fan. *Phys. Rev.*, 148(873), 1966.
 - [26] A. Mooradian. *Laser Handbook*. North-Holland, Amsterdam.
 - [27] J. Kuhl W. E. Bron and B. K. Rhee. *Phys. Rev.*, B34(6961), 1986.
 - [28] D. von der Linde. *Tpics Appl. Phys*, 60, 1988.
 - [29] F. Vallee. *Phys. Rev. B*, 49(2460), 1994.
 - [30] F. Ganikhanov and F. Vallee. *Phys. Rev. B*, 55(15614), 1997.
 - [31] I.B. Khaibulin, B.I. Shtyrkov, M. M. Zaripov, R. M. Bayazitov, and M. F. Galjautdinov. *Galjautdinov, Radia. Eff.*, 36(225), 1978.
 - [32] In N. J. Leamy S. D. Ferris and J. M. Poate, editors, *Laser-Solid Interactions and Laser Processing 1978*. American Physical Society, New York, 1978.

- [33] *Maximizing 300mm Yield Through Automated Macrodefect Inspection*. Semiconductor Manufacturing, May 2005.
- [34] Production monitoring of copper chemical mechanical planarization processes with picosecond ultrasonic metrology. Semicon Korea 2004 Technology Seminar, 2004.
- [35] H. Y. Hao and H. J. Maris. *Phys. Rev. B*, 63(224301), 2001.
- [36] H. Y. Hao and H. J. Maris. *Phys. Rev. B*, 64(64302), 2001.
- [37] S. N. Ehrlich, L. D. Chapman, and N. M. Lazarz. *Solid State Comm.*, 81:451–456, 1992.
- [38] L. D. Chapman, S. M. Heieh, and R. Colella. *Phys. Rev. B*, 30(2), 1984.
- [39] Rischel C et al Christian Rischel, Antoine Rousse, Ingo Uschmann, Pierre Antoine Albouy, Jean Paul Geindres, Patrick Audeberts, Jean Claude Gauthiers, Eckhart Froster, Jean Louis Martin, and Andre Antonetti. *Nature*, 390(490), 1997.
- [40] A. Cavalleri, Cs. Toth, C. W. Siders, and J. A. Squier. *Phys. Rev. Lett.*, 2001.
- [41] K. Sokolowski-Tinten, C. Blome, C. Dietrich, A. Tarasevitch, M. Horn von Hoegen, D. von der Linde, A. Cavalleri, J. Squier, and M. Kammler. *Phys. Rev. Lett.*, 26(225701), 2001.
- [42] F. R. Elder, A. M. Gurewitsch, R. V. Langmuir, and H. C. Pollock. *Phys. Rev.*, 71:829–829, 1947.
- [43] F. R. Elder, R. V. Langmuir, , and H. C. Pollock. *Phys. Rev.*, 74:52–56, 1948.
- [44] K. J. Kim. *Methods Phys. Res A*, 246(71), 1986.
- [45] F. Schotte, S. Techert, P. Anfinrud, V. Srajer, K. Moffat, and M. Wulff. Time resolved experiments in the picosecond to microsecond range using pulsed synchrotron radiation.
- [46] J. Als-Nielsen and D. McMorrow. *Elements of Modern X-Ray Physics*. Wiley, New York.
- [47] O. E. Martinez. *IEEE J. Quantum Electron*, 23(59), 1987.
- [48] S. Backus, J. Peatross, C. P. Huang, M. M. Murnane, and H. C. Kapteyn. *Opt. Lett.*, 20(2000), 1995.
- [49] J. V. Rudd, G. Korn, S. Kane, Jeff Squier, Gerard A. Mourou, and Philippe Bado. *Opt. Lett.*, 18(2044), 1993.

- [50] Jeff Squier, Chris P. J. Barty, Francois Salin, Catherine Le Blanc, and Steve Kane. *Appl. Opt.*, 37(1638), 1998.
- [51] B. E. A. Saleh and M. C. Teich. *Photonics*. Wiley, New York, 1991.
- [52] William Jones and Norman H. March. *Theoretical Solid State Physics Volume1: Perfect Lattice in Equilibrium*. Dover Publications, Inc., New York, 1985.
- [53] C. Kittel. Introduction to solid state physics. 7th edition. 1996.
- [54] Neil W. Ashcroft and N. David Mermin. *Solid State Physics*. Thomson Learning, Inc., 1976.
- [55] J.R. Hook and H.E. Hall. Solid state physics. 1991.
- [56] M.F. DeCamp, D. A. Reis, A. Cavalieri, P. H. Bucksbaum, R. Clarke, R. Merlin, E. M. Dufresne, D. A. Arms, A. M. Lindenberg, A. G. MacPhee, Z. Chang, B. Lings, J. S. Wark, and S. Fahy. *Phys. Rev. Lett.*, 91, 2003.
- [57] Xiaoping Cao. *J. Phys. Chem. Solids*, 47:981–986, 1986.
- [58] Lax M. *Symmetry Principles in Solid-State and Molecular Physics*. Wiley Interscience, New York, 1974.
- [59] B.E. Warren. *X-Ray Diffraction*. Dover, New York, 1969.
- [60] J.M. Cowley and Moodie. *Acta Cryst.*, 10, 1959.
- [61] N. Kato. *Acta. Cryst.*, 13:349–356.
- [62] D.G. Cahill, W.K. Ford, K.E. Goodson, G.D. Mahan, A. Majumdar, H.J. Maris, R. Merlin, , and S.R. Phillpot. *J. Appl. Phys.*, 2003.
- [63] E. T. Swartz, R. O. Pohl, and Rev. Mod. *J. Phys.*, 61(3), 1989.
- [64] J.P. Wolfe. *Imaging Phonons: Acoustic Wave Propagation in Solids*. 1998.
- [65] V. Narayanamurti, H.L. Stormer. M.A. Chin, A.C. Gossard, and W. Wiemann. *Phys. Rev. Lett.*, 1979.
- [66] B.C. Daly, H.J. Maris, W.K. Ford, G.A. Antonelli, L. Wong, and E. Andideh. *J. Appl. Phys.*, 2002.
- [67] R.M. Costescu, M.A. Wall, , and D.G. Cahill. *Phys. Rev. B*, 2003.
- [68] R. J. Stoner and H.J. Maris. *Phys. Rev. B*, 1993.
- [69] G. Tas and H.J. Maris. *Phys. Rev. B*, 1993.
- [70] I.V. Tomov P. Chen and P.M. Rentzepis. *J. Chem. Phys.*, 104, 1996.

- [71] Christoph Rose-Petruck, Ralph Jimenez, Ting Guo, Andrea Cavalleri, Craig W. Siders, Ferenc Rksi, Jeff A. Squier, Barry C. Walker, Kent R. Wilson, and Christopher P. J. Barty. *Nature*, 398, 1999.
- [72] A. Cavalleri, C. W. Siders, F. L. H. Brown, D. M. Leitner, C. Tóth, J. A. Squier, C. P. J. Barty, and K. R. Wilson. *Phys. Rev. Lett.*, 85(586), 2000.
- [73] M. Bargheer, Y. Gritsai N. Zhavoronkov, J.C. Woo, D.S. Kim, M. Woerner, , and T. Elsaesser. *Science*, 306(1771), 2004.
- [74] P. Sonhauss, K. Larsson, M. Harbst, G.A. Naylor, A. Plech, K. Scheidt, O. Synnergren, M. Wulff, and J.S. Wark. *Phys. Rev. Lett.*, 94(125509), 2005.
- [75] M.F. DeCamp, DA Reis, DM Fritz, PH Bucksbaum, EM Dufresne, and R. Clarke. *J. Synch. Rad.*, 2005.
- [76] B.W. Batterman and Cole. *Rev. Mod. Phys.*, 36:681–717, 1964.
- [77] D. Taupin. *Bill. Soc. Fr. Mineral. Cryt.*, 87:469–511, 1964.
- [78] Walter A. Harrison. *Electronic Structure and the Properties of Solids*. Dover Publications, Inc., New York, 1989.
- [79] Thomas F. Boggess, Arthur L. Smirl, Steve C. Moss, Ian W. Boyd, and Stryland Eric W. Van. *IEEE Journal of Quantum Electronics QE*, 21:488–494, 1985.
- [80] J.M. Ralston and R.K. Chang. *Appl. Phys. Lett.*, pages 164–166, 1969.
- [81] V.V. Arsenájev, V.S. Dneprovskii, D.N. Klyshko, and A.N. Penin. *Sov. Phys. JETP*, 29:413–415, 1969.
- [82] H.A. Lorent. *theory of Electrons*. Teubner, Leipzig, 1906.
- [83] F. Seitz. McGraw-Hill, New York, 1940.
- [84] Ralph M. Grant. *Applied Optics*, 5:333–341, 1966.
- [85] K.G. Svantesson. *J. Phys. D: Appl. Phys.*, 12:425–435, 1979.
- [86] R.G. Ulbrich. Nonequilibrium phonon dynamics. 124:101–127, 1985.
- [87] Ulbrich R.G., Narayanamuti V., and Chin M.A. *Phys. Rev. Lett.*, 45, 1980.
- [88] M.J. Colles and J.A. Giordmaine. *Phys. Rev. Lett.*, 27:670–674, 1971.
- [89] S.E. Hebboul and J.P. Wolfe. *Phys. Rev. Lett.*, 34(3948), 1986.
- [90] D.B. McWhan, P. Hu, M.A. Chin, and Narayanamurti. *Phys. Rev. B*, 26(R4774), 1982.

ABSTRACT

Time-resolved X-ray Measurements of Energy Relaxation in Ultrafast
Laser-Excited Semiconductors

by

Soo Heyong Lee

Chair: Reis, David A.

In semiconductors, the properties and dynamics of photoexcited carriers and subsequent energy relaxation through lattice vibrations are quite complex and occur on a variety of time scales. Typically the transient dynamics involving transitions of electrons from lower energy states to higher ones upon photoexcitation take place almost instantaneously. The electrons eventually recombine with holes while losing most of their kinetic energy to the lattice through various routes at different time scales. The lattice relaxation processes, especially at high photoexcitation levels, have been subjected to numerous experimental and theoretical investigations during past decades.

Time-resolved X-ray diffraction (TRXD) method provides a novel tool for studying these dynamics because X-rays have short wavelength, long material penetration

depth and relatively strong interaction with core electrons. In my work, femtosecond laser pulses excite electrons in opaque materials, and subsequent carrier relaxation process and coherent/incoherent lattice dynamics are investigated using TRXD. My thesis covers quantitative detail of the generation and propagation of ultrafast laser induces acoustic strain waves in bulk semiconductor materials as well as at the heterostructure interface. In particular propagation of strain waves, which are comprised of broadband low wave vector phonons, is studied in an AlGaAs/GaAs multilayer structure. The spatial and temporal profiles of the acoustic waves at varying photoexcitation density are characterized. We are able to distinguish thermal from carrier-induced strain and measure the free-carrier absorption cross-section. The approximation that impulsively generated acoustic waves are uniaxial is found to break down. The research also demonstrates a novel approach to explore laser induced acoustic phonon dynamics at high wavevector, near the Brillouin zone-boundary, the details of which are inaccessible to optical pump-probe methods. Throughout this thesis, the validity and limits of our theoretical model of high frequency acoustic phonon generation are examined. Toward the end, theoretical and experimental challenges are addressed and possible solutions are presented.